TECHNISCHE
UNIVERSITÄT
WIEN

DIPLOMARBEIT

Angular Distributions and Time Ordering in Double Ionization of Helium: Approaching the Long-wavelength Regime

zur Erlangung des akademischen Grades

Diplom-Ingenieur

im Rahmen des Studiums

Technische Physik

eingereicht von

Manuel Ederer
Matrikelnummer 01327066

ausgeführt am Institut für Theoretische Physik
der Fakultät für Physik der Technischen Universität Wien

Betreuung
Betreuer: O.Univ.-Prof. Dipl.-Phys. Dr.rer.nat. Joachim Burgdörfer
Mitwirkung: Projektass. Dipl.-Ing. Stefan Donsa

Wien, 7.1.2020 _____ _____

(Unterschrift Verfasser) (Unterschrift Betreuer)

Contents

List of Acronyms

APT Attosecond pulse train
ATI Above threshold ionization
CC Continuum-continuum (phase)
CD Circular dichroism
CTMC Classical trajectory Monte-Carlo (simulation)
DI Double ionization
DI-PES Double ionization photo electron spectrum
EWS Eisenbud-Wigner-Smith (time delay)
FEDVR Finite-element discrete-variable-representation
FWHM Full width at half maximum
HHG High-harmonic generation
IR Infra red
JAD Joint-angular distribution
LCP Left circular polarization
MB Main band
NS Non-sequential
o.c. Optical cycles
OPDI One-photon double ionization
PES Photo-electron spectrum
RABBITT Reconstruction of attosecond bursts by interference of two-photon transitions
RCP Right circular polarization
SAE Single active electron
SB Side band
SI Single ionization
SI-PES Single ionization photo electron spectrum
TDSE Time-dependent Schrödinger equation
TPDI/2-PDI Two-photon double ionization
XUV Extreme ultraviolet

1. Introduction

With the progress in laser technologies over recent years it has become possible to create coherent and intense extreme ultraviolet (XUV) pulses via high-harmonic generation [1–5] with durations of only a few femtoseconds (1 fs = 10^{-15} s) or even reaching the attosecond (1 as = 10^{-18} s) regime. This development has started the field of attosecond science [6–8] which has enabled detailed studies of electron dynamics with a time resolution down to single attoseconds. In order to ultimately be able to control electrons and their motion with all-optical devices, it is a necessity to fully understand the fundamentals of light-matter and electron-electron interaction on this time scale. Double ionization of helium provides the ideal testbed to obtain insights into the electron dynamics in the full three-body Coulomb break-up process, as the process is simple enough such that *ab-initio* computations are numerically feasible.
While the two extremal cases of few-photon [9–12] and strong-field double ionization [13–15] have been studied extensively, the regime in between where 4 to 20 photons are needed to overcome the double ionization threshold of helium has not gained a lot of attention. The reason for this is the numerical complexity and experimental limitations to generate intense light pulses for $\lambda < 400$ nm. Within this thesis we aim at bridging this gap starting from one-photon double ionization, increasing successively the wavelength of the ionizing light field until we approach the experimentally strong-field regime [16]. To do so we employ state of the art *ab-initio* simulations. To characterize the influence of electron-correlation onto the double ionization process, we study similarities and differences in the angular emission pattern over a broad range of wavelengths.
One-photon double ionization has attracted attention from both theoretical and experimental physicists since decades [9, 10, 17, 18]. Electron interaction is essential for this process to occur, as the energy of the single photon ($\omega > 79$ eV) has to be shared between the two electrons. Depending on the degree of correlation different ionization mechanics can be observed. We try to distinguish different processes leading to double ionization from the final joint-angular distribution of the electrons. Further, we investigate the effect of the laser polarization on the angular distribution and observe pronounced circular dichroism [19–21].
Decreasing the carrier frequency of the laser pulse below 79 eV, the number of photons necessary to overcome the double ionization threshold increases. For up to five-photon double ionization ($\lambda = 68.9$ nm) we investigate the influence of the polarization of the ionizing field onto the double ionization process and still find a pronounced circular dichroism. Further decreasing the frequency of the ionizing field allows us to study the transition from the perturbative multi-photon to the tunneling regime. In this regime the primary process leading to double ionization is that one electron is liberated via tunnel ionization, driven back to the core by the laser field where it recollides with the second electron leading to both electrons being ionized. This mechanism has been discovered by observing a "knee"-structure in the double ionization probability as a function of laser peak intensity [13, 22, 23]. Within this thesis we

try to reproduce this structure for lower infrared wavelengths where numerical simulations are still feasible. Unfortunately, however, we are only able to achieve converged results for $\lambda = 100$ nm, but not for $\lambda = 396$ nm where experimental results for strong-field double ionization have been achieved recently [16].
In the second part of this thesis, we focus on time-resolving one- and two-photon double ionization. We employ the RABBITT pump-probe scheme [24, 25] consisting of an attosecond pulse train as pump and a weak infrared field as probe which has been used extensively to time-resolve (or characterize) single ionization [26]. We extend this concept to double ionization [27] and take first steps to disentangle the different contributions to the time delay we retrieved and how they can be interpreted.

2. Theoretical background and computational methods

Double ionization (DI) of atomic helium is among the simplest processes where electronic correlations can be studied and accurate theoretical calculations are still possible. Thus a full understanding of the underlying processes is achievable for a wide range of parameters. Within this chapter we will briefly describe the underlying theoretical concepts and describe the computational methods employed in this thesis. Atomic units ($e = \hbar = m_e = 1$) are used throughout this thesis unless specified differently.

2.1. Hamiltonian

The time dependent electronic dynamics of atoms subject to intense light fields is determined by the time-dependent Schrödinger equation (TDSE)

$$i\partial_t|\Psi(t)\rangle = H|\Psi(t)\rangle. \tag{2.1}$$

The Hamiltonian H can be separated into a time-independent part H_0 and a time-dependent part $V_I(t)$. For atomic helium H_0 is in in the limit of infinite nucleus mass given by

$$H_0 = \frac{\mathbf{p}_1^2}{2} + \frac{\mathbf{p}_2^2}{2} - \frac{2}{r_1} - \frac{2}{r_2} + \frac{1}{|\mathbf{r}_1 - \mathbf{r}_2|} \tag{2.2}$$

with $\mathbf{r}_i$ and $\mathbf{p}_i$ being the relative coordinates and momenta of the electrons. The time-dependent interaction of the electrons with the electromagnetic field is in minimal coupling given by

$$V_I(t) = \mathbf{A}(\mathbf{r}, t)(\mathbf{p}_1 + \mathbf{p}_2) + \frac{\mathbf{A}(\mathbf{r}, t)^2}{2}. \tag{2.3}$$

As typical laser wavelengths are much larger than the distances over which photoionization takes place we employ the dipole approximation for the electromagnetic field. Thus, we neglect the spatial dependence of the vector potential $\mathbf{A}(\mathbf{r}, t) \approx \mathbf{A}(t)$. Using Coulomb gauge, $V_I(t)$ [Eq. (2.3)] is given by

$$V_v(t) = \mathbf{A}(t)(\mathbf{p}_1 + \mathbf{p}_2) + \frac{\mathbf{A}(t)^2}{2}. \tag{2.4}$$

The quadratic term $\mathbf{A}(t)^2/2$ can be absorbed into the wave function as a global phase factor and will be omitted from here on. Applying the unitary Göppert-Mayer gauge transformation to the wave function

$$|\Psi_L\rangle = e^{i\mathbf{A}(t)\mathbf{r}}|\Psi_v\rangle \tag{2.5}$$

results in the length gauge for the laser-electron interaction

$$V_{\mathrm{L}}(t) = \mathbf{E}(t)(\mathbf{r}_1 + \mathbf{r}_2). \tag{2.6}$$

Both formulations of the light-matter interaction [Eq. (2.4) and Eq. (2.6)] are in principle equivalent and results for physical observables should be independent of the chosen gauge. The numerical implementations, however, differ and thus comparing the results for the two gauges can be used as a test for numerical convergence.
The helium singlet groundstate (parahelium) can be described as a product of spatial and spin functions

$$\langle \mathbf{r}_1 \mathbf{r}_2 | \Psi(t) \rangle = \Psi(\mathbf{r}_1, \mathbf{r}_2, t) \otimes \frac{1}{\sqrt{2}} \left(|\uparrow\downarrow\rangle - |\downarrow\uparrow\rangle \right). \tag{2.7}$$

The ground state is a singlet state and the electron-laser interaction within the dipole approximation is spin-conserving. Therefore, the wavefunction remains in the singlet state for the full propagation time.

2.2. Time-dependent close-coupling method

In our numerical implementation, the full three-dimensional time-dependent Schrödinger equation (TDSE) is solved directly using the time-dependent close-coupling method with the Hamiltonian H introduced in the previous section [Eq. (2.2)] in either length or velocity gauge. The wave function in coordinate space is expanded using coupled spherical harmonics [28]

$$\Psi(\mathbf{r}_1, \mathbf{r}_2, t) = \sum_{L,M}^{\infty} \sum_{\ell_1,\ell_2}^{\infty} \frac{R^{LM}_{\ell_1,\ell_2}(r_1, r_2, t)}{r_1 r_2} \mathcal{Y}^{LM}_{\ell_1,\ell_2}(\Omega_1, \Omega_2), \tag{2.8}$$

with

$$\mathcal{Y}^{LM}_{\ell_1,\ell_2}(\Omega_1, \Omega_2) = \sum_{m_1,m_2} \langle \ell_1 m_1 \ell_2 m_2 | \ell_1 \ell_2 L M \rangle Y^{\ell_1}_{m_1}(\Omega_1) Y^{\ell_2}_{m_2}(\Omega_2), \tag{2.9}$$

where $\langle \ell_1 m_1 \ell_2 m_2 | \ell_1 \ell_2 L M \rangle$ are the Clebsch-Gordan coefficients and $Y^l_m(\Omega)$ the spherical harmonics. For linear polarized laser fields the Hamiltonian is cylindrical symmetric and M is conserved. The radial functions $R^{LM}_{\ell_1,\ell_2}(r_1, r_2)$ are discretized using the finite-element discrete-variable-representation [54, 55], see App. A.

2.2.1. Equations of motion

Inserting Eq. (2.8) into the TDSE [Eq. (2.1)] results in the following equations of motion

$$
\begin{aligned}
i\frac{\partial}{\partial t}R^{L,M}_{\ell_1,\ell_2}(r_1,r_2,t) = &\left[-\frac{1}{2}\left(\frac{\partial^2}{\partial r_1^2}+\frac{\partial^2}{\partial r_2^2}\right)-\frac{2}{r_1}-\frac{2}{r_2}\right)\right] R^{L,M}_{\ell_1,\ell_2}(r_1,r_2,t) \\
&+\sum_{\ell_1',\ell_2',L',M'} V^{L,M,L',M'}_{\ell_1,\ell_2,\ell_1',\ell_2'}(r_1,r_2,t) R^{L',M'}_{\ell_1',\ell_2'}(r_1,r_2,t) \\
&+\sum_{\ell_1',\ell_2'} W^{L}_{\ell_1,\ell_2,\ell_1',\ell_2'}(r_1,r_2) R^{L,M}_{\ell_1',\ell_2'}(r_1,r_2,t),
\end{aligned}
\tag{2.10}
$$

consisting of, in principle, infinitely many coupled partial differential equations, which will be limited in the practical case to the relevant partial waves only. $V^{L,M,L',M'}_{\ell_1,\ell_2,\ell_1',\ell_2'}(r_1,r_2,t)$ describes the interaction with the laser field in either length or velocity gauge and $W^{L}_{\ell_1,\ell_2,\ell_1',\ell_2'}(r_1,r_2)$ the electron-electron interaction (for more details see [29, 30]).

2.3. Laser polarization

In this work we employ linearly and elliptically polarized laser pulses of both positive and negative helicity. Throughout this thesis, linearly polarized pulses are always polarized in $\hat{z}$ direction

$$
\mathbf{A}_{\text{lin}}(t) = A_0 f(t) \begin{pmatrix} 0 \\ 0 \\ \cos(\omega t) \end{pmatrix}, \tag{2.11}
$$

where $f(t)$ is the envelope function and $I = A_0^2$ the peak intensity. Elliptically polarized laser pulses are polarized within the $\hat{x}$-$\hat{y}$ plane

$$
\mathbf{A}_{\text{ell}}(t) = A_0 f(t) \frac{1}{\sqrt{1+\epsilon^2}} \begin{pmatrix} \sin(\omega t) \\ \epsilon \cos(\omega t) \\ 0 \end{pmatrix}, \tag{2.12}
$$

with ϵ being the ellipticity. The employed envelope functions are specified in App. B.1. Right-hand helicity ($\epsilon = -1$) corresponds to photons with a magnetic quantum number $m_\gamma = +1$ where m is the projection of the photon spin onto the direction of propagation [31]. It is equivalent to left circular polarization (LCP) as the polarization vector rotates counter-clockwise for an observer looking towards the source. For left-hand helicity ($\epsilon = -1$) or right circular polarization (RCP) the polarization vector consequently rotates clockwise.

3. Extraction of double ionization spectra

In this chapter we describe in detail how the fully differential cross section is extracted from the time-dependent wave function and define the observables referred to throughout this thesis.

3.1. Fully differential double ionization probability

In order to extract the fully differential double ionization probability distribution $P(\mathbf{k}_1, \mathbf{k}_2)$ at the end of the time propagation we would need to project the fully correlated two electron wave function onto eigenstates of the full field-free Hamiltonian. The full Hamiltonian [Eq. (2.2)], is however, non-separable due to the electron-electron interaction term and numerical diagonalization is computationally expensive and challenging due to boundary conditions. To circumvent this problem we resort to final states that only represent the true eigenstates in the asymptotic region. Thus, we neglect the electron-electron interaction $|\mathbf{r}_1 - \mathbf{r}_2|^{-1}$. This implies that the distance between the electrons has to be sufficiently large for this approximation to be reasonable, resulting in long propagation times after the end of the pulse to obtain converged results [29].

3.1.1. Coulomb waves

After the interaction of the atom with the laser pulse has ended and the electrons are sufficiently separated the electron-electron interaction can be neglected. The resulting Hamiltonian is separable into two independent one-particle Hamiltonians

$$H_i = \frac{\mathbf{k}_i^2}{2} - \frac{2}{r_i}. \tag{3.1}$$

The unbound solutions of Eq. (3.1) are given by [32]

$$\Phi_{k,\ell,m} = \sqrt{\frac{2}{\pi}} \frac{F_\ell(\eta, kr)}{r} Y_m^\ell(\Omega), \tag{3.2}$$

where $F_\ell(\eta, kr)$ is the radial Coulomb function, given by

$$F_\ell(\eta, kr) = 2^\ell \mathrm{e}^{-\frac{1}{2}\pi\eta} \frac{|\Gamma(\ell + 1 + \mathrm{i}\eta)|}{(2\ell+1)!} \mathrm{e}^{-ikr} (kr)^{\ell+1} \mathrm{F}(\ell + 1 - \mathrm{i}\eta, 2\ell + 2; 2\mathrm{i}kr), \tag{3.3}$$

with the Coulomb parameter $\eta = -Z_{\mathrm{eff}}/k$. The confluent hypergeometric function F is in the

limit $r \to \infty$ given by

$$\mathrm{F}(\ell+1-\mathrm{i}\eta, 2\ell+2; 2\mathrm{i}kr) \to \sin\left(kr - \eta\ln 2kr - \frac{\ell\pi}{2} + \sigma_\ell\right), \tag{3.4}$$

where $\sigma_\ell = \arg[\Gamma(\ell+1+i\eta)]$ is the Coulomb phase shift. To calculate angular distributions, we sum over all angular momentum quantum numbers

$$\psi_{\mathbf{k}}(\mathbf{r}) = \sum_{\ell=0}^{\infty}\sum_{m=-\ell}^{\ell} \mathrm{i}^\ell \mathrm{e}^{-i\sigma_l} Y_m^{\ell *}(\Omega_k)\sqrt{\frac{2}{\pi}} F_\ell(\eta, kr). \tag{3.5}$$

The double continuum wave function for $\mathbf{k}_1 \neq \mathbf{k}_2$ is constructed as

$$\Psi^{\mathrm{DC}}_{\mathbf{k}_1,\mathbf{k}_2}(\mathbf{r}_1,\mathbf{r}_2) = \frac{1}{\sqrt{2}}[\psi_{\mathbf{k}_1}(\mathbf{r}_1)\psi_{\mathbf{k}_2}(\mathbf{r}_2) + \psi_{\mathbf{k}_1}(\mathbf{r}_2)\psi_{\mathbf{k}_2}(\mathbf{r}_1)]. \tag{3.6}$$

To obtain the fully differential double ionization probability the time dependent wave function $|\Psi(t)\rangle$ is projected onto the asymptotic eigenfunction [Eq.(3.6)]

$$P(\mathbf{k}_1,\mathbf{k}_2) = P(k_1,k_2,\Omega_{k,1},\Omega_{k,2}) = |\langle\Psi^{\mathrm{DC}}_{\mathbf{k}_1,\mathbf{k}_2}(\mathbf{r}_1,\mathbf{r}_2)|\Psi(t)\rangle|^2. \tag{3.7}$$

Using energy-normalized Coulomb functions instead of Eq. (3.2) results in the energy differential distribution

$$P(E_1,E_2,\Omega_1,\Omega_2) = \frac{\mathrm{d}k_1}{\mathrm{d}E_1}\frac{\mathrm{d}k_2}{\mathrm{d}E_2}P(k_1,k_2,\Omega_1,\Omega_2) = \frac{1}{k_1k_2}P(k_1,k_2,\Omega_1,\Omega_2). \tag{3.8}$$

3.1.2. Volkov waves

The major disadvantage of projecting onto Coulomb waves to calculate the observables of interest is the necessity that the electrons are spatially well separated. Thus, long after pulse propagation times and, numerically even more demanding, large boxes for the radial coordinates of the electrons are needed. Together with the fact that for laser pulses with high wavelengths it is necessary to include many angular momentum channels in the calculation to achieve convergence, numerical calculations are no longer feasible. To circumvent this problem it is possible to not only project at the end of propagation but also at several times during propagation even before the end of the laser pulse, opening the possibility to use much smaller boxes.

For each projection time t_p we split the radial part of the wave function $\Psi(t_p)$ into an inner part $\Psi_{\mathrm{inner}}(t_p)$ and an outer part $\Psi_{\mathrm{outer}}(t_p)$ (Fig. 3.1)

$$\Psi(t_\mathrm{p}) = \Psi_{\mathrm{inner}}(t_p) + \Psi_{\mathrm{outer}}(t_p) = M\Psi(t_\mathrm{p}) + (1-M)\Psi(t_\mathrm{p}) \tag{3.9}$$

with the mask function

$$M = \frac{1}{4}[1+\mathrm{erf}(r_{\mathrm{cut}}-r_1)][1+\mathrm{erf}(r_{\mathrm{cut}}-r_2)]\Theta(r_{\mathrm{cut}}-r_1)\Theta(r_{\mathrm{cut}}-r_2) \tag{3.10}$$

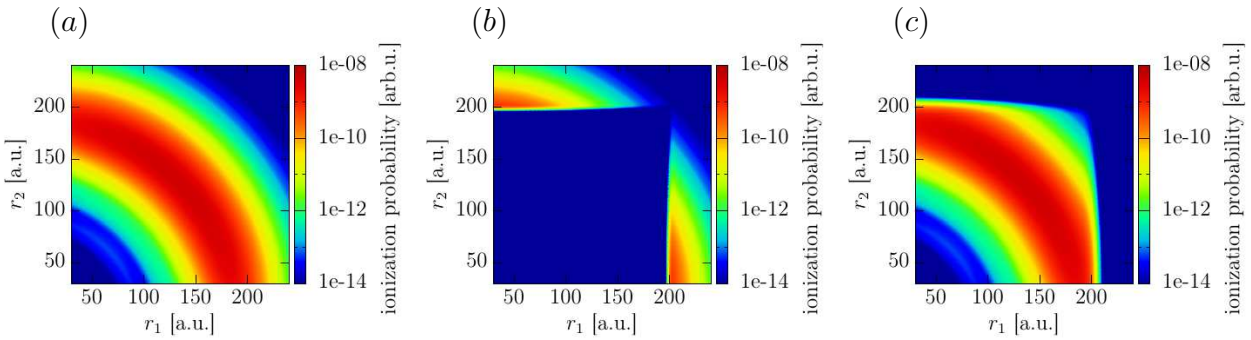

Figure 3.1.: (a) $|\Psi(r_1, r_2, t_\mathrm{p})|^2$ with $t_\mathrm{p} = 4$ fs for a laser pulse with a wave length of $\lambda = 12.5$ nm ($\omega = 99$ eV) and a FWHM duration of $T = 0.5$ fs. (b) Outer part $|\Psi_\mathrm{outer}(r_1, r_2, t_p)|^2$ and (c) inner part $|\Psi_\mathrm{inner}(r_1, r_2, t_p)|^2$ from Eq. (3.9) for a cut-off radius $r_\mathrm{cutoff} = 200$ a.u..

where $\mathrm{erf}(x)$ is the Gauss error function, Θ the Heaviside step function and r_cut the cut-off radius.

The inner part is used as the starting point for further numerical propagation up to the next projection time t_p, while the outer part is analytically propagated to the end of time propagation. For large enough radii the Coulomb potential of the ion can be neglected resulting in the one particle Hamiltonian

$$H_i = \frac{\mathbf{k}_i^2}{2} + \mathbf{k}_i \cdot \mathbf{A}(t) + \frac{\mathbf{A}(t)^2}{2}. \tag{3.11}$$

The solutions to Eq. (3.11) are the Volkov wave functions [33, 34]

$$\chi_\mathbf{k}^\mathrm{Volkov}(\mathbf{r}, t) = (2\pi)^{-3/2} \exp\left[\mathrm{i}\mathbf{k}\mathbf{r} - \mathrm{i}\frac{k^2 t}{2} - \mathrm{i}\Phi^\mathrm{Volkov}(\mathbf{k}, t)\right], \tag{3.12}$$

which differ from plane waves only by the Volkov phase

$$\Phi^\mathrm{Volkov}(\mathbf{k}, t) = \mathbf{k}\int_{-\infty}^{t} \mathrm{d}\tau \mathbf{A}(\tau) + \int_{-\infty}^{t} \mathrm{d}\tau \frac{\mathbf{A}^2(\tau)}{2}. \tag{3.13}$$

Thus, for each time t_p we project the outer part of the wave function $\Psi_\mathrm{outer}(t_\mathrm{p})$ onto Coulomb waves, as they differ only marginally from plane waves for $r > r_\mathrm{cut}$, and account for the analytic propagation with an additional phase

$$\Phi^\mathrm{ana}(\mathbf{k}, t_\mathrm{p}, t_\mathrm{end}) = \frac{k^2(t_\mathrm{end} - t_\mathrm{p})}{2} + \mathbf{k}\int_{t_\mathrm{p}}^{t_\mathrm{end}} \mathrm{d}\tau \mathbf{A}(\tau) + \int_{t_\mathrm{p}}^{t_\mathrm{end}} \mathrm{d}\tau \frac{A^2(\tau)}{2}. \tag{3.14}$$

This avoids the loss of information through absorption at the boundaries of the radial grid otherwise unavoidable when small boxes are used.
At the end of propagation t_end all the parts are summed up with the correct phase

$$P(\mathbf{k}_1, \mathbf{k}_2) = \left| \sum_{t_p} \langle \Psi_{\mathbf{k}_1,\mathbf{k}_2}^\mathrm{DC} | \Psi_\mathrm{outer}(t_p) \rangle \mathrm{e}^{-\mathrm{i}\Phi^\mathrm{ana}(\mathbf{k}_1) - \mathrm{i}\Phi^\mathrm{ana}(\mathbf{k}_2)} + \langle \Psi_{\mathbf{k}_1,\mathbf{k}_2}^\mathrm{DC} | \Psi(t_\mathrm{end}) \rangle \right|^2. \tag{3.15}$$

Using this method we neglect both the electron-core and the electron-electron interaction. Thus, it is important that the cutoff radius is large enough that the errors from these approximations are negligible.

3.2. Double ionization observables

With the fully differential DI probability [Eq. (3.15)] as starting point, we derive several observables which will be used and referred to throughout this thesis. Integrating over the solid angles in Eq. (3.8) results in the joint energy probability distribution

$$P(E_1, E_2) = \int_0^{4\pi} \int_0^{4\pi} \mathrm{d}\Omega_1 \, \mathrm{d}\Omega_2 \, P(E_1, E_2, \Omega_1, \Omega_2). \tag{3.16}$$

Performing the energy coordinate transformation to the total energy $E_{\mathrm{tot}} = E_1 + E_2$ and the energy difference $\Delta E = E_1 - E_2$ results in

$$P(E_{\mathrm{tot}}, E_\Delta) = \frac{1}{2} P(E_1, E_2). \tag{3.17}$$

Further integration results in the singly differential DI probabilities

$$P(E_{\mathrm{tot}}) = \int \mathrm{d}\Delta E P(E_{\mathrm{tot}}, \Delta E) \tag{3.18}$$

and

$$P(\Delta E) = \int \mathrm{d}E_{\mathrm{tot}} P(E_{\mathrm{tot}}, \Delta E). \tag{3.19}$$

Integrating Eq. (3.16) over both energies yields the total double ionization yield

$$P^{\mathrm{DI}} = \int \int \mathrm{d}E_1 \, \mathrm{d}E_2 \, P(E_1, E_2). \tag{3.20}$$

The generalized n_{ph}-photon cross section for DI [35] is given by

$$\sigma_{n_{\mathrm{ph}}} \approx \left(\frac{\omega}{I}\right)^{n_{\mathrm{ph}}} \frac{1}{T_{\mathrm{eff}}} P^{\mathrm{DI}}, \tag{3.21}$$

where I is the peak intensity of the ionizing pulse and the effective duration T_{eff} is defined as

$$T_{\mathrm{eff}} = \int_{-\infty}^{\infty} \mathrm{d}t \, f(t)^{2n_{\mathrm{ph}}}, \tag{3.22}$$

with $f(t)$ being the time dependent envelope function of the vector potential of the ionizing pulse.
An efficient way to study electron correlations for double ionization processes is to reduce the fully differential DI probability Eq. (3.8) to two angular parameters, resulting in the joint-angular distribution (JAD) [11, 36, 37]. In order to obtain the JAD we either choose for both

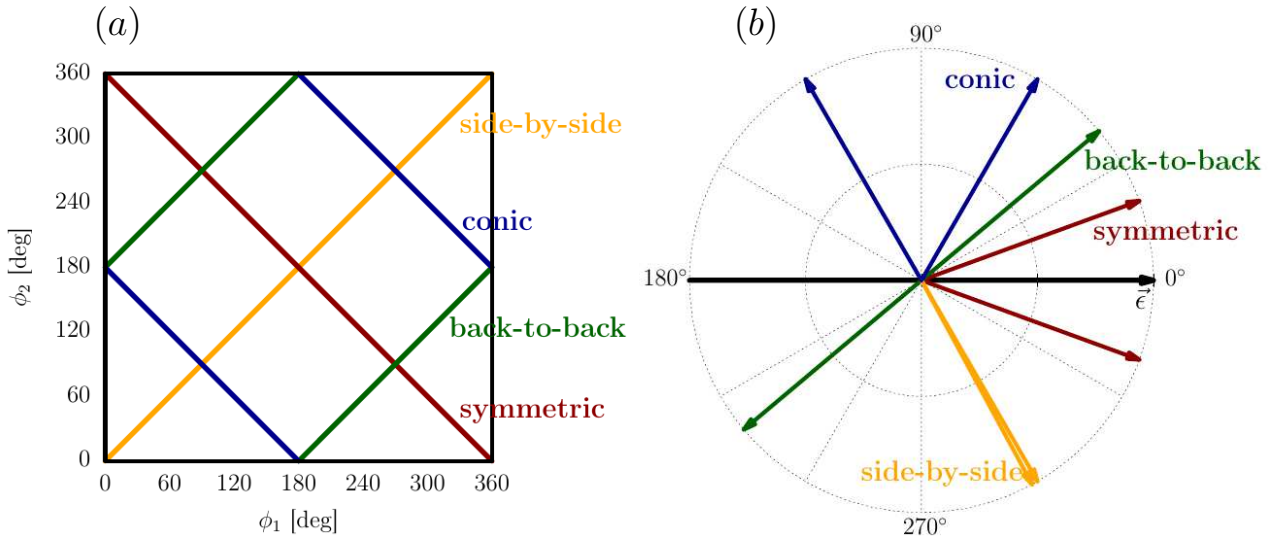

Figure 3.2.: Schematic representation of the angular distributions. (a) The angles $\Phi_{1,2}$ correspond to $\theta_{1,2}$ for linear polarized laser pulses and to $\varphi_{1,2}$ for circular polarized pulses. The coloured lines represent specific emission patterns of interest and shown in (b) are examples of the angular patterns in the $\hat{z}$-$\hat{x}$ plane for linear polarization and in the $\hat{x}$-$\hat{y}$ plane for circular polarization. For circular polarization only side-by-side and back-to-back are relevant as there is no distinct direction in the $\hat{x}$-$\hat{y}$ plane.

electrons the same energy (equal-energy sharing) or the energy of one electron to nearly the total energy (asymmetric energy sharing). For linear polarized pulses (polarization direction $\hat{z}$) due to the cylindrical symmetry the DI probability does not depend on the azimuthal angles, and are chosen $\varphi = 0$ for $\theta < 180°$ or $\varphi = 180°$ for $\theta > 180°$. Within this thesis for circularly polarized pulses (polarization direction in the $\hat{x}$-$\hat{y}$ plane) the polar angles are of less relevance and are chosen as $\theta_1 = \theta_2 = 90°$.

The JAD allows to distinguish four electron emission patterns for linear polarization [36] (Fig. 3.2): back-to-back emission ($|\theta_1 - \theta_2| = 180°$), side-by-side emission ($\theta_1 = \theta_2$), conic emission ($\theta_1 + \theta_2 = 180°$) and symmetric emission ($\theta_1 + \theta_2 = 360°$). For circular polarization back-to-back emission ($|\varphi_1 - \varphi_2|$) and side-by-side emission with ($\varphi_1 = \varphi_2$) can be distinguished. As there is no distinct direction in the $\hat{x}$-$\hat{y}$ plane conic and symmetric emission can not be identified for emission within the polarization plane.

4. One-photon double ionization

One-photon double ionization (OPDI)

$$\omega_{\mathrm{XUV}} + \mathrm{He} \rightarrow \mathrm{He}^{2+} + e^- + e^- \tag{4.1}$$

is the prime example to observe electron correlation effects, as the quantized photon energy has to be shared between both electrons via the electron-electron interaction for DI to occur. In order to achieve one-photon double ionization the carrier frequency of the laser pulse ω_{XUV} has to be larger than the groundstate energy of helium (79.01 eV).
Over the years two different processes have been distinguished for OPDI [38]. In the so called shake-off process [39], one electron alone absorbs the photon and is swiftly ionized. This causes a sudden change in the effective nuclear charge which leads to the ionization of the second electron, as the wave function of the second electron can not adapt to the new nuclear potential and is thus shaken off. This process results in one fast and one very slow electron. The second mechanism identified for one-photon double ionization is called "knockout" [40]. After being ionized the electron is driven back to the core by the field and kicks out the second electron via a hard binary collision. A classical collision between two bodies with the same mass would lead to a preferred angle of $\pi/2$ between the two electrons.
A potential process where both electrons simultaneously share the photon and leave the ion with similar energies but in opposite directions is forbidden for OPDI. As electrons are indistinguishable this would imply $P(\mathbf{k}_1, \mathbf{k}_2) = P(\mathbf{k}_2, \mathbf{k}_1)$, but according to the parity of coupled spherical harmonics

$$\hat{\Pi} \mathcal{Y}^{LM}_{\ell_1,\ell_2}(\Omega_1, \Omega_2) = (-1)^{l_1+l_2} \mathcal{Y}^{LM}_{\ell_1,\ell_2}(\Omega_1, \Omega_2) \tag{4.2}$$

only a final state with odd parity is allowed when an odd number of photons is absorbed. Thus, this process is only allowed when an even number of photons are absorbed.
In the following we compare OPDI for linearly and elliptically polarized laser pulses. In agreement with many experiments we choose a pulse with $\omega_{\mathrm{XUV}} = 99$ eV ($\lambda = 12.5$ nm) resulting in a total excess energy of ~ 20 eV for both electrons upon OPDI. The numerical parameters are given in App. B.2. The pulse intensity ($I_{\mathrm{XUV}} = 10^{14}$ W/cm^2) is weak enough for groundstate depletion to be negligible.

4.1. Angle integrated double ionization spectra

The angle-integrated DI probability $P(E_1, E_2)$ [Eq. (3.16)] is independent of the laser polarization [Fig. 4.1(a)]. Consequently, $P(\Delta E)$ [Eq. (3.19)] is indistinguishable for both laser polarizations employed, the only difference is the slightly higher (0.02 %) total DI probability for

circular polarization [Fig. 4.1(b)]. The shake-off process is the dominant DI mechanism [black arrows in Fig. 4.1(b)], while the knockout process is dominant at $\Delta E = 0$ [38].

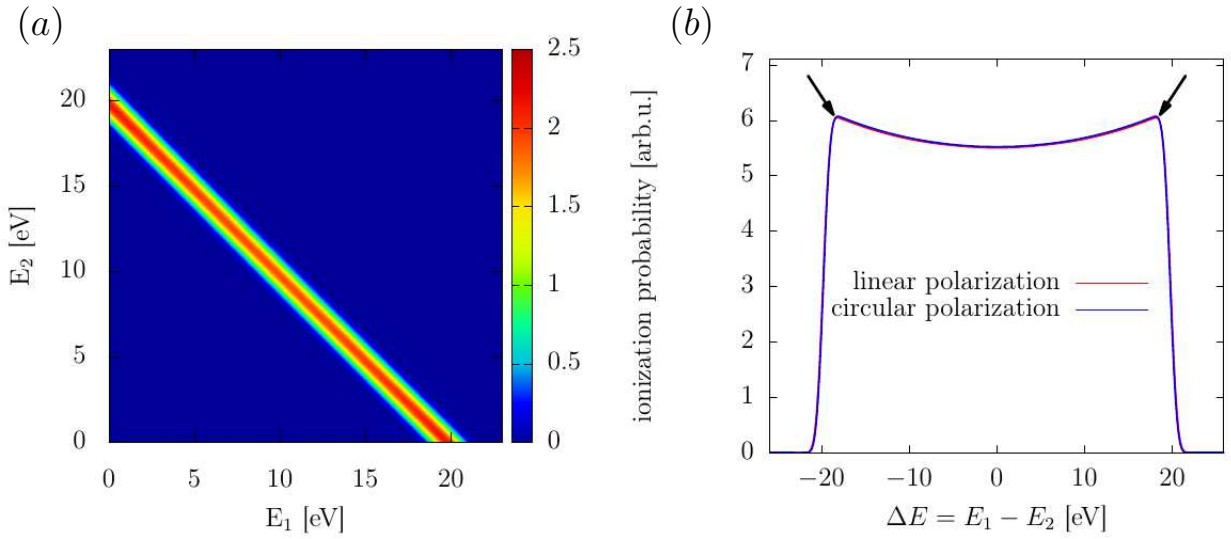

Figure 4.1.: (a) Doubly differential photoelectron spectrum $P(E_1, E_2)$ [Eq. (3.16)] for a laser pulse with a wave length of $\lambda = 12.5$ nm and a FWHM duration of $T = 2$ fs. (b) Spectrum for linear and for circular polarization, integrated over the total energy $E_{\text{tot}} = E_1 + E_2$ [Eq. (3.19)].

4.2. Angular and momentum distributions

To study the imprint of Coulomb correlation and parity conservation on the double ionization process we focus on angular and momentum distributions. We investigate DI by laser pulses with linear polarization and with elliptical polarization separately.

4.2.1. Linear polarization

Detailed insight into the double ionization process can be gained from joint momentum distributions. Integrating the momentum distribution [Eq. (3.7)] over the momenta perpendicular to the laser polarization direction

$$P(k_{\parallel,1}, k_{\parallel,2}) = \iiiint \mathrm{d}k_{x,1}\mathrm{d}k_{x,2}k_{y,1}\mathrm{d}k_{y,2}\ P(\mathbf{k}_1, \mathbf{k}_2), \tag{4.3}$$

reveals that the signs of the momentum components parallel to the polarization direction ($p_\parallel$) coincide for almost the full probability distribution [Fig. 4.2(a)].
This seems to contradict the assumption that the electron-electron interaction should suppress the emission of electrons into the same direction. This apparent contradiction is resolved by the joint momentum spectrum perpendicular to the laser polarization [Fig. 4.2(b)]

$$P(k_{\perp,1}, k_{\perp,2}) = \iiiint \mathrm{d}k_{y,1}\mathrm{d}k_{y,2}\mathrm{d}k_{z,1}\mathrm{d}k_{z,2}\ P(\mathbf{k}_1, \mathbf{k}_2). \tag{4.4}$$

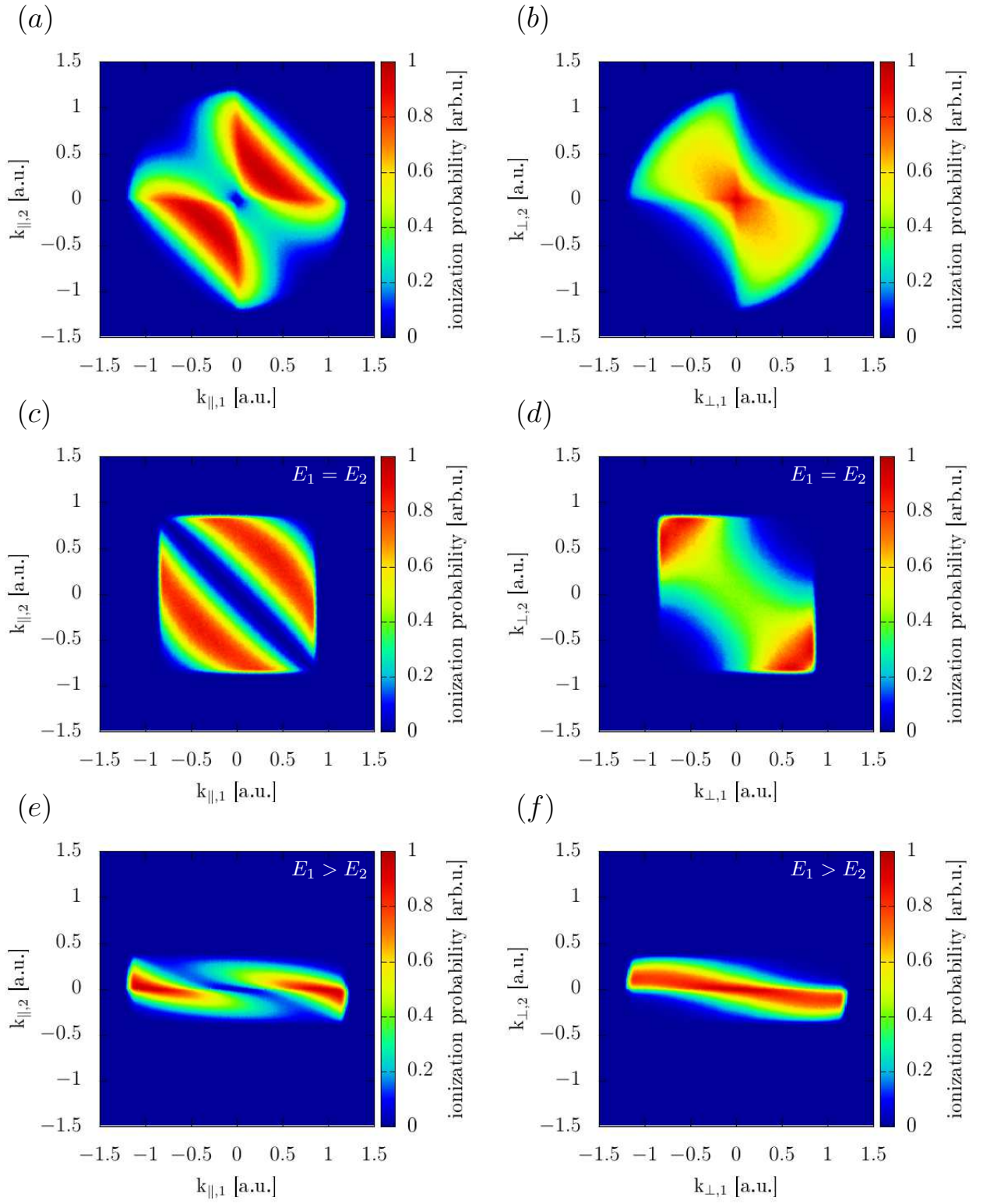

Figure 4.2.: Electron momentum spectrum for a linear polarized laser pulse in one spatial direction, integrated over the other momenta. Left column: Electron momenta parallel to the laser polarization, in z-direction [Eq. (4.3)]. Right column: Momenta perpendicular to the laser polarization, in x-direction [Eq. (4.4)]. $(a), (b)$ Integrated over all energies. $(c), (d)$ For equal-energy sharing, $E_1 = E_2$. $(e), (f)$ For completely asymmetric energy sharing, $(E_1 - E_2)/(E_1 + E_2) > 0.9$.

The electrons are primarily ionized in opposite directions ($k_{\perp,1} = -k_{\perp,2}$), indicating that "knockout" is the primary ionization mechanism. Thus, the electrons leave with opposite perpendicular momenta on a cone along the polarization axis.
Restricting the full momentum distribution to certain energy regions for the two electrons allows us to obtain even more insights. While the conditional momentum distribution for both electrons having the same final energy (equal-energy sharing) is very similar to the unrestricted momentum distribution for the parallel momentum component [Fig. 4.2(c)], the perpendicular distribution Eq. (4.4) clearly shows that the Coulomb repulsion pushes the electrons apart [Fig. 4.2(d)]. Contrary to Fig. 4.2(b), the most probable cases are for large $p_\perp$. For strongly asymmetric energy sharing ($(E_1 - E_2)/(E_1 + E_2) > 0.9$) $p_\parallel$ and $p_\perp$ have opposite sign for both electrons, indicating emission in opposite direction [Fig. 4.2(e, f)]. Complementary to momentum distributions the JAD reveals that conic and back-to-back emission are completely forbidden due to parity conservation for equal-energy sharing (Fig. 4.3(a)). Additionally, side-by-side emission is suppressed due to the repulsive Coulomb interaction. The most probable scenario is symmetric emission with a relative angle of $\theta_1 - \theta_2 = 120°$ and $\theta_1 - \theta_2 = 240°$. For equal-energy sharing and $\theta = 0$ parity conservation combined with the suppressed side-by-side emission [41] leads to the well-known "butterfly" shape in the angular distribution with a preferred relative angle of around $\theta_2 = 120°$ [Fig. 4.3(b)].
For asymmetric energy sharing with $E_1 = 19$ eV and $E_2 = 1$ eV a similar picture emerges for the angular correlation [Fig. 4.3(c)] with the difference that back-to-back emission is no longer strictly forbidden. Interestingly, for $\theta_1 = 0°$ [Fig. 4.3(d)] back-to-back is the most likely scenario.

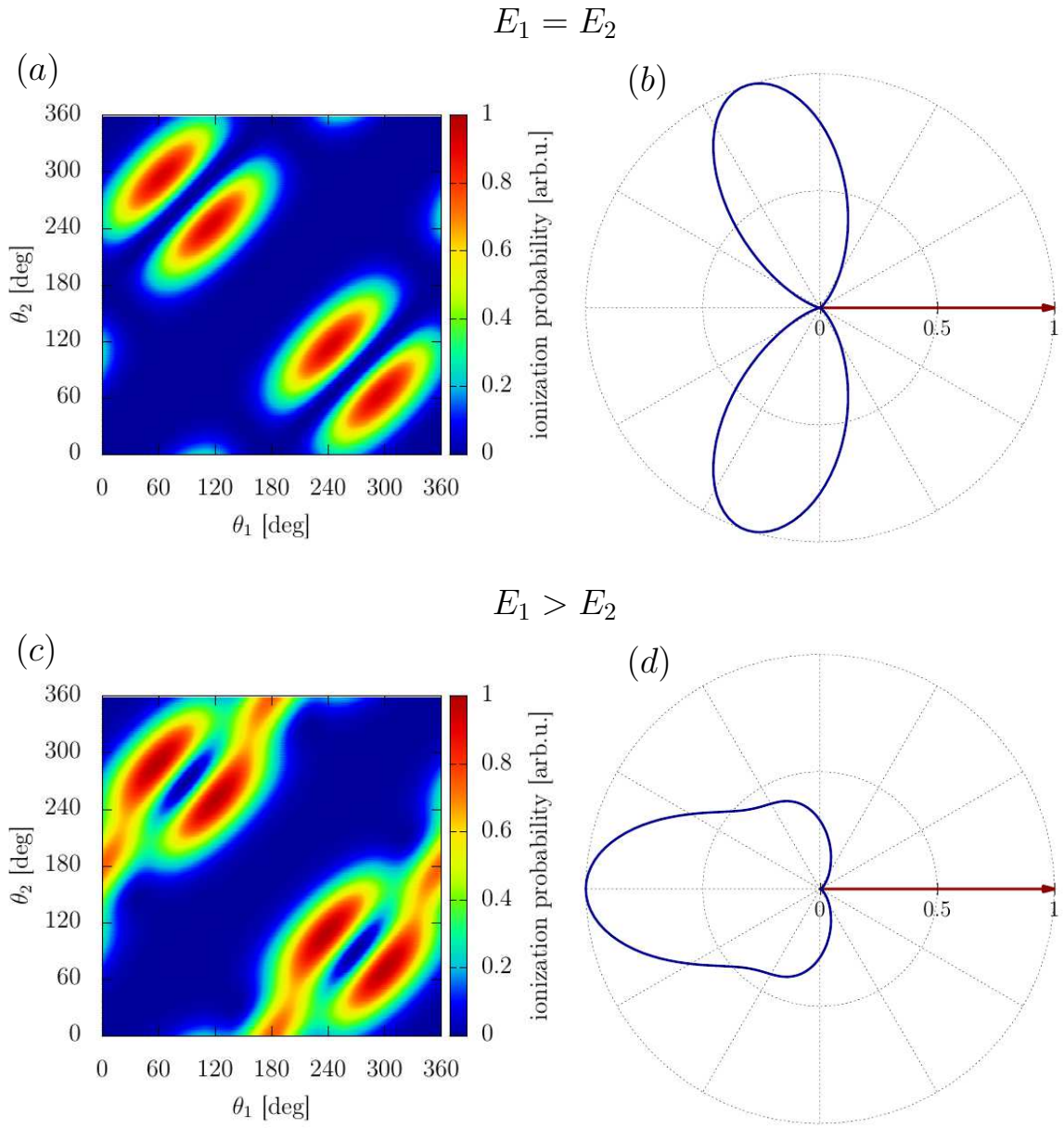

Figure 4.3.: Left column: Joint-angular distribution (JAD) in the polarization plane for a linear polarized laser pulse with a wave length of $\lambda = 12.5$ nm, a FWHM duration of $T = 2$ fs and a peak intensity of $I = 10^{14}$ W/cm^2. θ is measured relative to the polarization direction for (a) equal-energy sharing ($E_1 = E_2 = 10$ eV) and for (c) a completely asymmetric energy distribution between the electrons ($E_1 = 19$ eV and $E_2 = 1$ eV). Right Column: Cut through the JAD at $\theta_1 = 0$ for (b) equal-energy sharing ($E_1 = E_2 = 10$ eV) and for (d) a completely asymmetric energy distribution between the electrons ($E_1 = 19$ eV and $E_2 = 1$ eV). The direction of the first electron is marked by the red arrow ($\theta_1 = 0$ and $\varphi_1 = 0$) in (b) and (d). The angle in the polar plot is then consequently the angle $\theta_1 - \theta_2$ between the two electrons and the radial coordinate gives the ionization probability.

4.2.2. Circular polarization

As shown before, the photoelectron spectrum for ionization by circularly polarized pulses differs in no way from the case of linear polarized light, since it is integrated over the solid angles of both electrons and differences between linear and circular polarized light emerge most prominently in angle resolved observables. Thus, the angular distribution for equal-energy sharing and strongly asymmetric energy sharing reveals drastic differences in the emission patterns which depend on the ellipticity of the ionizing pulse. For equal-energy sharing the relative angle between the lobes decreases continuously with increasing ϵ while back-to-back emission is still suppressed [Fig. 4.4(a,b)].
The JAD for equal-energy sharing and a circularly polarized laser pulse [Fig. 4.4(c)] shows even more drastic differences compared to the case of linear polarization [Fig. 4.3(a)]. As there is no preferred ionization direction within the polarization plane, the emission probability depends only on the relative angle $\varphi_1 - \varphi_2$ and clearly shows that back-to-back emission is forbidden by parity and maxima are located at $|\varphi_1 - \varphi_2| = 128°$. For asymmetric energy sharing the qualitative shape of the angular distribution changes and a preferential emission direction can clearly be identified [Fig. 4.5]. This preferred emission angle depends strongly on the helicity of the ionizing pulse as is revealed by the so called circular dichroism

$$CD(\varphi_1, \varphi_2) = \frac{\sigma^+(\varphi_1, \varphi_2) - \sigma^-(\varphi_1, \varphi_2)}{\sigma^+(\varphi_1, \varphi_2) + \sigma^-(\varphi_1, \varphi_2)}, \tag{4.5}$$

where $\sigma^+(\varphi_1, \varphi_2)$ is the ionization probability for circular polarized light with $\epsilon = +1$ (RCP) and $\sigma^-(\varphi_1, \varphi_2)$ for $\epsilon = -1$ (LCP). Circular dichroism is a visible consequence of the rotation of the electric field vector of the circularly polarized light which results in a torque of the motion of the electron pair [19]. This can clearly be seen in the angular distribution [Fig. 4.5(a)] where for positive helicity the angle $\varphi_2 = 147°$ is preferred and for negative helicity $\varphi_2 = 213°$ is preferred. A chiral initial state is not a necessity for circular dichroism to emerge and even a spherical symmetric groundstate (as for OPDI of helium) is no hindrance. The only necessary condition is that the two electron momentum vectors and the light propagation axis span a tripod with a defined handedness [20]. For equal-energy sharing two legs of this tripod are indistinguishable and thus circular dichroism is absent. Calculating the CD for the full JAD for asymmetric energy sharing we clearly observe a strong signal which is maximal at the maxima of the respective angular distributions [Fig. 4.5(b)].
To further investigate circular dichroism of OPDI for asymmetric energy sharing we study the angular distribution as a function of ellipticity ϵ, pulse energy ω_{XUV} and pulse duration T. The asymmetric emission visible for $\epsilon = +1$ (RCP) continuously changes with decreasing ellipticity to the shape observed for linear polarization [Fig. 4.6(a)]. Comparison of experimental data with theoretical calculations could thus, in principle, be used to measure the ellipticity of the used XUV. While the angular distribution is not sensitive to the pulse duration [Fig. 4.6(b)] it depends strongly on the pulse energy [Fig. 4.7(a)]. The CD angle decreases gradually [Fig. 4.7(b)] and we expect it to become 0 for $\omega_{\mathrm{XUV}} \to \infty$. Simultaneously, the amplitude of the smaller side lobe decreases. The diminishing of the CD can be attributed to the shorter time the electrons have to interact with each other for increased energy. Similar effects have also been shown for the imprint of Coulomb correlation onto the angular distribution for two-photon DI [11].

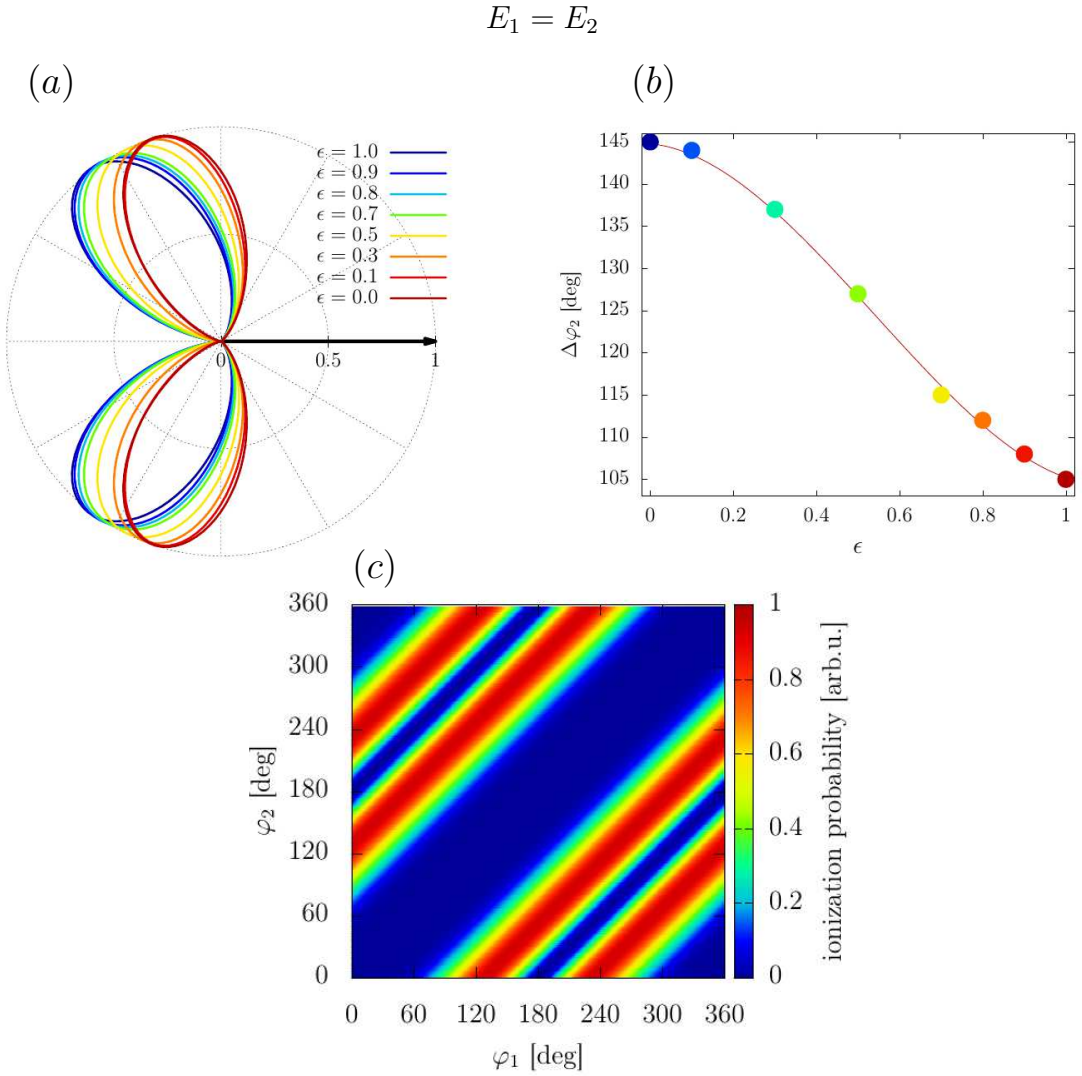

Figure 4.4.: OPDI for elliptically polarized laser pulses with polarization direction in the $\hat{x}$-$\hat{y}$ plane, a wave length of $\lambda = 12.5$ nm, a FWHM duration of $T = 4$ fs and equal-energy sharing between the two electrons ($E_1 = E_2 = 10$ eV). (a) Angular distributions ($\theta_1 = \theta_2 = 90°, \varphi_1 = 0$) for different elliptical polarizations of the laser pulse. Direction of the first electron is marked by the black arrow, corresponding to $\theta = \pi/2$ and $\varphi = 0$. (b) Relative angle between the two lobes of (a) as function of ellipticity. (c) JAD for $\epsilon = 1$.

$E_1 > E_2$

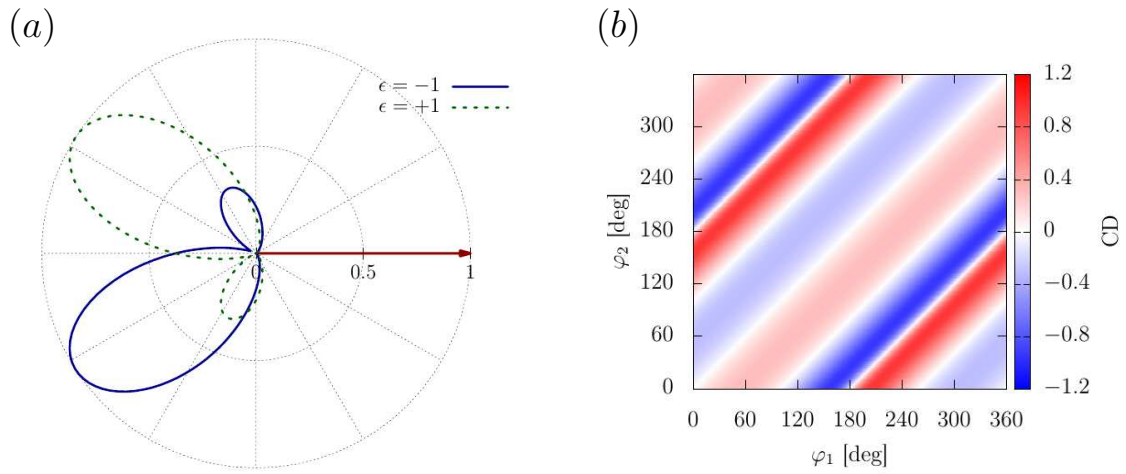

Figure 4.5.: OPDI for a circularly polarized laser pulse with polarization direction in the $\hat{x}$-$\hat{y}$ plane, a wave length of $\lambda = 12.5$ nm, a FWHM duration of $T = 4$ fs and completely asymmetric energy sharing between the two electrons ($E_1 = 19$ eV, $E_2 = 1$ eV). (a) Angular distribution ($\theta_1 = \theta_2 = 90°, \varphi_1 = 0$) for LCP and RCP laser pulses. The direction of the first electron is marked by the black arrow. (b) Circular dichroism as function of φ_1 and φ_2.

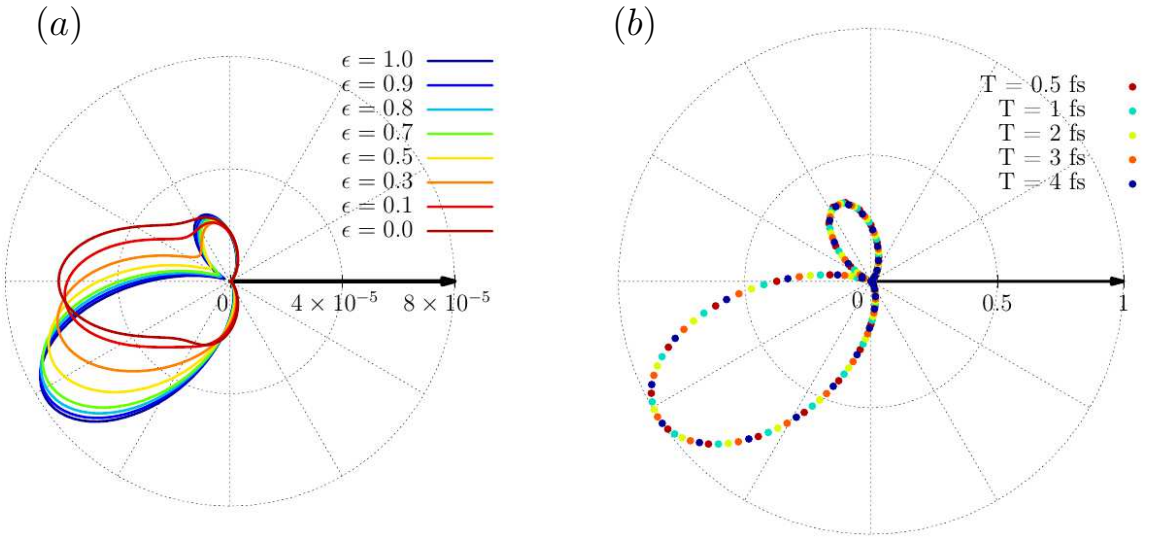

Figure 4.6.: Angular distributions ($\theta_1 = \theta_2 = 90°, \varphi_1 = 0$) within the $\hat{x}$-$\hat{y}$ plane. The direction of the first electron is marked by the black arrow ($\theta_1 = \pi/2$ and $\varphi_1 = 0$). (a) Ionization by elliptically polarized light with polarization in the $\hat{x}$-$\hat{y}$ plane, a FWHM pulse duration of 2 fs, a photon energy of 99 eV and varying degrees of ellipticity. $\epsilon = 1$ corresponds to circularly polarized light with negative helicity (RCP) and $\epsilon = 0$ to linearly polarized light in $\hat{x}$ direction. (b) Ionization by circularly polarized light with negative helicity, a photon energy of 99 eV and varying total pulse durations. The distributions are normalized to their maximal value.

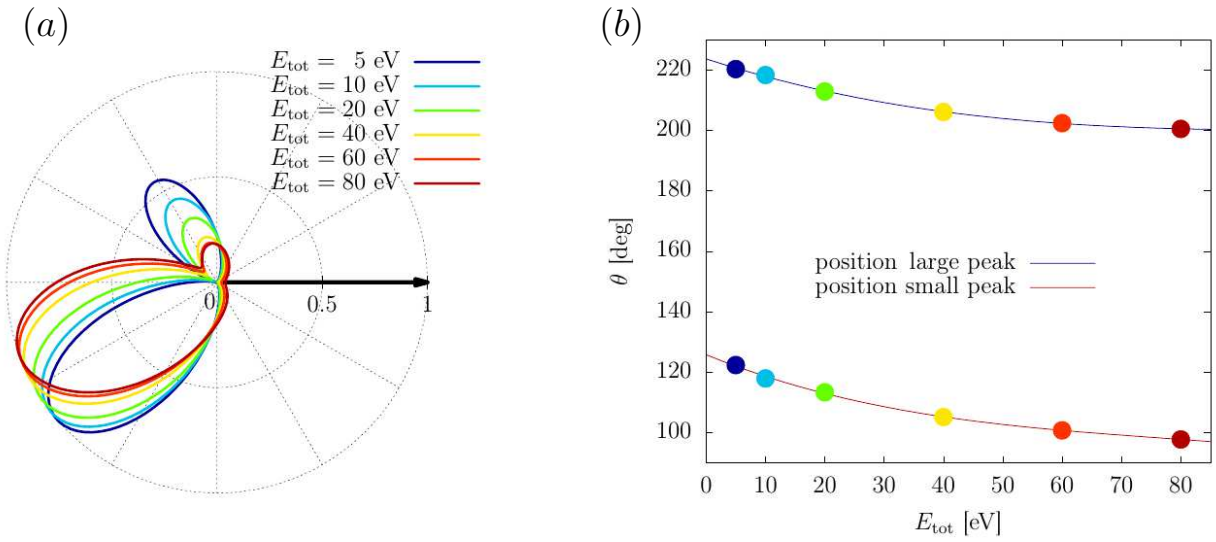

Figure 4.7.: (a) Angular distribution ($\theta_1 = \theta_2 = 90°, \varphi_1 = 0$) within the $\hat{x}$-$\hat{y}$ plane for a RCP pulse, a FWHM pulse duration of 2 fs and varying photon energies. The distributions are normalized to their maximal value. The relative energy sharing is held constant at $\Delta E/E_{\text{tot}} = 0.9$. The direction of the first electron is marked by the black arrow ($\theta_1 = \pi/2$ and $\varphi_1 = 0$). (b) Angle of maximal emission probability for the two lobes visible in (a).

5. Few-photon double ionization

Decreasing the carrier frequency ω of the laser pulse below 79 eV, the number of photons (n_{ph}) which have to be absorbed in order to overcome the double ionization threshold increases

$$\mathrm{n}_{ph}\omega > I_1 + I_2, \tag{5.1}$$

where $I_1 \approx 24.6$ eV is the first ionization potential and $I_2 \approx 54.4$ eV the second ionization potential of helium [Fig. 5.1(a)]. Different from the case of OPDI two separate ionization regimes exist, the sequential and the non-sequential regime [29]. While in the sequential regime the emission of the first electron can happen independently of the subsequent emission of the second electron, in the non-sequential regime the electrons are emitted near simultaneously and share the energy of the absorbed photons.
In the straightforward case of two-photon double ionization (TPDI) the sequential regime starts from $\omega > I_2$. In this case one electron absorbs a photon and is ionized ($E_1 = \omega - I_1$). After an arbitrary long time, the second electron absorbs a photon and is ionized ($E_2 = \omega - I_2$). For photon energies below the second ionization potential but still high enough that Eq. (5.1) holds (39.5 eV $< \omega <$ 54.5 eV), both photons have to be absorbed almost simultaneously resulting into non-sequential TPDI. For non-sequential TPDI the final energies of the electrons are not given by isolated peaks at $E_1 = \omega - I_1$ and $E_2 = \omega - I_2$, because the two electrons interact with each other via Coulomb correlation and exchange energy giving rise to the characteristic energy distribution [42] [Fig. 5.1(b)]. Thus, non-sequential TPDI is an ideal test case to study the influence of electron-electron correlation on photoionization[1].
Within this chapter we extend previous investigations and show results for non-sequential DI for four different wavelengths and different laser field polarizations (the numerical parameters are given in App. B.3) corresponding to a different minimum n_{ph} to reach the DI threshold (see Fig. 5.1).

[1] The imprint of electronic correlation on the emission pattern can also be seen in the spectrally sequential regime for ultrashort pulses [11, 37, 43]

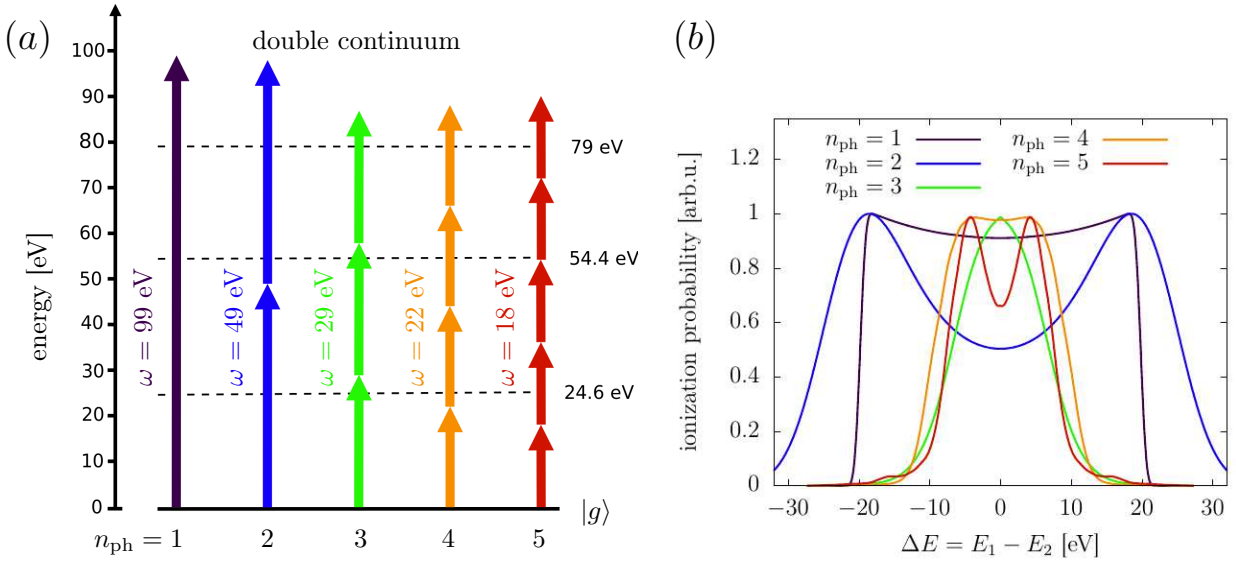

Figure 5.1.: (a) Schematic representation of the double ionization process from $n_{\mathrm{ph}} = 1$ up to $n_{\mathrm{ph}} = 5$. Each arrow represents one absorbed photon. (b) The photoelectron spectra $P(\Delta E)$ [Eq. (3.19)] corresponding to the DI processes from (a), integrated over the total energy $E_{\mathrm{tot}} = E_1 + E_2$.

5.1. Total double ionization probabilities

The extraction of the angle- and energy-integrated DI probability P^{DI} in the numerical implementation described in Sec. 3.2 is only accurate for asymptotic distances between the electrons implying that within the employed method P^{DI} is a projection time τ_{p} dependent quantity and converges only for $\tau_{\mathrm{p}} \to \infty$, see Fig. 5.2$(a)$. To circumvent this problem we fit a second-order polynomial to P^{DI} as function of $1/\tau_{\mathrm{p}}$ [Fig. 5.2(b)] and extrapolate the value to $1/\tau_{\mathrm{p}} = 0$ [35]. This procedure simulates the asymptotic projection after the end of the pulse.

In the following we compare P^{DI} for linear and circular polarization for different wavelengths [Fig. 5.1(a)] and total durations corresponding to 10 optical cycles (o.c.) for each wavelength. The wavelengths were chosen at the maximal cross sections obtained in [12]. The total double ionization probability for different photon energies corresponding to up to five photon-absorptions necessary for double ionization to occur together with the generalized n_{ph}-photon cross sections [Eq. (3.21)] can be seen in Tab. 5.1 for linear polarization and in Tab. 5.2 for circular polarization. Due to the different selection rules for linearly polarized ($\Delta L = \pm 1$, $\Delta M = 0$) and RCP ($\Delta L = \pm 1$, $\Delta M = 1$) fields, different angular momentum channels are occupied for the two different laser polarizations. For linearly polarized light multiple values of L are possible while for circular polarized light only one channel contributes.

For both polarizations the DI probability decreases with the number of photons needed to reach the DI threshold with the exception of $n_{\mathrm{ph}} = 5$ for linear polarization. The enhanced DI probability for $n_{\mathrm{ph}} = 5$ might be due to nearly resonant bound transitions at this wavelength. The ionization probability for circular polarization is slightly higher compared to linear polarization summed over all channels for $n_{\mathrm{ph}} = 2, 3, 4$ but orders of magnitude smaller for $n_{\mathrm{ph}} = 5$.

Comparing our results to reference values taken from Pindzola et al. [12] obtained for the same parameters and the conceptually identical method we find rather big differences. For linear

polarization most noteworthy is the discrepancy for the $L = 1$ channels for 3 and 5 photons where there is a factor of ten difference between our data and [12], see Tab. 5.1. The agreement for circular polarization is considerably better, probably due to the fact that the for some reason more problematic $L = 1$ channel cannot be populated for $n_{\mathrm{ph}} > 1$ because of the dipole selection rules for circular polarized light. A possible source for this difference might be the influence of the after pulse propagation time dependence of the DI yield. Nevertheless we have no obvious explanation for the disagreement of our data with the results of [12].

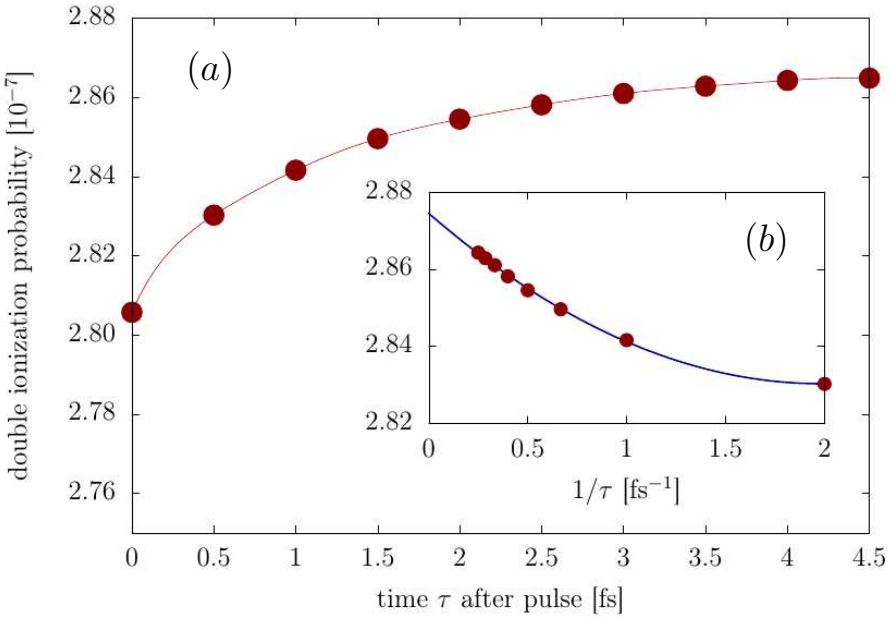

Figure 5.2.: (a) Total double ionization probability P^{DI} [Eq. (3.20)] for different projection times τ_{p} after the end of the pulse. For a linear polarized laser pulse with a wavelength of $\lambda = 42.7$ nm (29 eV), a Gaussian envelope with a FWHM duration of $T = 356$ as and an intensity of $I = 10^{14}$ W/cm^2. (b) The inset shows the same data points over the inverse projection time together with the quadratic fit (blue line) used to extrapolate the double ionization probability for asymptotic times after the pulse.

Table 5.1.: Total double ionization probabilities for linear polarization. Pulse parameters are given in App. B.3

Photons	Energy	L	Probability	Reference [12]	cross section
1	99 eV	1	8.34×10^{-5}		1.78×10^{-21} cm^2
2	49 eV	0	1.31×10^{-6}	1.5×10^{-6}	5.43×10^{-54} cm^4 s
		2	3.07×10^{-6}	3.5×10^{-6}	1.27×10^{-53} cm^4 s
		0+2	4.37×10^{-6}	5.0×10^{-6}	1.81×10^{-53} cm^4 s
3	29 eV	1	1.05×10^{-7}	1.0×10^{-6}	7.13×10^{-88} cm^6 s^2
		3	1.81×10^{-7}	2.7×10^{-7}	1.23×10^{-87} cm^6 s^2
		1+3	2.87×10^{-7}	1.3×10^{-6}	1.95×10^{-87} cm^6 s^2
4	22 eV	0	1.12×10^{-9}	2.5×10^{-9}	1.37×10^{-121} cm^8 s^3
		2	1.63×10^{-9}	5.7×10^{-9}	1.99×10^{-121} cm^8 s^3
		4	1.02×10^{-9}	2.8×10^{-9}	1.25×10^{-121} cm^8 s^3
		0+2+4	3.77×10^{-9}	1.1×10^{-8}	4.61×10^{-121} cm^8 s^3
5	18 eV	1	2.41×10^{-7}	2.6×10^{-6}	1.06×10^{-150} cm^{10} s^4
		3	7.94×10^{-11}	2.0×10^{-10}	3.49×10^{-154} cm^{10} s^4
		5	1.80×10^{-11}	4.8×10^{-11}	7.92×10^{-155} cm^{10} s^4
		1+3+5	2.41×10^{-7}	2.6×10^{-6}	1.06×10^{-150} cm^{10} s^4

Table 5.2.: Total double ionization probabilities for circular polarization. Pulse parameters are given in App. B.3

Photons	Energy	L	Probability	Reference [12]	cross section
1	99 eV	1	8.33×10^{-5}		1.78×10^{-21} cm^2
2	49 eV	2	4.61×10^{-6}	5.3×10^{-6}	1.91×10^{-53} cm^4 s
3	29 eV	3	4.53×10^{-7}	6.9×10^{-7}	3.07×10^{-87} cm^6 s^2
4	22 eV	4	4.56×10^{-9}	1.3×10^{-8}	5.57×10^{-121} cm^8 s^3
5	18 eV	5	1.41×10^{-10}	4.1×10^{-10}	6.20×10^{-154} cm^{10} s^4

5.2. Angular distributions

To study the imprint of Coulomb correlation on the double ionization process we focus on angular distributions as they allow a detailed understanding of DI. Due to parity conservation the electron emission pattern is fundamentally different for n_{ph} = odd or even. Thus we investigate the two cases separately.

5.2.1. Even number of photons

This section focuses on double ionization events involving $n_{\mathrm{ph}} = 2$ and $n_{\mathrm{ph}} = 4$ photons with linear and circular polarization and the resulting differences compared to Chap. 4 where only one photon is absorbed.
The angular distributions for $n_{\mathrm{ph}} = 2$ and linearly polarized pulses clearly reveal that differently from OPDI back-to-back emission is no longer forbidden for equal-energy sharing, but the most probable case [Fig. 5.3(a)] Furthermore, there are only marginal differences between the equal and the asymmetric energy sharing case. The qualitative shape of the angular distribution for $n_{\mathrm{ph}} = 2$ [Fig. 5.3(a)] to $n_{\mathrm{ph}} = 4$ [Fig. 5.3(b)] is similar for both wavelengths. Interestingly, however, for $n_{\mathrm{ph}} = 4$ additional side lobes appear around $\theta_2 = 120°$ and $\theta_2 = 240°$. The sidelobes are more prominently visible for asymmetric energy sharing, where also the emission for $\theta_1 - \theta_2 = \pi/2$ is no longer suppressed.

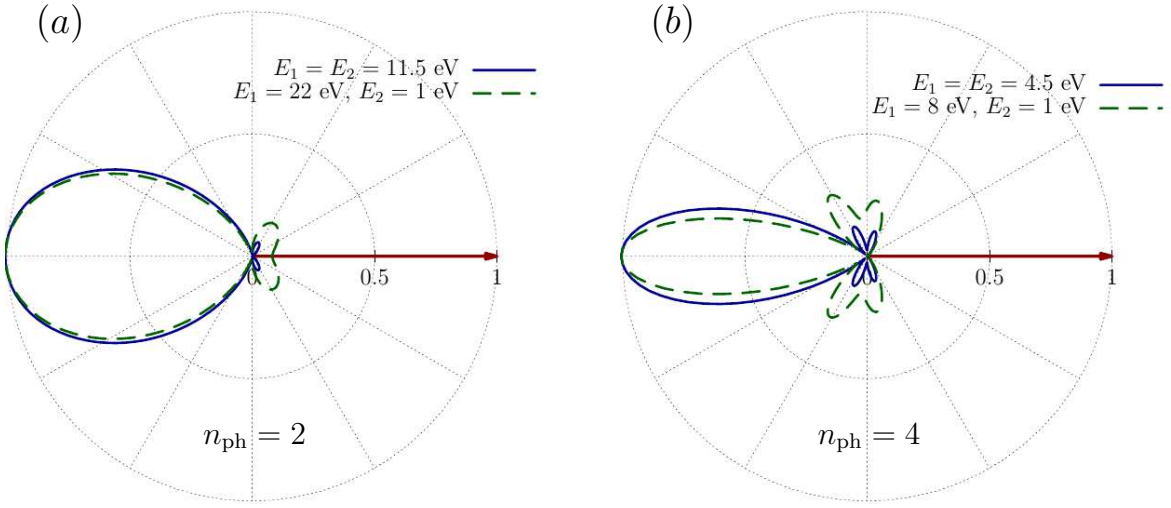

Figure 5.3.: Angular distributions ($\theta_1 = 0, \varphi_1 = \varphi_2 = 0$) in the $\hat{x}$-$\hat{z}$ plane for a linear polarized laser pulse. (a) For a wave length of $\lambda = 25.3$ nm and FWHM duration of $T = 210$ as. This corresponds to a photon energy of 49 eV and a minimum number of $n_{\mathrm{ph}} = 2$ photon absorptions. (b) For a wave length of $\lambda = 56.4$ nm and FWHM duration of $T = 470$ as. This corresponds to a photon energy of 22 eV and a minimum number of $n_{\mathrm{ph}} = 4$ to overcome the DI threshold. Direction of the first electron is marked by the red arrow, parallel to the laser polarization with $\theta_1 = 0$ and $\varphi_1 = 0$.

The angular distribution for TPDI by circularly polarized pulses and equal-energy sharing clearly reveals the influence of electronic correlation. Contrary to ionization by linearly polarized pulses there are no nodal lines imprinted onto the angular distribution [Fig. 5.4(a)]. The

probability that both electrons are ejected in opposite hemispheres (back-to-back) is by far dominant over the probability that both electrons are emitted side-by-side. Electron emission into the same direction ($\varphi_1 = \varphi_2$) is suppressed due to the repulsive electron-electron interaction. For unequal-energy sharing ($E_1 = 22$ eV and $E_2 = 1$ eV) the angular distribution changes slightly as the distribution appears to be rotated a few degree clockwise for RCP and counter-clockwise for LCP [Fig. 5.4(b)]. Thus, similar to the results shown in Sec. 4.2.2, we find signatures of circular dichroism.
For four-photon DI by circular polarized pulses and equal-energy sharing an additional dip appears at $\varphi_2 = 105°$ and $\varphi_2 = 255°$ in the otherwise qualitatively similar shaped angular distribution. Interestingly, the maximum of the angular distribution is not at $\varphi_2 = 180°$, but rather at $\varphi_2 = 152°$ and $\varphi_2 = 208°$. For completely asymmetric energy sharing the angular distribution is rotated into the same direction as for $n_{\mathrm{ph}} = 2$ but the angle of most probable emission is much farther away from $\varphi_1 - \varphi_2 = \pi$ compared to TPDI.

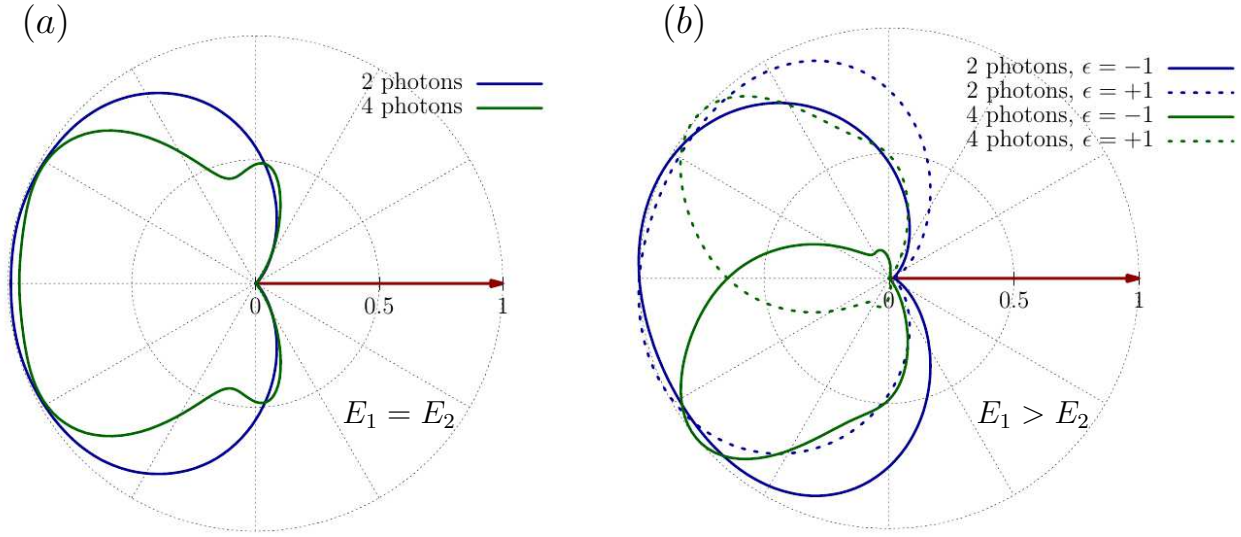

Figure 5.4.: Angular distributions ($\theta_1 = 0, \varphi_1 = \varphi_2 = 0$) within the polarization plane for a circular polarized laser pulse with a wave length of $\lambda = 25.3$ nm and FWHM duration of $T = 210$ as corresponding to $n_{\mathrm{ph}} = 2$ absorbed photons (blue line) and a wave length of $\lambda = 56.4$ nm and FWHM duration of $T = 470$ as corresponding to $n_{\mathrm{ph}} = 4$ absorbed photons (green line). The direction of the first electron is marked by the red arrow, parallel to the laser polarization, corresponding to $\theta_1 = 0$ and $\varphi_1 = 0$. (a) Equal-energy sharing. (b) $E_1 = 22$ eV and $E_2 = 1$ eV for $n_{\mathrm{ph}} = 2$ and $E_1 = 8$ eV and $E_2 = 1$ eV for $n_{\mathrm{ph}} = 4$.

The JAD (Fig. 5.5) provides a more comprehensive view on the influence of electronic correlation on double ionization. Whereas for OPDI the peaks were mainly distributed along the symmetric emission diagonal [$\theta_1 + \theta_2 = 2\pi$, Fig. 4.3($a, c$)], we find only minor peaks along this diagonal. For linearly polarized pulses for TPDI and four photon DI the maximal DI probability occurs for $\theta_1 = 0°$ with $\theta_2 = 180°$ and vice versa, corresponding to back-to-back emission [Fig. 5.5, left column]. Emission along the main diagonal ($\theta_1 = \theta_2$), representing side-by-side emission, is suppressed due to electron-electron interaction. For asymmetric energy sharing this suppression is less pronounced since the effect of electron-electron interaction is smaller in this case [Fig. 5.5, right column].

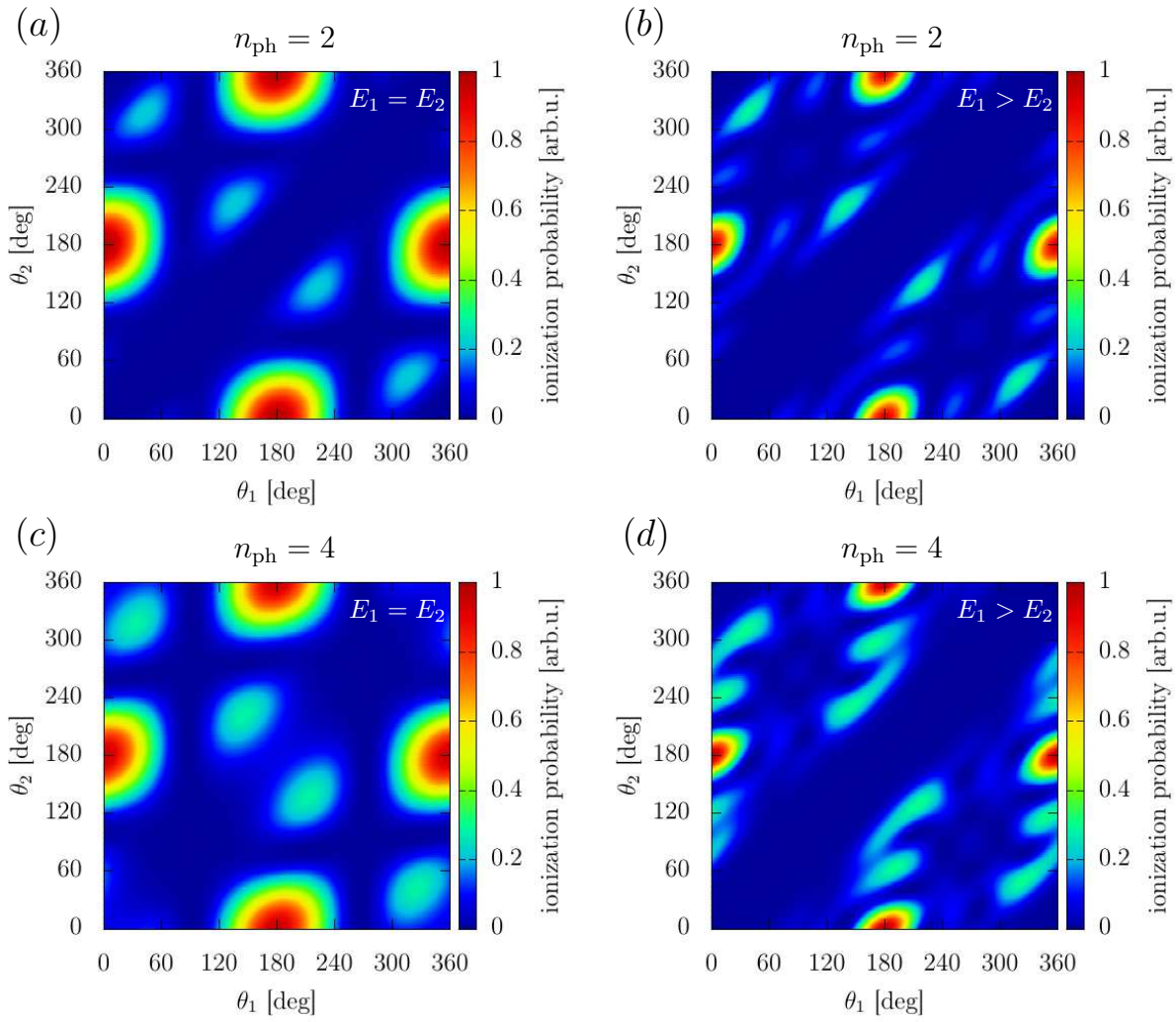

Figure 5.5.: JAD for a linear polarized laser pulse with a wave length of $\lambda = 25.3$ nm and FWHM duration of $T = 210$ as, corresponding to $n_{\mathrm{ph}} = 2$ (left column) and a wave length of $\lambda = 56.4$ nm and FWHM duration of $T = 470$ as, corresponding to $n_{\mathrm{ph}} = 4$ (right column). Equal-energy sharing case: (a) $E_1 = E_2 = 11.5$ eV and (c) $E_1 = E_2 = 4.5$ eV. Unequal-energy sharing case: (b) $E_1 = 22$ eV and $E_2 = 1$ eV and (d) $E_1 = 8$ eV and $E_2 = 1$ eV.

Circular dichroism

Circular and elliptic dichroism in DI ($n_{\mathrm{ph}} > 1$) of helium has been studied in the past using perturbative arguments [21]. Full *ab-initio* calculations on this topic, however, have not been presented yet. As shown in Fig. 5.4(b) for unequal-energy sharing a weak CD signal can be observed. Calculating the CD for the full JAD we find only weak CD for $n_{\mathrm{ph}} = 2$ [Fig. 5.6(a)]. For four-photon DI a stronger CD is present which is in magnitude similar to the case of OPDI [Fig. 5.6(b)].

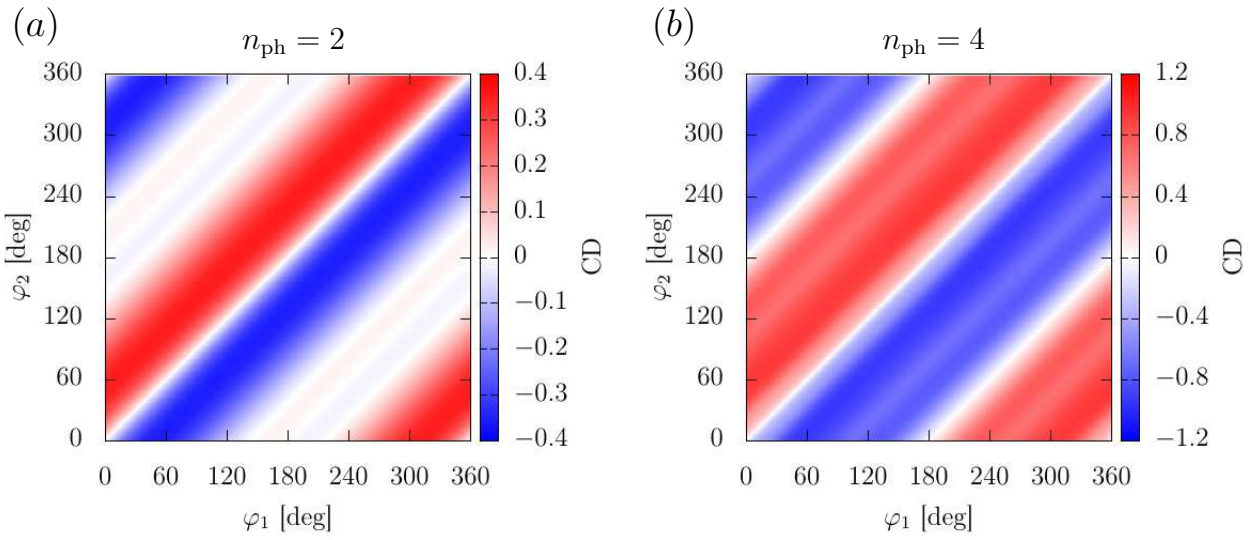

Figure 5.6.: Circular dichroism for an asymmetric energy sharing between the electrons. (a) $E_1 = 22$ eV and $E_2 = 1$ eV for $n_{\mathrm{ph}} = 2$. (b) $E_1 = 8$ eV and $E_2 = 1$ eV for $n_{\mathrm{ph}} = 4$.

5.2.2. Odd number of photons

For DI events involving $n_{\mathrm{ph}} = 3$ and $n_{\mathrm{ph}} = 5$ photons with linear and circular polarization the angular distributions look drastically different compared to DI with an even number of photons. For $n_{\mathrm{ph}} = 3$ ($\omega = 29$ eV), unlike the previous cases, sequential double ionization is energetically possible where the first electron absorbs one photon and subsequently the second one absorbs two. Nevertheless, due to the short pulse duration the sequential contribution should be small compared to the non-sequential contribution to DI. Due to the broad bandwidth for $n_{\mathrm{ph}} = 5$ (≈ 3 eV for $\omega = 18$ eV) sequential DI is possible with a split into two and three photons. The angular distributions for ionization by linearly polarized fields (Fig. 5.7) show only a relatively small difference compared to OPDI (grey inset) for equal energy sharing. The main lobes continuously shift closer to a relative angle of 180° and a pair of side lobes appear for $n_{\mathrm{ph}} = 3$ [Fig. 5.7(a)] as well as for $n_{\mathrm{ph}} = 5$ [Fig. 5.7(b)]. These side lobes are also persistent for unequal energy sharing. In this case, contrary to OPDI orthogonal emission of the two electrons is strongly suppressed. Noteworthy is, however, that for $n_{\mathrm{ph}} = 5$ the maximum does not appear at $\theta_2 = 180°$ but rather at $\theta_2 = 154°$ and $\theta_2 = 206°$ [Fig. 5.7(b), green dashed line].
For ionization by LCP and RCP pulses the angular distributions for equal energy sharing are maximal for approximately orthogonal emission of both electrons [Fig. 5.8(a)]. This shows that

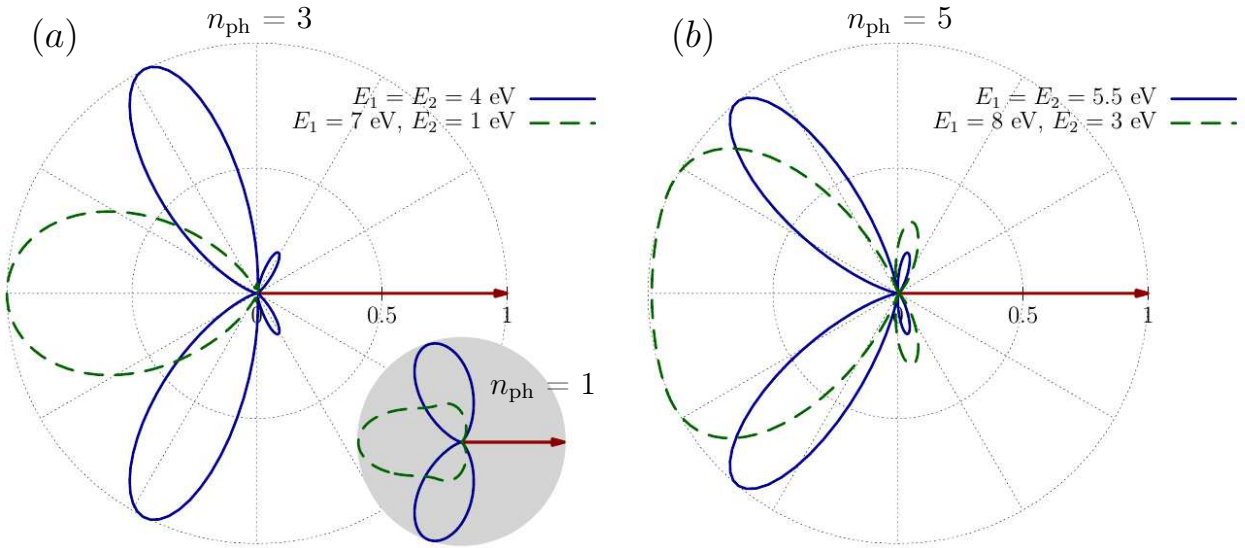

Figure 5.7.: Angular distributions ($\theta_1 = 0, \varphi_1 = \varphi_2 = 0$) in the $\hat{x}$-$\hat{z}$ plane for a linear polarized laser pulse. (a) For a wave length of $\lambda = 42.7$ nm and FWHM duration of $T = 365.5$ as. This corresponds to a photon energy of 29 eV and a minimum number of $n_{\mathrm{ph}} = 3$ to overcome the DI threshold. The grey inset shows the angular distribution for one-photon absorption from Fig. 4.3(b, d) for comparison, with $E_1 = E_2 = 10$ eV (blue line) and $E_1 = 19$ eV, $E_2 = 1$ eV (green dashed line). (b) For a wave length of $\lambda = 68.9$ nm and FWHM duration of $T = 574$ as. This corresponds to a photon energy of 18 eV and a minimum number of $n_{\mathrm{ph}} = 5$ to overcome the DI threshold. The direction of the first electron is marked by the red arrow ($\theta_1 = 0$ and $\varphi_1 = 0$).

the nodal plane for $\theta_1 = \pi/2, 3\pi/2$ in Fig. 5.7 is an imprint of the polarization of the ionizing pulse. The lobes are slightly shifted towards $\varphi_2 = 90°$ and $\varphi_2 = 270°$ compared to the angular distribution of OPDI [Fig. 4.4(a)]. We hypothesise that this is an effect of the balance between the electron-electron repulsion and the parity-forbidden back-to-back emission. For asymmetric energy sharing the angular distribution shows, similar to the case of OPDI, that one emission angle is strongly preferred over the other [Fig. 4.4(b)]. Interestingly, for $n_{\mathrm{ph}} = 3$ and $\epsilon = -1$ the emission angle $\varphi_2 < 180°$ is preferred while for $n_{\mathrm{ph}} = 1$ and $n_{\mathrm{ph}} = 5$ the opposite emission angle is preferred.

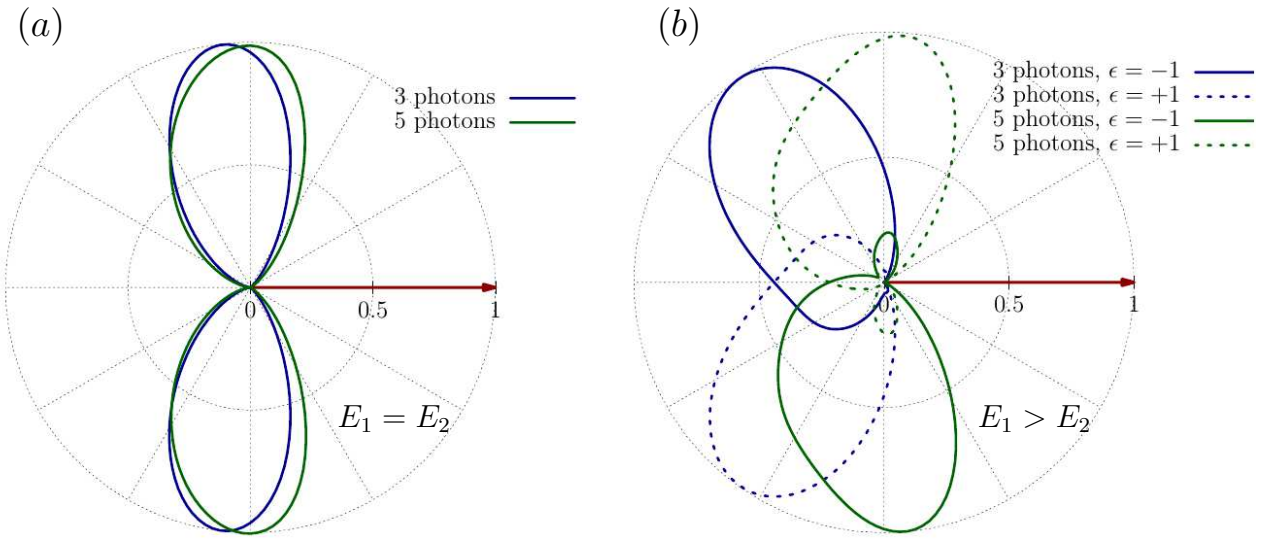

Figure 5.8.: Angular distributions ($\theta_1 = \theta_2 = 90°, \varphi_1 = 0$) within the polarization plane for a circular polarized laser pulse with a wave length of $\lambda = 42.7$ nm and FWHM duration of $T = 365.5$ as corresponding to $n_{\mathrm{ph}} = 3$ (blue line) and a wave length of $\lambda = 68.9$ nm and FWHM duration of $T = 574$ as corresponding to $n_{\mathrm{ph}} = 5$ (green line). The direction of the first electron is marked by the red arrow, parallel to the laser polarization ($\theta_1 = 90°$ and $\varphi_1 = 0$). (a) Equal-energy sharing. (b) $E_1 = 7$ eV and $E_2 = 1$ eV for $n_{\mathrm{ph}} = 3$ and $E_1 = 8$ eV and $E_2 = 3$ eV for $n_{\mathrm{ph}} = 5$.

From the JAD for linearly polarized pulses (Fig. 5.9) stronger differences compared to $n_{\mathrm{ph}} = 1$ become apparent. While for equal energy sharing (left column) the overall shape is similar to OPDI [Fig. 4.3(a)] with nodes along the conic and back-to-back emission lines, a more intricate pattern emerges for higher n_{ph}. The most probable cases of emission are no longer for symmetric emission ($\theta_1 + \theta_2 = 360°$) but for $\theta_1 = 0°$ with $\theta_2 = 120°$ and $\theta_2 = 240°$, or $\theta_1 = 60°$ with $\theta_2 = 180°$. For asymmetric energy sharing (right column) the JAD for 3- and 5-photon double ionization surprisingly resembles the results for $n_{\mathrm{ph}} = 2, 4$ more closely than for OPDI. The reason for this is that due to the generally lower excess energies available to the ionized electrons, they feel their mutual presence for longer times and hence the effect of the repulsive electron-electron interaction is more pronounced. Thus the JAD reveals a strong preference for back-to-back emission along the laser polarization direction, i.e. $\theta_1 = 0°$ with $\theta_2 = 180°$ and vice versa.

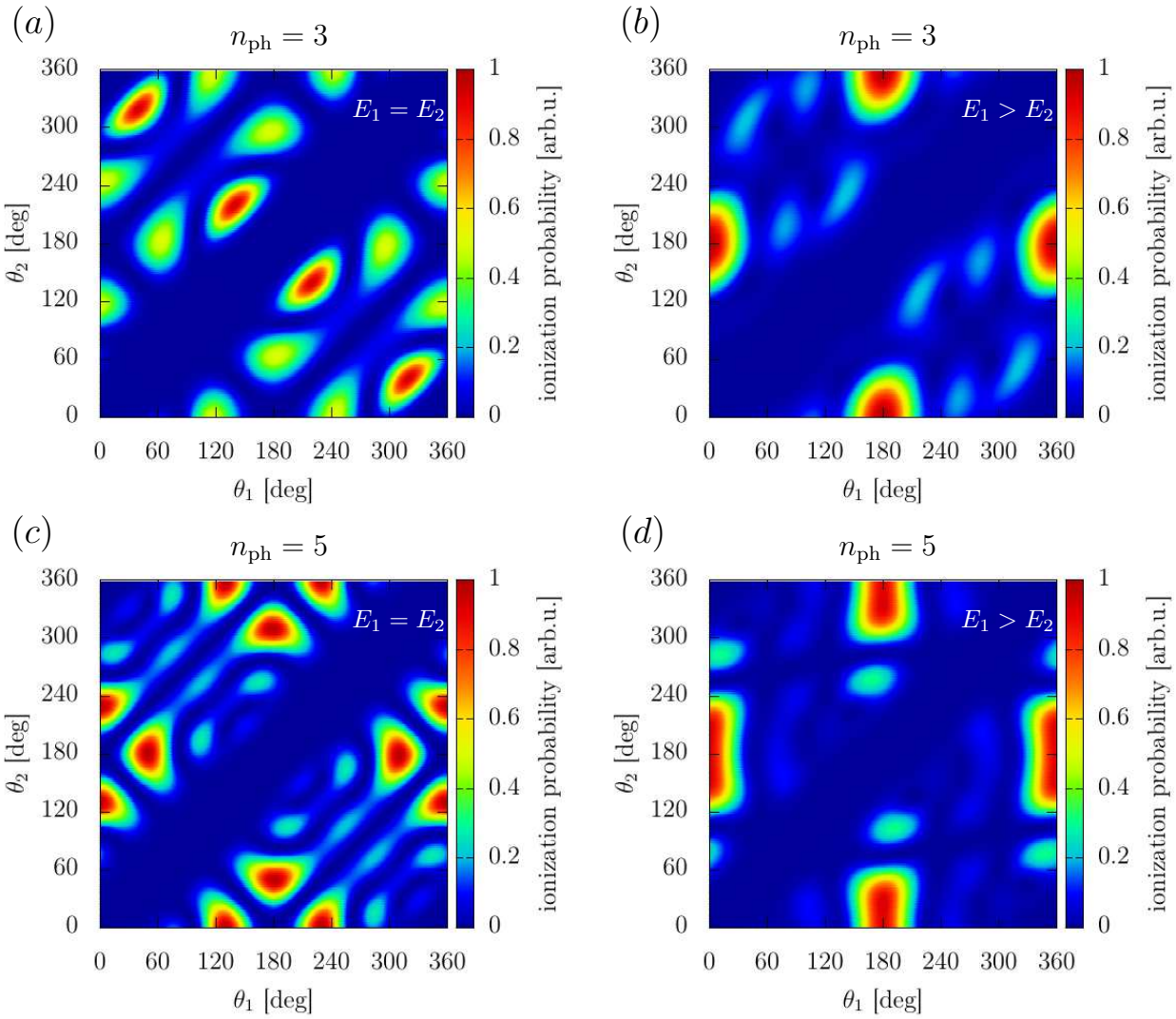

Figure 5.9.: JAD for a linear polarized laser pulse with a wave length of $\lambda = 42.7$ nm and FWHM duration of $T = 365.5$ as, corresponding to $n_{\mathrm{ph}} = 3$ photon absorptions (left column) and a wave length of $\lambda = 68.9$ nm and FWHM duration of $T = 574$ as, corresponding to $n_{\mathrm{ph}} = 5$ photon absorptions (right column). Equal-energy sharing case: (a) $E_1 = E_2 = 4$ eV and (c) $E_1 = E_2 = 5.5$ eV. Unequal-energy sharing case: (b) $E_1 = 7$ eV and $E_2 = 1$ eV and (d) $E_1 = 8$ eV and $E_2 = 3$ eV.

Circular dichroism

For asymmetric energy sharing, similar to $n_{\mathrm{ph}} = 1$ and $n_{\mathrm{ph}} = 4$, a strong circular dichroism emerges [Fig. 5.10]. Remarkable here is that for $n_{\mathrm{ph}} = 3$ the sign of the CD pattern is reversed compared to all previous cases. This becomes especially apparent in the angular distribution [Fig. 5.8(b)] where the peak of the main lobe is shifted to an angle below 180° for LCP ($\epsilon = -1$) and to an angle above 180° for RCP ($\epsilon = +1$). For all other cases ($n_{\mathrm{ph}} = 1, 2, 4, 5$) the direction of this shift is reversed. As of now we do not have a straightforward explanation for this behaviour.

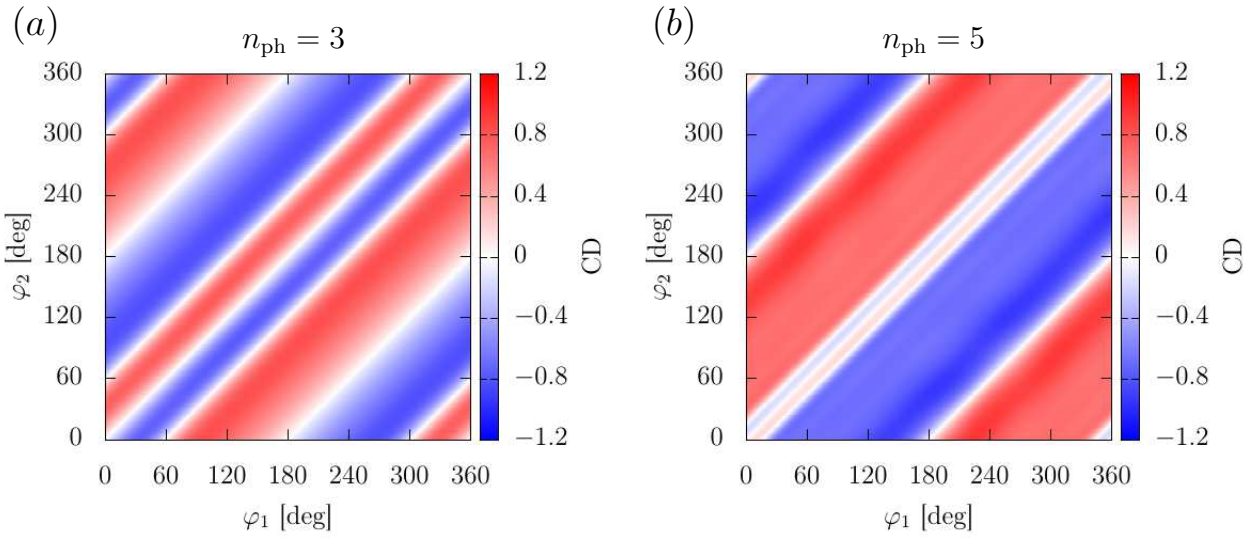

Figure 5.10.: Circular dichroism for an asymmetric energy distribution between the two electrons. (a) $E_1 = 7$ eV and $E_2 = 1$ eV for $n_{\mathrm{ph}} = 3$. (b) $E_1 = 8$ eV and $E_2 = 3$ eV for $n_{\mathrm{ph}} = 5$.

6. Approaching the long wavelength regime

To study the transition between the multi-photon and strong field DI regime we increase the wavelength of the ionizing field stepwise up to $\lambda = 396$ nm in the following chapter (numerical parameters are given in App. B.4). Due to the increasing numerical expenses with increasing wave length we will focus from now on linearly polarized pulses. We compare DI to single ionization (SI) probabilities for peak intensities spanning several orders of magnitude [23]. Further, we analyse the angular distributions and compare them to the results from previous chapters.

6.1. Double ionization for 98.5 nm

For a wave length of $\lambda = 98.5$ nm ($\omega \approx 12.6$ eV) at least 7 photons have to be absorbed for DI to occur. The resulting doubly differential photo electron spectrum is shown in Fig. 6.1(a). Besides the band at total energy $E_{\mathrm{tot}} = 7.3$ eV resulting from the absorption of 7 photons ($n_{\mathrm{ph}} = 7$) additional bands spaced by ω are visible at higher energies. These additional peaks are caused by above threshold ionization (ATI), where more photons are absorbed than necessary to overcome the DI threshold [44] and appear at

$$E_{\mathrm{tot}} = E_1 + E_2 = n_{\mathrm{ph}}\omega - I_1 - I_2 - 2U_{\mathrm{p}}, \tag{6.1}$$

where U_{p} is the ponderomotive potential

$$U_{\mathrm{p}} = \frac{I}{4\omega^2} \propto I\lambda^2. \tag{6.2}$$

Thus every band corresponds to an additional photon, marked by white or black dashed lines in Fig. 6.1. The singly differential cross section $P(E_{\mathrm{tot}})$ [Eq. (3.18)] clearly shows distinct ATI peaks [Fig. 6.1(b)]. The expected energies of the peaks according to Eq. (6.1) agree very well with our simulation results.

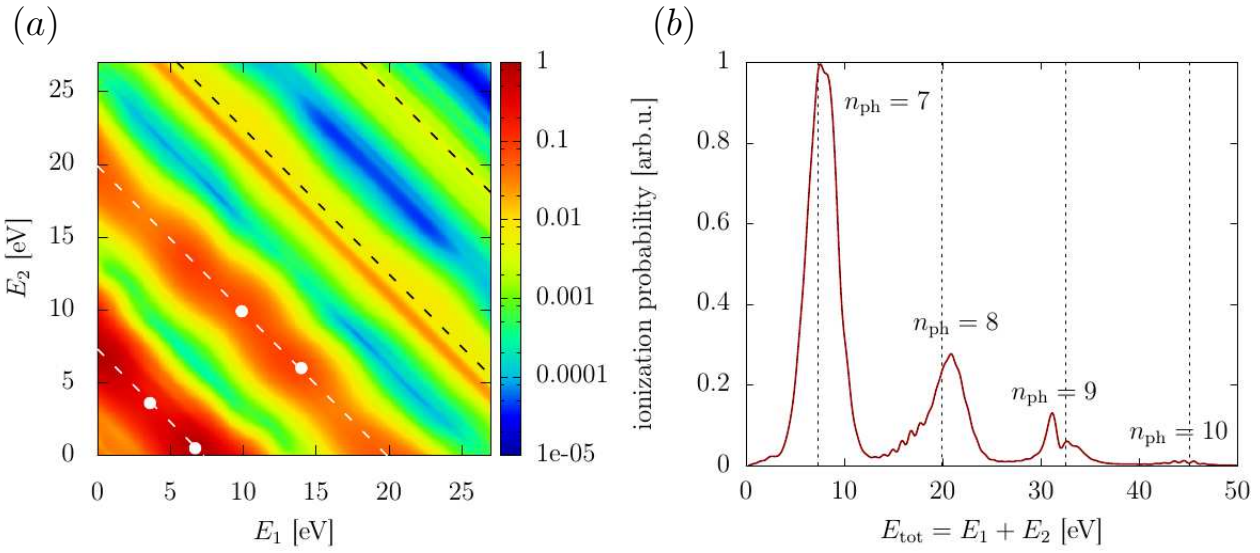

Figure 6.1.: (a) Photo electron spectrum for a laser pulse with a wave length $\lambda = 98.5$ nm, a FWHM duration $T = 1.7$ fs and a peak intensity $I = 10^{15}$ W/cm^2. White dots mark the energies for which we calculated angular distributions (Fig. 6.4). (b) Spectrum integrated over $\Delta E = E_1 - E_2$ [Eq. (3.18)]. Dashed lines indicate total energies according to Eq. (6.1).

Compared to previous chapters, sequential DI is energetically possible (e.g. a 2-5 split for $n_{\mathrm{ph}} = 7$). This makes the distinction between sequential and NS ionization more difficult, as both will take place. In the following we first focus on the differences between sequential and non-sequential DI (NSDI) and later show angular distributions for $n_{\mathrm{ph}} = 7$ and $n_{\mathrm{ph}} = 8$.

6.1.1. Ionization probabilities

For a wave length $\lambda = 98.5$ nm we can still obtain numerically converged DI probabilities for a wide range of pulse parameters. Historically, sequential and NSDI in the long-wavelength regime have been distinguished by analysing the SI and DI probability as function of the peak intensity of the ionizing laser field, see [13] and Fig. 6.2. In a pioneering experiment Walker et al. measured the number of He^+ (corresponding to SI) and of He^{2+} (corresponding to DI) ions for ionization of helium by a linear polarized laser pulse with a wave length of $\lambda = 780$ nm. Comparing the experimental results to the ionization probabilities obtained using the single active electron (SAE) approximation, they were able to clearly identify imprints of NS processes.
At the onset of DI the He^{2+} count rate is significantly enhanced compared to the prediction by the SAE approximation. This enhancement, in the literature often referred to as "knee", can be explained by the "knockout" process, already introduced in Chap. 4. The first electron tunnels out of the core potential, is driven back to the core by the laser field and knocks out the second electron. The colliding electron has a maximal energy of $3.17U_p$. Over the intensity range of the "knee" $3.17U_p$ is larger than the second ionization potential of helium (54.4 eV). Thus, the returning electron has enough energy to knock out the second electron and DI can occur. The SAE approximation (solid lines in Fig. 6.2) which does not include electron-electron correlation can not describe this process and, thus, underestimates the DI rate. Measurements with circular polarized laser pulses [45] showed that DI is not enhanced compared to the SAE prediction as there are no recolliding electrons, further supporting the "knockout" model.

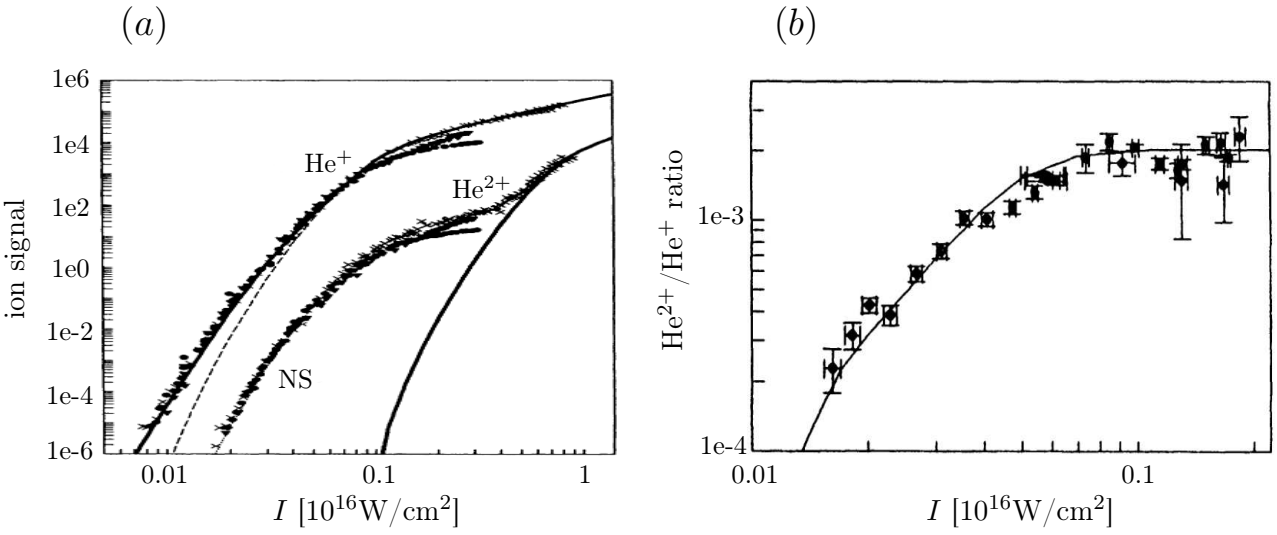

Figure 6.2.: He^+ and He^{2+} ion yields for a linear polarized laser pulse with total duration $T_{tot} = 100$ fs and a wave length $\lambda = 780$ nm, measured by Walker et. al in [13]. (a) He^+ and He^{2+} ion yields separately (black dots) together with SAE calculations (solid lines) and ac-tunneling calculations (dashed lines). (b) He^{2+}/He^+ ratio. Solid line is calculated from the ac-tunneling rate times a constant. Figure reproduced from [13].

Our results of DI yields for $\lambda = 98.5$ nm show no "knee" structure at all (Fig. 6.3). Rather, for intensities up to $I \approx 8 \times 10^{15}$ W/cm^2 the DI/SI ratio follows a nearly perfectly straight line

in a double logarithmic plot, corresponding to an intensity dependence of DI/SI $\propto I^{4.7}$. The reason for this is that the maximal energy of the returning electron ($3.17U_p$) is well below the second ionization potential (54.4 eV) within this intensity range. Thus, the returning electron has not enough kinetic energy to knock out the electron still bound by the ion. Fig. 6.3(b) shows that the slope of the DI to SI ratio significantly changes for $I > 2 \times 10^{15}$ W/cm^2 ($U_p > 2$ eV) to DI/SI $\propto I^{2.1}$, indicating a change in the DI process with its concrete nature not entirely clear yet. Further noticeable is the decrease of both SI and DI probability for intensities above $I = 8 \times 10^{15}$ W/cm^2. Unfortunately, converged results for even higher intensities beyond 10^{16} W/cm^2 could not be achieved due to the increased numerical complexity.

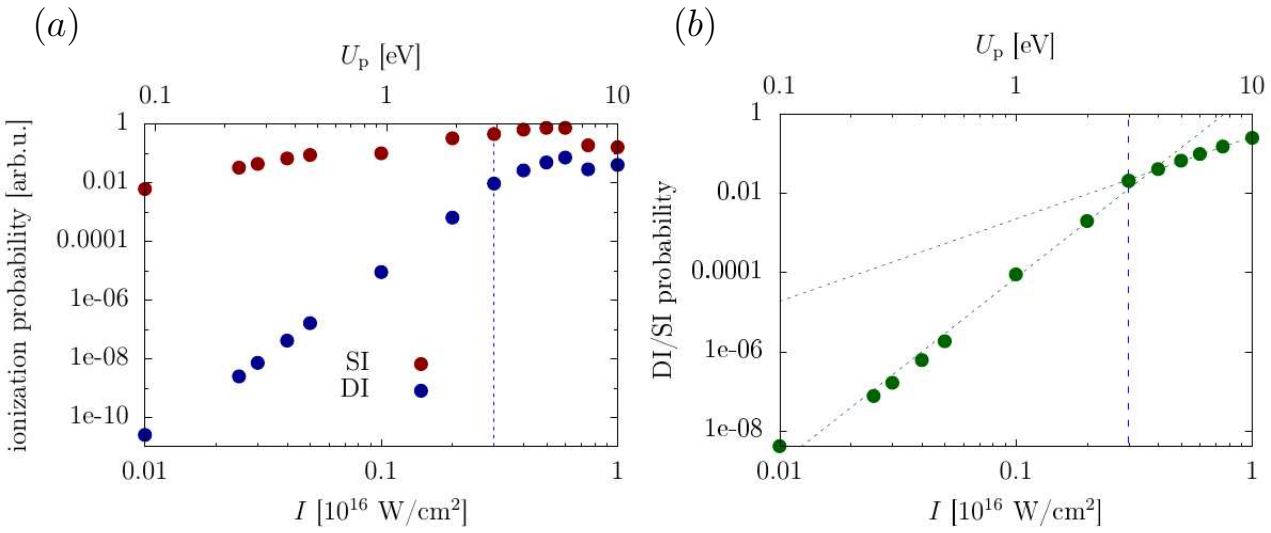

Figure 6.3.: Peak intensity dependence of ionization probabilities for a linear polarized laser pulse with a wave length of $\lambda = 98.5$ nm and a FWHM pulse duration of $T = 4$ fs. (a) SI and DI probability. (b) Ratio of DI to SI probability.

6.1.2. Angular distributions

Despite involving processes with significantly more photons, the angular distributions still show the same qualitative characteristics as the respective distributions involving one or two photons [Fig. 6.4]. For $n_{ph} = 7$ and equal-energy sharing the characteristic "butterfly" shape already encountered for $n_{ph} = 1$ emerges. The only difference is the appearance of additional side lobes at $\theta_2 = 57°$ and $\theta_2 = 303°$. For strongly asymmetric energy sharing back-to-back is still the most dominant emission pattern, which is also the case for $n_{ph} = 8$. The angular distribution for the first ATI band ($n_{ph} = 8$) and equal-energy sharing shows very little differences as compared to the angular distribution encountered for $n_{ph} = 2$. The same trend can be observed for asymmetric energy sharing where the angular distributions display only marginal differences between $n_{ph} = 7$ and $n_{ph} = 8$ and also compared to the angular distribution for $n_{ph} = 2$. This further solidifies the hypothesis discussed in Chap. 5 that the angular distributions are mainly dominated by the selection rules.

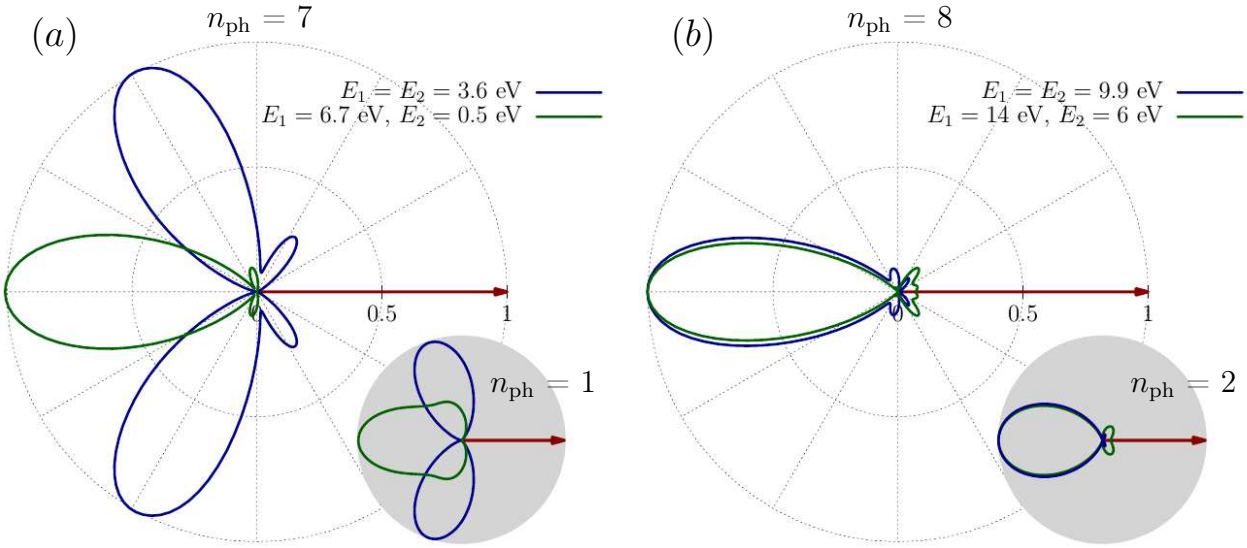

Figure 6.4.: Angular distributions ($\theta_1 = 0, \varphi_1 = \varphi_2 = 0$) in the $\hat{x}$-$\hat{z}$ plane for a linear polarized laser pulse. For a wave length of $\lambda = 98.5$ nm and FWHM duration of $T = 1.7$ fs. This corresponds to a photon energy of 12.6 eV. (a) Total energy corresponding to $n_{\mathrm{ph}} = 7$. The grey inset shows the angular distribution for $n_{\mathrm{ph}} = 1$ from Fig. 4.3(b, d) for comparison, with $E_1 = E_2 = 10$ eV (blue line) and $E_1 = 19$ eV, $E_2 = 1$ eV (green line). (b) Total energy corresponding to $n_{\mathrm{ph}} = 8$. The grey inset shows the angular distribution for $n_{\mathrm{ph}} = 2$ from Fig. 5.3 for comparison, with $E_1 = E_2 = 11.5$ eV (blue line) and $E_1 = 22$ eV, $E_2 = 1$ eV (green line). Direction of the first electron is marked by the red arrow, parallel to the laser polarization ($\theta = 0$ and $\varphi = 0$). The used energies are marked by white dots in the energy spectrum [Fig. 6.1(a)].

Comparing the JAD for $n_{\mathrm{ph}} = 7$ for long ($T_{\mathrm{tot}} = 10$ o.c. $= 3.3$ fs) and short ($T_{\mathrm{tot}} = 5$ o.c. $= 1.65$ fs) pulses gives additional insight into the DI process. For equal-energy sharing the long pulse duration [Fig. 6.5(a)] results in an emission pattern preferring symmetric emission, as the most probable emission angles are $\theta_1 \approx 30°$, $\theta_2 \approx 330°$ and $\theta_1 \approx 150°$, $\theta_2 \approx 210°$. It most strongly resembles the JAD for $n_{\mathrm{ph}} = 3$ [Fig. 5.9(a)].
Differently for short pulses the JAD resembles more the case of $n_{\mathrm{ph}} = 5$ [Fig. 5.9(c)]. This indicates that the emission pattern is mainly governed by the sequentiality of the process and not by n_{ph}. Sequential DI prefers emission patterns with maxima for symmetric emission, while NSDI prefers conic emission with $\theta_1 - \theta_2 = 120°$. For such a short pulse the electrons continuously interact with each other during the DI process, thus showing the effects of electron-electron correlation characteristically for NSDI.
For asymmetric energy sharing where one emitted electron is significantly faster than the other one there seems to be no such distinction for different total pulse durations as the JAD is basically indistinguishable for the two cases [Fig. 6.5(c), (d)]. The emitted electrons have very different energies and thus momenta, implicating that the characteristic interaction time between the electrons is for both pulse durations small compared to the pulse duration. We can, however, not exclude that even shorter pulse durations would reveal a pulse duration dependence of the JAD for asymmetric energy sharing.

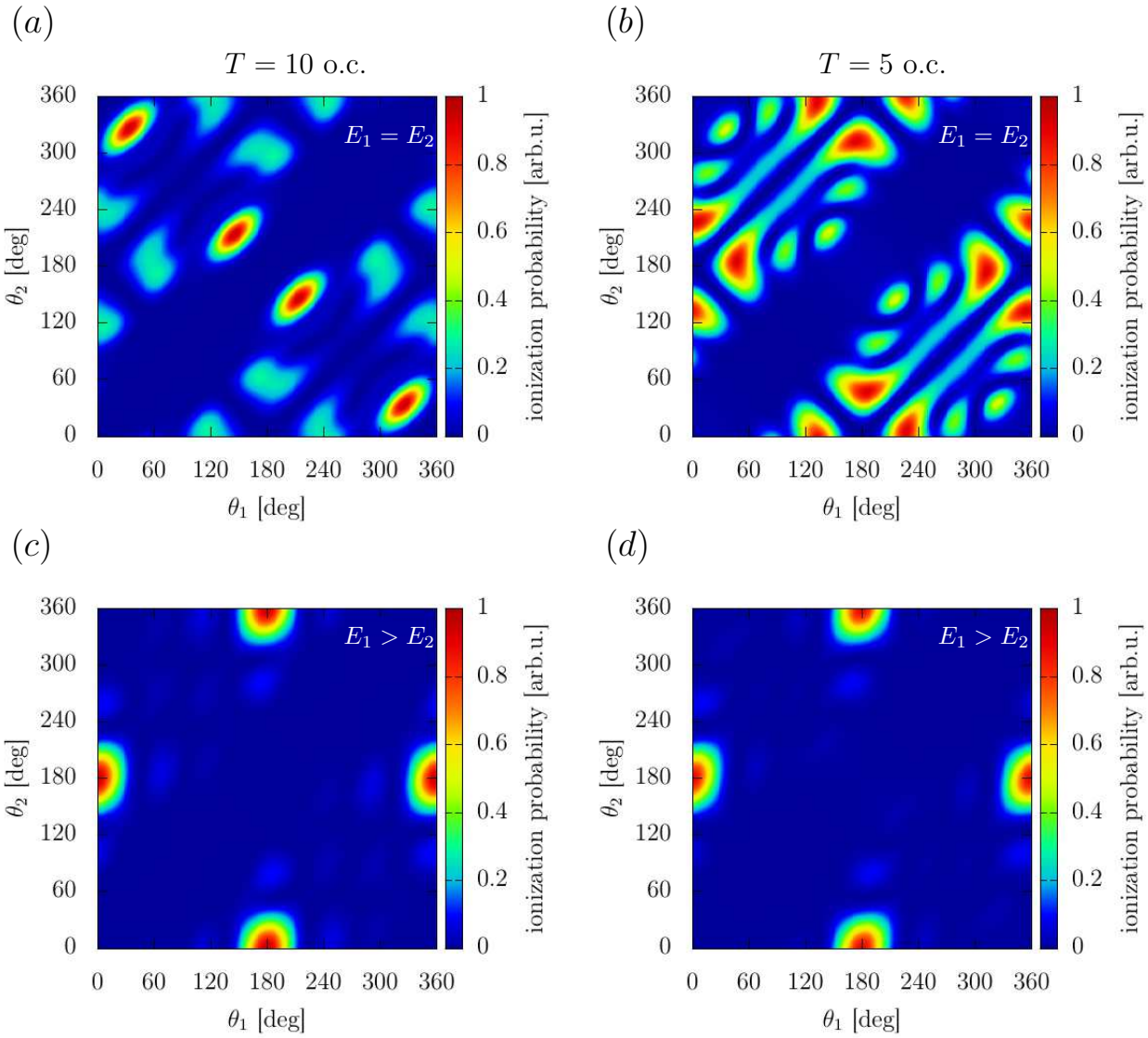

Figure 6.5.: JAD for a linearly polarized laser pulse with a wave length of $\lambda = 98.5$ nm and $n_{\mathrm{ph}} = 7$. Left column: Total pulse duration of 10 optical cycles ($T_{\mathrm{tot}} = 3.3$ fs). Right column: Total pulse duration of 5 optical cycles ($T_{\mathrm{tot}} = 1.65$ fs). Top row: Equal-energy sharing ($E_1 = E_2 = 3.6$ eV). Bottom row: Asymmetric energy sharing ($E_1 = 6.7$ eV, $E_2 = 0.5$ eV).

6.2. Double ionization for 197 nm and 394 nm

In this section we present preliminary results for DI with laser pulses with a wave length of $\lambda = 197$ nm and $\lambda = 394$ nm. The numerical parameters are given in App. B.5. Unfortunately solving the TDSE directly using the time-dependent close-coupling method scales very unfavourably with the wavelength [46]. The reason is that at long wavelengths the electron momenta are mostly determined by the vector potential $p_{\max} \propto A_0 \propto \lambda\sqrt{I}$. To correctly represent these momenta a high enough spatial grid point density is required. Further, longer cycle periods implicate longer pulse durations and thus longer propagation times. The increase in n_{ph} also makes a larger close-coupling expansion necessary. All this combined leads to results only qualitatively converged which we believe are nonetheless useful to make statements about the general properties of many-photon DI.

The previously seen characteristics for n_{ph} odd and n_{ph} even are still clearly visible even for $n_{\mathrm{ph}} > 13$ [Fig. 6.6]. For $n_{\mathrm{ph}} = 13$ there are only few differences compared to the angular distribution for $n_{\mathrm{ph}} = 1$. The main lobes for equal-energy sharing ($E_1 = E_2 = 1.4$ eV) are shifted towards $\theta_2 = 90°$ and $\theta_2 = 270°$. Noteworthy, however, is the appearance of a side-lobe at $\theta_2 = 0$, in the previous cases completely suppressed by the electron-electron repulsion. This can be explained by sequential DI with the respective ionization events well separated in time. This is possible due to the comparatively long total pulse duration of $T = 10$ o.c., corresponding to 6.6 fs. For $n_{\mathrm{ph}} = 14$ this peak at $\theta_2 = 0$ is even more noticeable where the angular distribution for equal-energy sharing ($E_1 = E_2 = 4.9$ eV) starts to approach the $\cos^2$ distribution of a Hertz dipole which would be expected for fully uncorrelated sequential DI. Side-by-side emission is only slightly less probable compared to back-to-back emission. Completely different, however, is that the orthogonal emission is not suppressed. For asymmetric energy sharing the results for the angular distribution for $n_{\mathrm{ph}} = 13$ closely resemble the case of OPDI with the only significant difference that orthogonal emission is strongly suppressed for $n_{\mathrm{ph}} = 13$. Contrary for $n_{\mathrm{ph}} = 14$ orthogonal emission is sizeable as compared to TPDI. In general, however, the angular distributions are similar to OPDI and TPDI, respectively.

For both $n_{\mathrm{ph}} = 13$ and $n_{\mathrm{ph}} = 14$ and equal-energy sharing the JAD [Fig. 6.7$(a),(b)$] strongly resembles the respective JAD for $n_{\mathrm{ph}} = 1$ and $n_{\mathrm{ph}} = 2$. The main differences are that for $n_{\mathrm{ph}} = 13$ side-by-side emission is, while still suppressed, possible for all angles $\theta_1 = \theta_2$. For $n_{\mathrm{ph}} = 14$ side-by-side emission is nearly as probable as back-to-back emission, but maximal for $\theta_1 = \theta_2 = 0, 180°$.

For $\lambda = 394$ nm with $n_{\mathrm{ph}} \geq 29$ the JAD shows a completely different picture [Fig. 6.7$(c),(d)$]. While the most probable angles are the same as for lower n_{ph}, many new maxima in the emission patterns appear. It is not entirely clear if these patterns are physically relevant or numerical artefacts due to the non complete numerical convergence (see Appendix C). As before, side-by-side emission is also not completely suppressed, due to the long pulse duration.

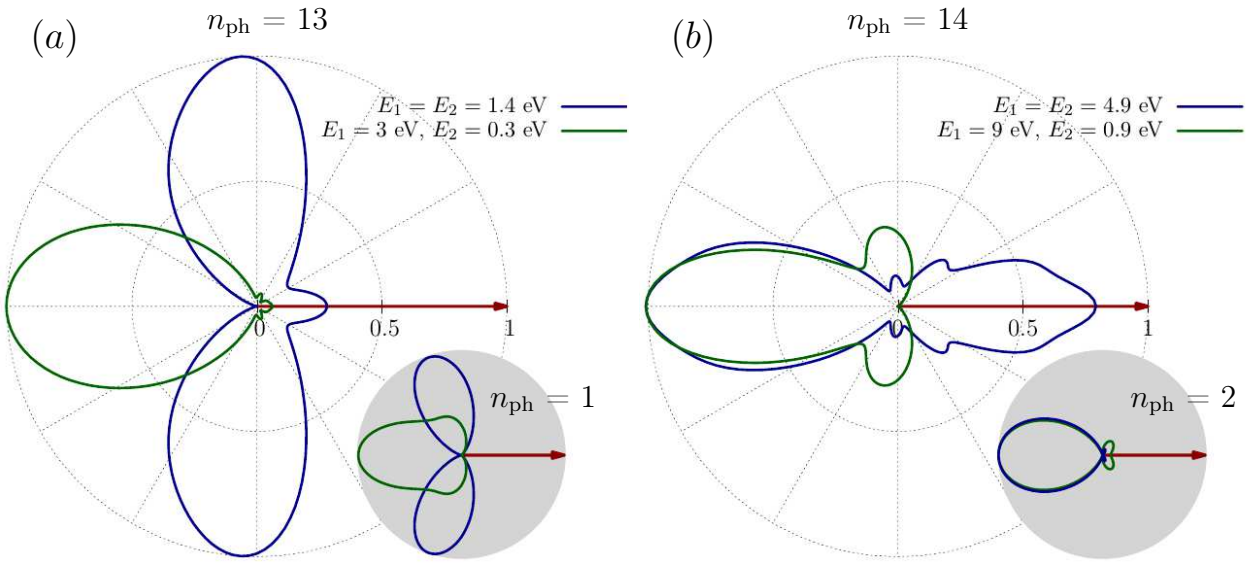

Figure 6.6.: Angular distributions ($\theta_1 = 0, \varphi_1 = \varphi_2 = 0$) in the $\hat{x}$-$\hat{z}$ plane for a linear polarized laser pulse. For a wave length of $\lambda = 197$ nm and FWHM duration of $T = 3.3$ fs. This corresponds to a photon energy of 6.3 eV. (a) Total energy corresponding to $n_{\mathrm{ph}} = 13$. The grey inset shows the angular distribution for $n_{\mathrm{ph}} = 1$ from Fig. 4.3(b, d) for comparison, with $E_1 = E_2 = 10$ eV (blue line) and $E_1 = 19$ eV, $E_2 = 1$ eV (green line). (b) Total energy corresponding to $n_{\mathrm{ph}} = 14$. The grey inset shows the angular distribution for $n_{\mathrm{ph}} = 2$ from Fig. 5.3 for comparison, with $E_1 = E_2 = 11.5$ eV (blue line) and $E_1 = 22$ eV, $E_2 = 1$ eV (green line). Direction of the first electron is marked by the red arrow, parallel to the laser polarization ($\theta = 0$ and $\varphi = 0$).

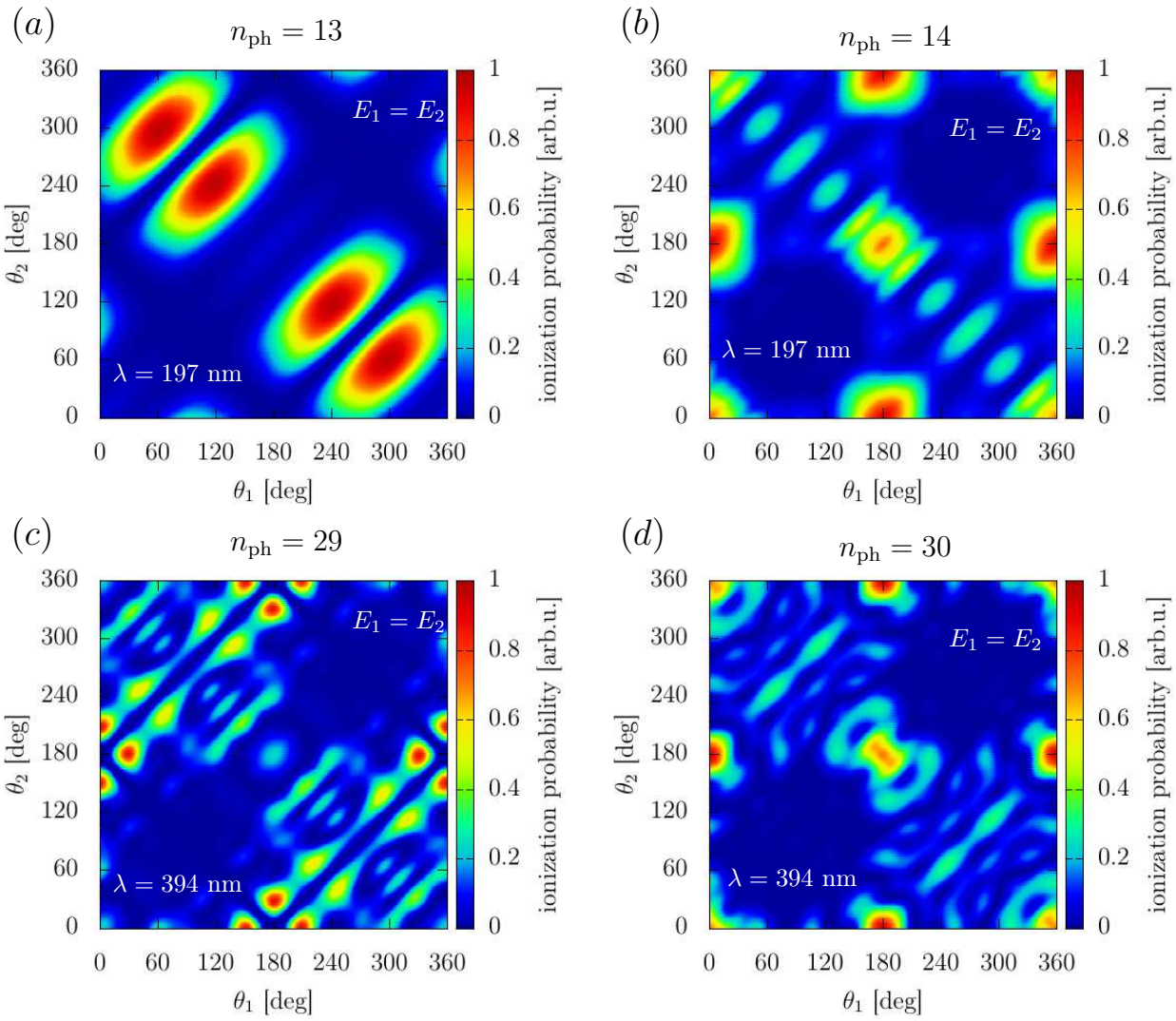

Figure 6.7.: $(a), (b)$ JAD for a linear polarized laser pulse with a wavelength of $\lambda = 197$ nm, a FWHM pulse duration of $T = 3.3$ fs and an intensity of $I = 10^{13}$ W/cm^2. $(c), (d)$ JAD for a linear polarized laser pulse with a wavelength of $\lambda = 394$ nm, a FWHM pulse duration of $T = 6.6$ fs and an intensity of $I = 3.5 \times 10^{14}$ W/cm^2.

7. Time delays in double ionization

In the second part of this thesis we focus on time resolved DI and how timing information can be obtained from experiments. We employ the RABBITT[2] pump-probe scheme consisting of ionization of a target by an attosecond pulse train (APT) as pump together with a weak infrared (IR) field as probe. Thus, interference patterns emerge in the energy spectrum as a function of the delay τ between the central time of the APT and IR field. For the case of single ionization it has been shown that one can unambiguously retrieve [26, 47] the Eisenbud-Wigner-Smith (EWS) time delay [48–50] from this pattern. Thus, the time of the formation of the ionized electron wave packet can be obtained. Following [27] we extend this formalism to DI and apply it to OPDI and TPDI.

7.1. RABBITT

Originally RABBITT was designed to obtain the relative phase differences between different XUV (extreme ultra violet) harmonics forming an APT as generated by high harmonics generation (HHG) [24, 25]. Typically HHG generates a train of attosecond laser pulses with frequencies of odd multiples of the energy of the fundamental IR pulse ω_{IR}. In this work though, we employ it for a different purpose: for known XUV phases the total atomic ionization phases and thus the atomic time delays are calculated [26].
In our simulation the total time-dependent vector potential linearly polarized along $\hat{z}$ [Fig. 7.1(a)] is given by

$$A(t) = A_{\mathrm{env,\,IR}}(t)\sin(\omega_{\mathrm{IR}}t) + \sum_{\mathrm{q}} A_{\mathrm{env,\,APT}}(t)\sin\left[(2q-1)\omega_{\mathrm{IR}}(t-\tau)\right] \tag{7.1}$$

with τ the delay between the IR and the harmonics. We use a $\sin^2$ envelope function for both the IR and the APT consisting of the harmonics H_{2q-1} with energy $\omega_{2q-1} = (2q-1)\omega_{\mathrm{IR}}$ with $q = 16$ to $q = 22$ [Fig. 7.1(b)]. Throughout this chapter we use an IR with $\lambda_{\mathrm{IR}} = 400$ nm corresponding to $\omega_{\mathrm{IR}} = 3.1$ eV.
The underlying principle of RABBITT can be demonstrated with two neighbouring harmonics H_{2q-1} and H_{2q+1}. Absorption of one XUV photon results in main bands (MB) at total electron energies $E_{\mathrm{tot}} = (2q \pm 1)\omega_{\mathrm{IR}} - 79$ eV. For DI of helium a subsequent continuum-continuum transition by absorbing/emitting one IR photon results in a side band (SB) at the same energy $E_{\mathrm{tot}} = (2q)\omega_{\mathrm{IR}} - 79$ eV for both harmonics. As a result, two quantum paths lead to the same SB peak and interfere with each other [Fig. 7.2(a)]. Due to the low intensity of the IR pulse higher-order processes of more than one IR photon can be neglected.

[2] RABBITT is an acronym for Reconstruction of Attosecond Bursts By Interference of Two-photon Transitions.

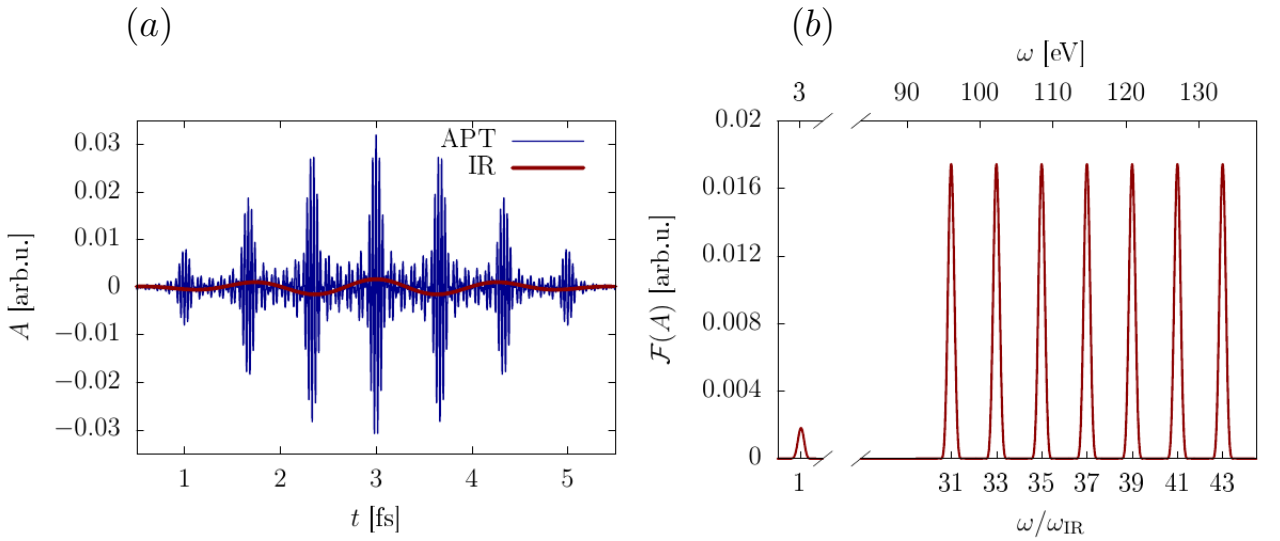

Figure 7.1.: (a) Time-dependent vector potential of the IR pulse with a wave length of $\lambda_{\mathrm{IR}} = 400$ nm ($\omega_{\mathrm{IR}} = 3.1$ eV) an the APT, consisting of the harmonics H_{2q-1} with q from 16 to 22. IR and APT both have a total duration of $T = 6$ fs. (b) Frequency spectrum of the laser pulses shown in (a). The numerical parameters can be found in App. B.6.

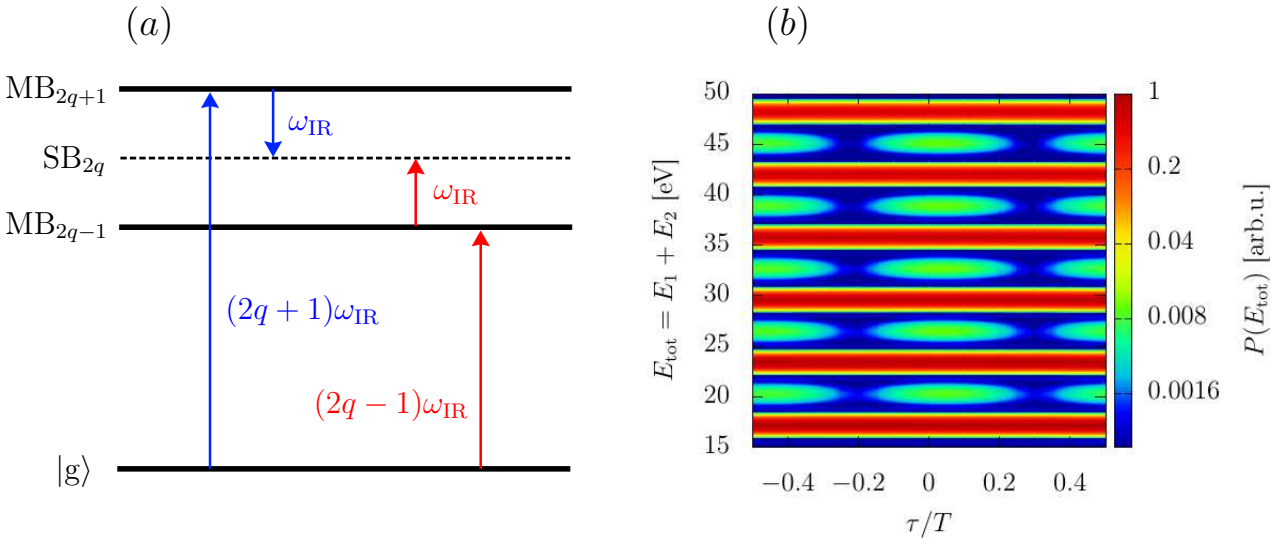

Figure 7.2.: (a) RABBITT scheme of the interfering two-photon transitions involving the absorption of an XUV photon and subsequent emission/absorption of an IR photon. This results in a $2\omega_{\mathrm{IR}}\tau$-beating in the side band (SB) at the energy where the even harmonic would be. (b) RABBITT spectrum for the used APT as a function of the total electron energy $E_{\mathrm{tot}} = E_1 + E_2$, integrated over $\Delta E = E_1 - E_2$, and the delay τ between the IR pulse and the APT. Numerical parameters for (b) are given in App. B.6.

The total transition amplitude from the initial bound state Ψ_i to the final continuum state Ψ_f can be calculated using second-order time-dependent perturbation theory [51]

$$\mathcal{A}^{(2)}_{f\leftarrow i} = -\mathrm{i}\sum\!\!\!\!\!\!\int_n \mathcal{A}^{(2)}_{f\leftarrow n\leftarrow i} = \sum\!\!\!\!\!\!\int_n \mathcal{M}_{f\leftarrow n\leftarrow i}\,\mathcal{G}(E_{fn}, E_{ni}, A_\mathrm{APT}, A_\mathrm{IR}), \tag{7.2}$$

with the transition matrix element

$$\mathcal{M}_{f\leftarrow n\leftarrow i} = \langle\Psi_f|\hat{\mu}|n\rangle\langle n|\hat{\mu}|\Psi_i\rangle, \tag{7.3}$$

where $\hat{\mu}$ is the total dipole operator for both electrons and with the shape function

$$\mathcal{G}(E_{fn}, E_{ni}, A_\mathrm{APT}, A_\mathrm{IR}) = \int_0^{t_f} \mathrm{d}t_1 \int_0^{t_1} \mathrm{d}t_2\; \mathrm{e}^{\mathrm{i}E_{fn}t_1}\mathrm{e}^{\mathrm{i}E_{ni}t_2} A_\mathrm{IR}(t_1)A_\mathrm{XUV}(t_2), \tag{7.4}$$

with $E_{fn} = E_f - E_n$ and $E_{ni} = E_n - E_i$. The integral sum runs over all intermediate states $|n\rangle$ with energies E_n. Taking only two intermediate states in the continuum with energies $E_n = (2q \pm 1)\omega_\mathrm{IR} - 79$ eV into account Eq. (7.2) simplifies to

$$|\Psi(E = E_{2q})|^2 = |\mathcal{A}^{(2)}_{2q\leftarrow 2q+1\leftarrow i} + \mathcal{A}^{(2)}_{2q\leftarrow 2q-1\leftarrow i}|^2 \tag{7.5}$$

for the probability distribution at the SB with $E_f = 2q\omega_\mathrm{IR} - 79$ eV. Similar to RABBITT for SI [26] we write the transition amplitude corresponding to a single quantum mechanical path as

$$\mathcal{A}_{2q\leftarrow 2q\pm 1\leftarrow i} = |\mathcal{A}_{2q\leftarrow 2q\pm 1\leftarrow i}|\mathrm{e}^{\mp\mathrm{i}\omega_\mathrm{IR}\tau}\mathrm{e}^{\mathrm{i}\Phi_\mathrm{R}(E_1,E_2)}, \tag{7.6}$$

The factor $\mathrm{e}^{\mp\mathrm{i}\omega_\mathrm{IR}\tau}$ stems from the emission (absorption) of one IR photon and the delay between the peak time of the IR and the APT. Inserting Eq. (7.6) into Eq. (7.5) results in

$$|\Psi(E = E_{2q})|^2 = C + 2|\mathcal{A}_{2q\leftarrow 2q+1\leftarrow i}||\mathcal{A}_{2q\leftarrow 2q-1\leftarrow i}|\cos(2\omega_\mathrm{IR}\tau + \Delta\Phi_\mathrm{R}) \tag{7.7}$$

where C denotes the terms which are independent of τ [Fig. 7.2(b)]. Similar to SI [30] we define

$$t_\mathrm{R} = -\frac{\Delta\Phi_\mathrm{R}}{2\omega_\mathrm{IR}} \tag{7.8}$$

as the approximate time delay as retrieved by RABBITT. In order to extract $\Delta\Phi_\mathrm{R}$ the data points at each SB are fitted by use of the non-linear least squares method to the following function:

$$S_\mathrm{fit}(\tau) = \alpha + \beta\cos(2\omega\tau + \Delta\Phi), \tag{7.9}$$

where $\Delta\Phi$ is the parameter we are interested in.

7.2. Time delays in one-photon double ionization

Time delays for SI have been extensively studied in the past [47] and are already well understood. For SI of non-polarizable targets two contributions have been identified to the RABBITT phase $\Delta\Phi_{\mathrm{R}}$ [Eq. (7.7)]

$$\Delta\Phi_{\mathrm{R}}^{\mathrm{SI}} = \Delta\eta^{\mathrm{SI}} + \Delta\Phi_{\mathrm{cc}} = \eta^{\mathrm{SI}}(E-\omega_{\mathrm{IR}}) - \eta^{\mathrm{SI}}(E+\omega_{\mathrm{IR}}) + \Phi_{\mathrm{cc}}^{+} - \Phi_{\mathrm{cc}}^{-}. \tag{7.10}$$

$\eta^{\mathrm{SI}}(E)$ is the scattering phase the one-electron wave packet acquires by the XUV driven ionization to a continuum state with energy E. The derivative of η^{SI} with respect to the electron energy E results in the Eisenbud-Wigner-Smith time delay $t_{\mathrm{EWS}}^{\mathrm{SI}} = \partial\eta^{\mathrm{SI}}/\partial E$. The continuum-continuum phase $\Phi_{\mathrm{cc}}^{\pm}$ stems from the absorption (Φ_{cc}^{+}) or emission (Φ_{cc}^{-}) of an IR photon in the presence of the long-ranged Coulomb potential. For sufficiently high electron energies Φ_{cc} was analytically calculated to be [52]

$$\Phi_{\mathrm{cc}}(k,\kappa) = \arg\left\{\frac{(2\kappa)^{\mathrm{i}Z/\kappa}}{(2k)^{\mathrm{i}Z/k}}\frac{\Gamma[2+\mathrm{i}Z(1/\kappa-1/k)+\gamma(k,\kappa)]}{(\kappa-k)^{\mathrm{i}Z(1/\kappa-1/k)}}\right\}, \tag{7.11}$$

with

$$\gamma(k,\kappa) = \mathrm{i}Z\frac{(\kappa-k)(\kappa^2+k^2)}{2\kappa^2k^2}\Gamma[1+\mathrm{i}Z(1/\kappa-1/k)], \tag{7.12}$$

and $\Gamma(x)$ being the gamma function, Z the asymptotic charge of the residual ion ($Z=1$ for SI), k the momentum of the final state of the electron wave packet and κ the momentum of the intermediate state, before absorption/emission of one IR photon. In the single ionization photo electron spectrum (SI-PES) for zero delay between IR and APT (using the APT shown in Fig. 7.1) each MB is the result of the absorption of one XUV photon. The absorption/emission of an additional IR photon results in the SBs which oscillate with τ, with a frequency $2\omega_{\mathrm{IR}}$. The resulting SI time delays are shown in Fig. 7.3.

Following the pioneering work of Månsson et al. [27] we extend this formalism to OPDI. Månsson et al. theoretically describe the DI RABBITT time delay by

$$t_{\mathrm{R}}^{\mathrm{DI}} = -\frac{\Delta\Phi}{2\omega_{\mathrm{IR}}} = t_{\mathrm{EWS}}^{\mathrm{DI}} + t_{\mathrm{cc}}^{\mathrm{DI}} + t_{\mathrm{ee}} = \frac{1}{2}\left(\frac{d\eta_1}{dE_1}+\frac{d\eta_2}{dE_2}\right) + \frac{1}{2}\left(t_{\mathrm{cc},1}+t_{\mathrm{cc},2}\right) + t_{\mathrm{ee}}, \tag{7.13}$$

with

$$t_{\mathrm{cc,i}} = \frac{\Phi_{\mathrm{cc}}(E_i, E_i+\omega_{\mathrm{IR}}) - \Phi_{\mathrm{cc}}(E_i, E_i-\omega_{\mathrm{IR}})}{2\omega_{\mathrm{IR}}}, \tag{7.14}$$

and t_{ee} stemming from the electron-electron interaction. This approximation is only valid if the two-electron scattering phase $\eta^{\mathrm{DI}}(E_1,E_2)$ factorizes for the respective electrons $\eta^{\mathrm{DI}}(E_1,E_2) = \eta_1(E_1)\eta_2(E_2)$, as only then

$$\frac{d\eta(E_1,E_2)}{d(E_1+E_2)} = \frac{1}{2}\left(\frac{d\eta_1}{dE_1}+\frac{d\eta_2}{dE_2}\right) \tag{7.15}$$

holds true, where $\eta(E_1,E_2)$ is the one-photon transition matrix element

$$\eta(E_1,E_2) = \arg\{\langle\Psi_f(E_1,E_2)|\hat{\mu}|\Psi_i\rangle\}. \tag{7.16}$$

In order to achieve results comparable to SI, we integrate the DI photo electron spectrum [Fig. 7.4(a)] over $\Delta E = E_1 - E_2$ [Fig. 7.4(b)]. We find a significant relative delay between SI and DI with the main contribution from the DI time delay [Fig. 7.4]. This result implicates that the doubly ionized wave packet needs more time to form compared to the singly ionized wave packet.
In order to gain additional insight into the DI time delay, we analyse the DI time delays as function of the energy difference ΔE for fixed E_{tot}. The RABBITT spectrum in Fig. 7.5(a) shows a distinct cosine oscillation for each value ΔE along lines of constant E_{tot}. Accordingly, we can extract a RABBITT phase $\Delta\Phi_{\text{R}}$ and thus a time delay t_{R} along the diagonal for each SB [Fig. 7.5(b)]. Except for energies where the slow electron approaches zero ($\Delta E/E_{\text{tot}} \approx \pm 1$), t_R is almost constant and the dependence on ΔE is negligible. For ΔE outside the dashed lines in Fig. 7.5 corresponding to an energy range of ω_{IR}, t_R strongly fluctuates. A possible reason for this is the broken symmetry between the electrons. Outside the edge region each SB point can be reached by four quantum paths, as both electrons can absorb or emit one IR photon. In the edge regime only three quantum paths exist, as the energy of the slow electron would be negative after emitting one IR photon. Thus, this process is forbidden. Despite this asymmetry between the electrons the SB signal still exhibits a clear cosine oscillation and a time delay can be extracted. The physical interpretation is, however, not straightforward and beyond the scope of this work.
The dependence of t_{R}^{DI} on the total energy E_{tot} is unambiguous though, as t_{R}^{DI} continually decreases with increasing E_{tot}. For time delays in SI a similar electron energy dependence has been observed [47], as is indicated in Fig. 7.3(b).
In order to get a qualitative understanding of the different contributions to t_{R}^{DI} [Eq. (7.13)] we employ a classical trajectory Monte Carlo (CTMC) simulation in one spatial dimension. In this method the spatial starting parameters z_0 are randomly chosen according to the quantum mechanical groundstate distributionx. Starting momenta are then repeatedly chosen at random and cases where the total asymptotic kinetic energy of the electrons do not agree with Eq. (6.1) are discarded. The trajectories are calculated using the classical equations of motion for electrons in a Coulomb potential and an IR laser field. At the end of propagation the tangential curve and its intersection with the atomic core ($z = 0$) are calculated for each electron separately [Fig. 7.6(a)]. This intercept is interpreted as a time delay [47] and the sum for both electrons $t_{\text{CTMC}} = (t_{\text{CTMC}}^{(1)} + t_{\text{CTMC}}^{(2)})/2$ results in a qualitative approximation to t_{cc}.
Comparing the CTMC time delay to t_{R}^{DI} [Fig. 7.6(b)] shows that both are in a large energy range around $\Delta E = 0$ nearly independent of ΔE. For strongly asymmetric energy sharing ($\Delta E/E_{\text{tot}} \approx \pm 1$) t_{CTMC} decreases rapidly to large negative time delays. This trend is also present in the analytic approximation for $t_{\text{cc}}^{\text{DI}}$. The time delay $t_{\text{EWS}}^{\text{DI}}$ calculated from the scattering phase mirrors the behaviour of $t_{\text{cc}}^{\text{DI}}$ as it rapidly increases for $\Delta E/E_{\text{tot}}$ approaching ± 1. Neglecting t_{ee} the sum $t_{\text{EWS}}^{\text{DI}} + t_{\text{cc}}^{\text{DI}}$ [using Eq. (7.13)] at least qualitatively explains the almost flat shape of t_{R}^{DI}.
Comparing now $t_{\text{EWS}}^{\text{DI}} + t_{\text{cc}}^{\text{DI}}$ (with $Z = 2$ for DI) and $t_{\text{EWS}}^{\text{DI}} + t_{\text{CTMC}}$ with our results for t_{R}^{DI} as function of E_{tot} for $\Delta E = 0$, we observe a qualitative agreement for $t_{\text{EWS}}^{\text{DI}} + t_{\text{cc}}^{\text{DI}}$, but the time delays are shifted by approximately 50 as. Possible reasons for this offset for $t_{\text{EWS}} + t_{\text{cc}}$ are the

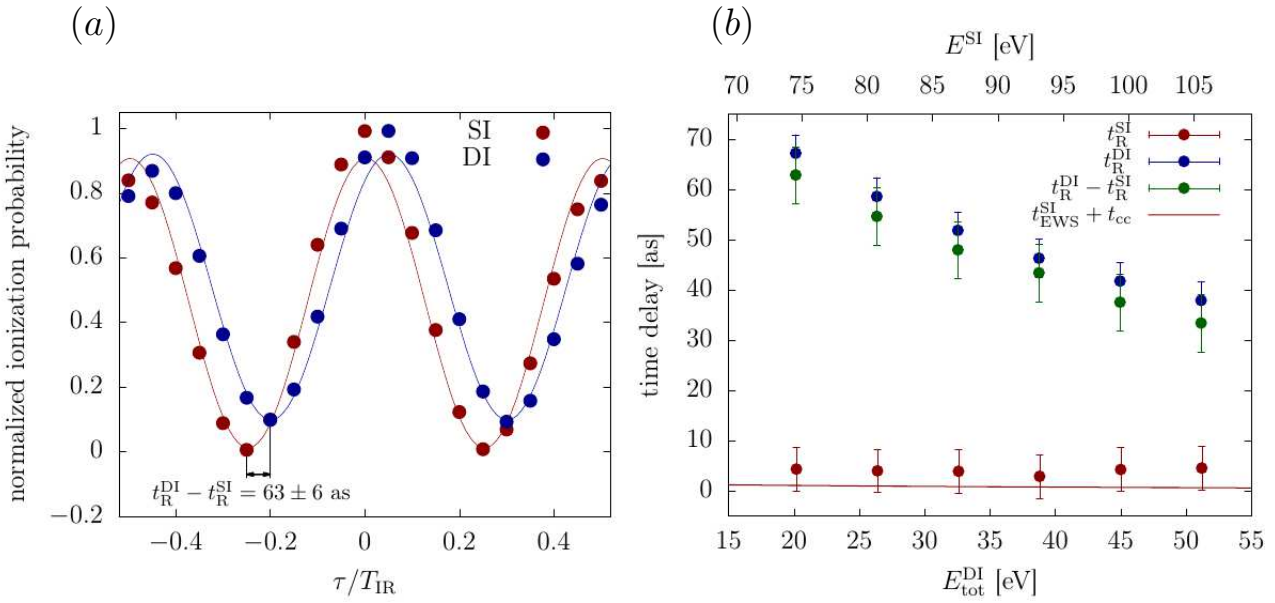

Figure 7.3.: (a) Ionization probabilities taken from the SI-PES ($E = 74.6$ eV) and from the DI-PES ($\Delta E = 20.1$ eV) integrated over ΔE for different delays τ between the IR pulse and the APT. The lines are obtained from a fit to Eq. (7.9).(b) Resulting time delays for SI, DI and the relative time delay. The error bars mark the error from the fitting procedure.

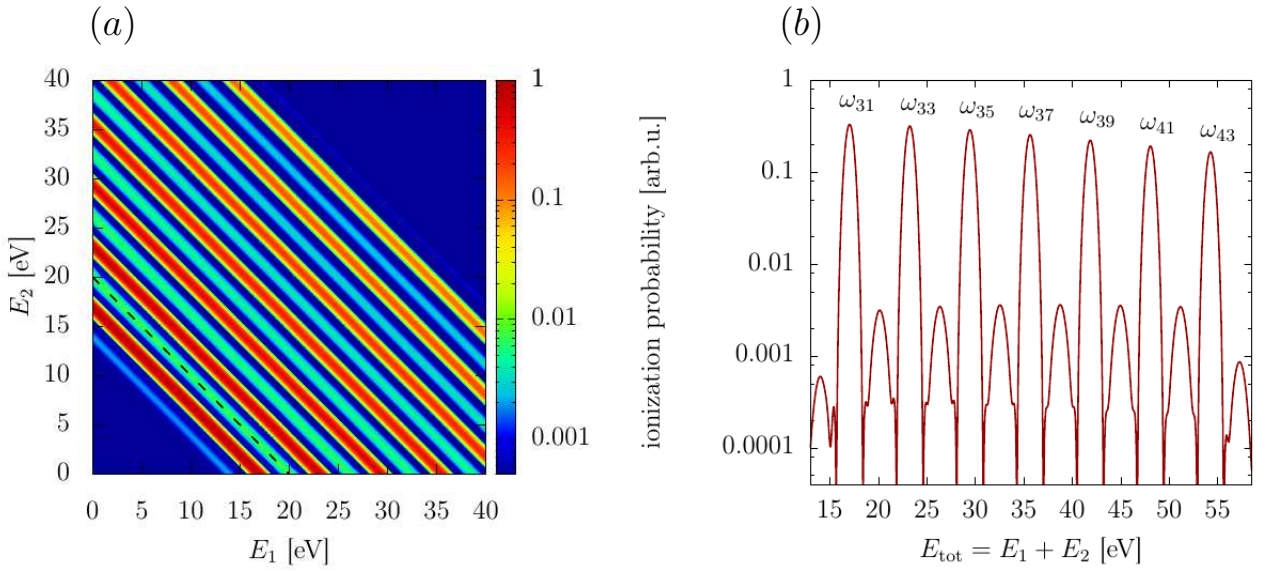

Figure 7.4.: (a) DI-PES for a laser pulse with a wave length $\lambda = 400$ nm and an APT consisting of the harmonics H_{2q-1} with $q = 16$-22 for $\tau = 0$. Each pulse has a total duration $T = 6$ fs. (b) Spectrum integrated over $\Delta E = E_1 - E_2$. The black dashed line indicates the energy range shown in Fig. 7.5(a).

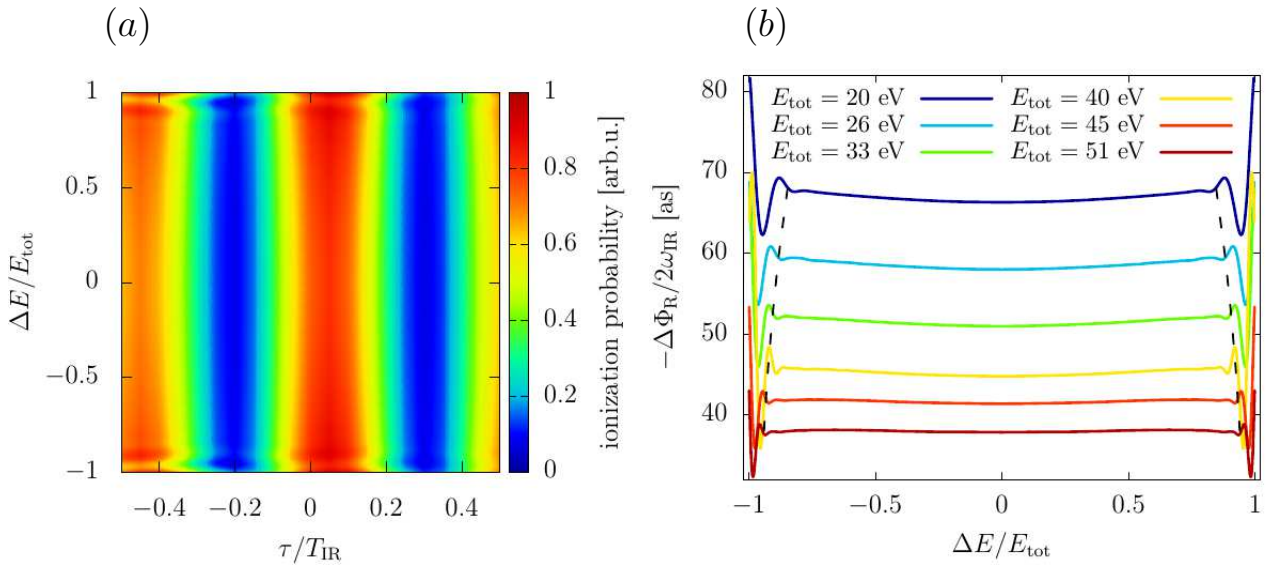

Figure 7.5.: (a) DI RABBITT spectrum as a function of the normalized delay τ between the IR pulse and the APT for the lowest lying SB, marked by the black dashed line in Fig. 7.4(a). (b) RABBITT time delays calculated for each SB. The dashed black lines indicate the energies with $E_1 = \omega_{\rm IR}$, $E_2 = E_{\rm tot} - \omega_{\rm IR}$ and vice versa.

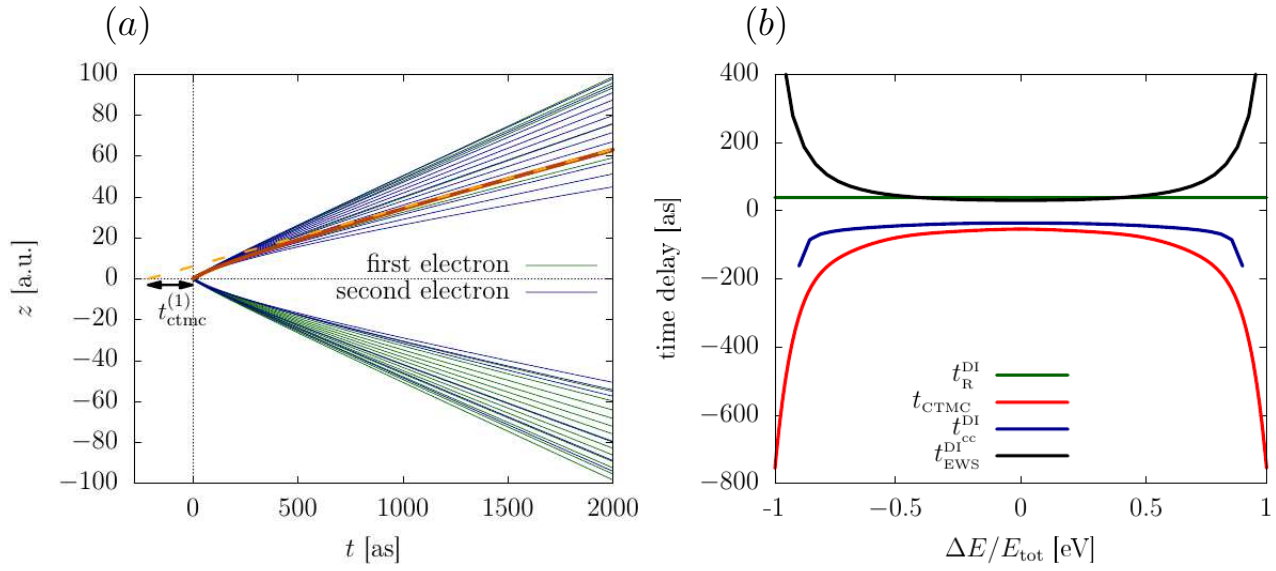

Figure 7.6.: (a) Trajectories of both electrons in one dimension from a CTMC simulation. The red trajectory with its asymptotic tangent (dashed orange line) highlights how time delays are extracted within this method. (b) RABBITT time delay $t^{\rm DI}_{\rm R}$ for the highest lying SB at $E_{\rm tot} = 51$ eV (green line). Analytic values for the continuum-continuum delay $t^{\rm DI}_{\rm cc}$ (blue line). Numerical approximation to $t^{\rm DI}_{\rm cc} + t_{\rm ee}$ using a CTMC calculation (red line). Numerical calculation of $t^{\rm DI}_{\rm EWS} = d\eta(E_1, E_2)/dE_{\rm tot}$ with η from Eq. (7.16) (black line).

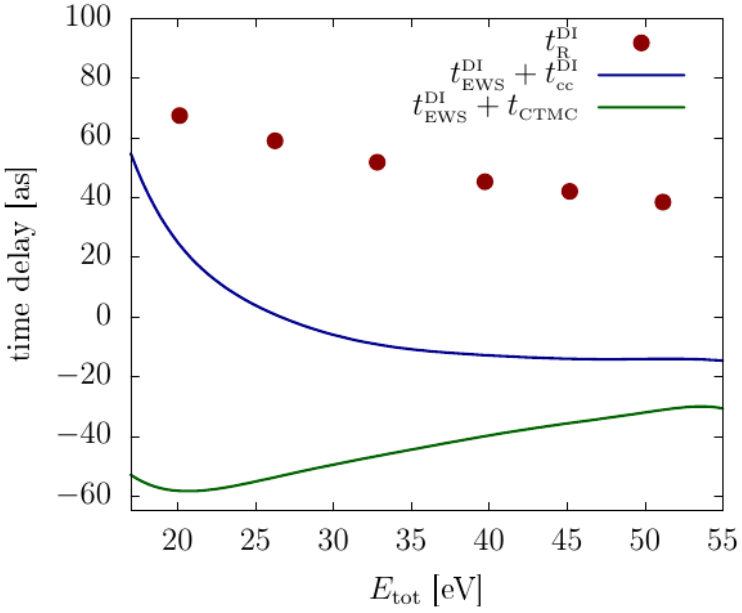

Figure 7.7.: Time delays $t_{\mathrm{R}}^{\mathrm{DI}}$ as function of E_{tot} for $\Delta E = 0$ Red dots: RABBITT time delays. Blue line: Analytic approximation consisting of $t_{\mathrm{cc}}^{\mathrm{DI}}$ and $t_{\mathrm{EWS}}^{\mathrm{DI}}$ [Eq. (7.13)]. Green line: Sum of $t_{\mathrm{EWS}}^{\mathrm{DI}}$ and the time delays from the CTMC calculation.

inaccuracy of Eq. (7.11) for OPDI as the asymptotic charge Z is not defined properly[3] if both electrons are close to the core and that we assume t_{ee} to be zero, which is surely wrong. Put differently one could also argue that the difference between $t_{\mathrm{R}}^{\mathrm{DI}}$ and $t_{\mathrm{EWS}} + t_{\mathrm{cc}}$ is exactly t_{ee}. The results for $t_{\mathrm{EWS}} + t_{\mathrm{CTMC}}$ do in principle include some part of the electron-electron delay t_{ee}, nevertheless, the 1D-CTMC calculation most likely overestimates the influence of the Coulomb interaction. Thus, a disagreement between $t_{\mathrm{R}}^{\mathrm{DI}}$ and $t_{\mathrm{EWS}} + t_{\mathrm{CTMC}}$ is expected.

7.3. Time delays in two-photon double ionization

In the final part of this chapter we present first results for timing information of TPDI using RABBITT[4]. We use the same laser parameters as in the previous section with the exception of limiting the APT to three harmonics with q = 16-18 (see App. B.6). The XUV photon energies are above the second ionization potential $I_2 = 54.4$ eV, thus, together with the long FWHM pulse durations ($T = 3$ fs) we are well within the sequential regime [11]. In contrast to the previous section where the DI-PES consisted of continuous bands, we have now distinct peaks in the PES at energies given by $E_1 = \omega_{\mathrm{XUV}} - I_1$, $E_2 = \omega_{\mathrm{XUV}} - I_2$ and vice versa.

[3] In the work by Månsson et al. an asymptotic charge of $Z \approx 1.7$ is used.
[4] Complementary to this work time resolved TPDI has also been investigated for streaking [53].

7.3.1. Shape function

In order to get a better understanding of the underlying sequential two-photon transition process, we analyse the shape function for the absorption of two XUV photons $\mathcal{G}(E_1, E_2, A_{\mathrm{APT}}, A_{\mathrm{APT}})$ [Eq. (7.4)]. The shape function is the part of the transition amplitude that contains information on the temporal shape of the laser pulse which depends strongly on the pulse envelope and the pulse duration [29]. It does, however, contain no system-specific information. The time integrals in Eq. (7.4) correspond to a two-dimensional Fourier transformation of the XUV vector potentials and can explicitly be solved [Fig. 7.8]. For TPDI with an APT consisting of 3 XUVs 9 different XUV combinations are possible, thus leading to the main pattern of 9 (18 when the electron symmetry is considered) distinct peaks. Each peak has exactly the same intensity since we do not consider the energy dependence of the cross section for the calculation of the shape function. From the phase of the shape function at the peaks a time delay can be defined for each electron

$$t_{\mathrm{s}}^{1,2} = -\frac{\partial}{\partial E_{1,2}} \arg\{\mathcal{G}(E_1, E_2)\}. \tag{7.17}$$

This time delay contribution from the shape function is completely independent of the energy sharing between the electrons ΔE and the total energy E_{tot}. The shape function time delay does, however, strongly depend on the temporal shape of the laser pulse, particularly on the pulse duration [Tab. 7.1]. Close investigation of the relative time delay reveals that Δt_{s} increases linearly with the pulse duration, resembling the trend observed for streaking of TPDI [53].

Table 7.1.: Time delays for different FWHM pulse durations T using Eq. (7.17).

T [fs]	t_{s}^1 [as]	t_{s}^2 [as]	Δt_{s} [as]
2	−66	−100	34
4	−131	−199	68
6	−299	−197	102
8	−398	−262	136
10	−498	−326	172

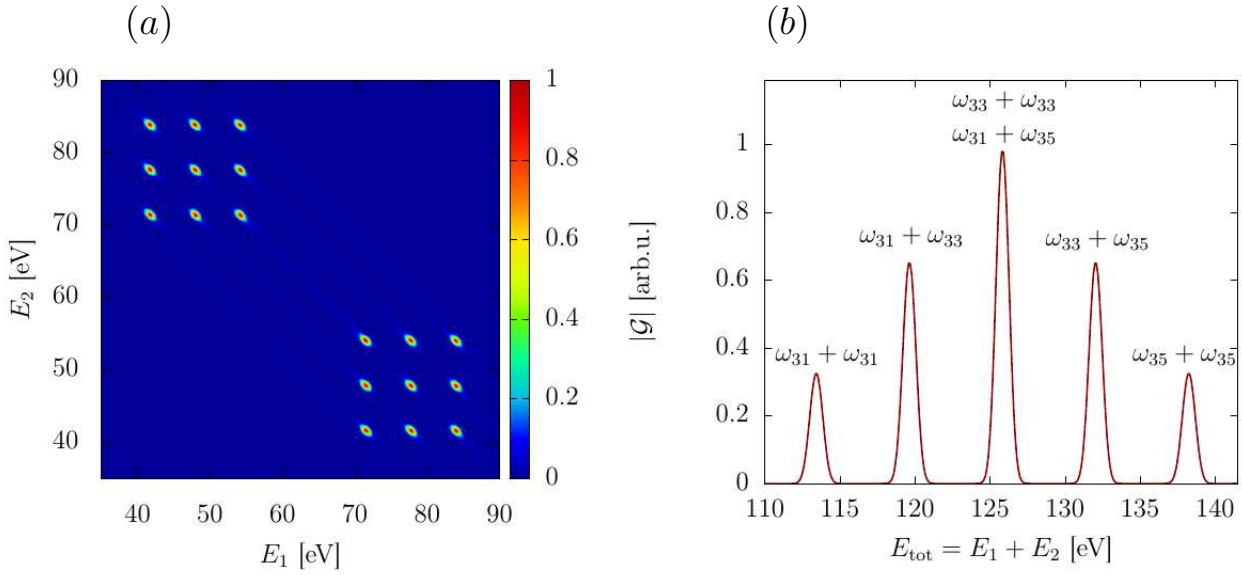

Figure 7.8.: (a) Pulse-dependent shape function $|\mathcal{G}(E_1, E_2, T)|$ in two-photon transitions for an APT consisting of the harmonics H_{2q-1} with q = 16-18 and a FWHM duration of $T = 3$ fs. (b) Shape function $|\mathcal{G}(E_1, E_2, T)|$ integrated over $\Delta E = E_1 - E_2$.

7.3.2. RABBITT

Employing the full time-dependent simulation including APT and IR, additional side peaks appear in the doubly differential PES between the main peaks as a result of the emission/absorption of one IR photon together with the absorption of two XUV photons [Fig. 7.9]. Compared to RABBITT for OPDI there is an important conceptual difference. For OPDI every point in the SB, except for the edges, is reachable by both electrons through absorption/emission of an IR photon. For sequential TPDI the side peaks are the result of the absorption/emission of one IR photon by one specific electron. Thus, we hypothesize that only either t^1_{EWS} (side peaks horizontally between main peaks) or t^2_{EWS} (side peaks vertically between main peaks) contributes to the measured time delay [Fig. 7.10] Our results seem to confirm this, as all the calculated time delays cluster around two values, with $t^{\mathrm{DI}}_{\mathrm{R}} \approx -18$ as for the faster electron and $t^{\mathrm{DI}}_{\mathrm{R}} \approx 31$ as for the slower electron. For OPDI this distinction is not possible as for each point of the side band the measured time delay is a function of $(t^1_{\mathrm{EWS}} + t^2_{\mathrm{EWS}})/2$ and thus nearly independent of ΔE [Fig. 7.5(b)].
In order to gain additional insight into the TPDI time delay, we calculate the time delays along fixed total energies (marked by dashed lines in Fig. 7.10). The ionization probability $P(E_1, E_2)$ exhibits a clear cosine oscillation with regards to τ, thus, $t^{\mathrm{DI}}_{\mathrm{R}}$ can be extracted for each point along ΔE (Fig. 7.11). $t^{\mathrm{DI}}_{\mathrm{R}}$ smoothly oscillates between the extremal time delay values associated with the slower and the faster electron. Further, it shows a distinct dependence on the XUV pulse duration. For OPDI this dependence nearly vanishes due to the averaging over both electrons [47].

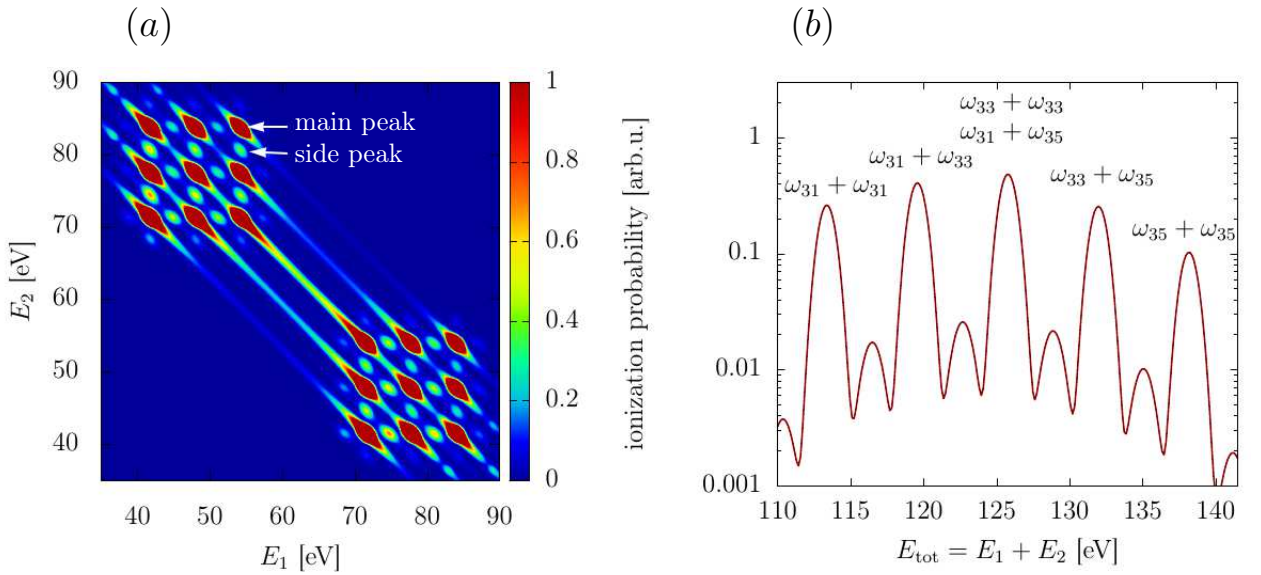

Figure 7.9.: (a) DI-PES for a laser pulse with a wave length $\lambda = 400$ nm and an APT consisting of the harmonics H_{2q-1} with $q = 16$-18 for $\tau = 0$. Each pulse has a FWHM duration $T = 3$ fs. In the shown energy range two XUV photons are absorbed. (b) PES shown in (a) integrated with regards to $\Delta E = E_1 - E_2$.

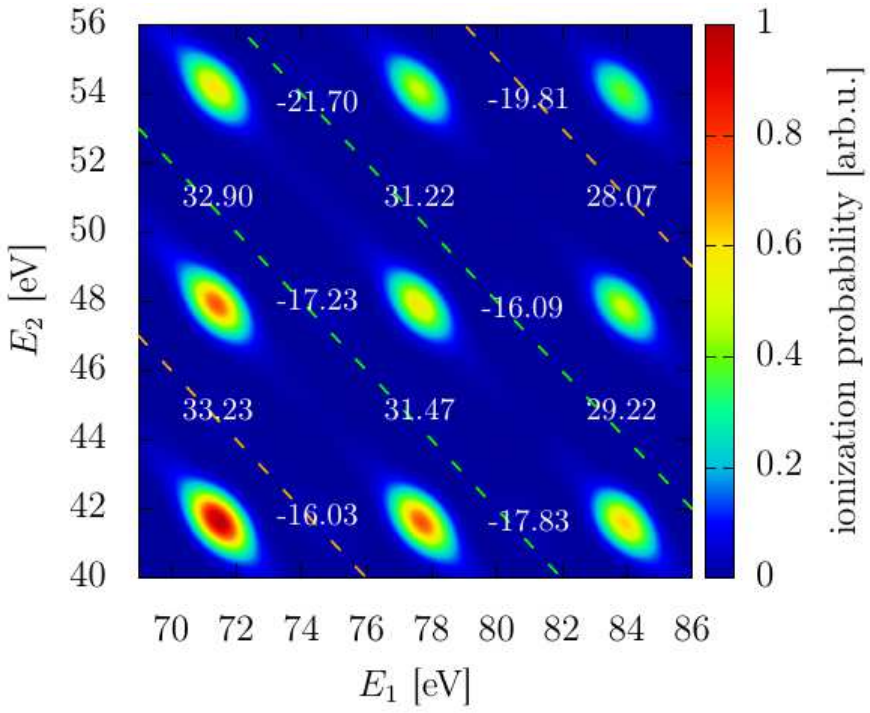

Figure 7.10.: Close up of Fig. 7.9(a). The calculated RABBITT time delays $t_{\mathrm{R}}^{\mathrm{DI}}$ (in as) are shown at the peaks resulting from the absorption of 2 XUV photons and the subsequent absorption or emission of one IR photon.

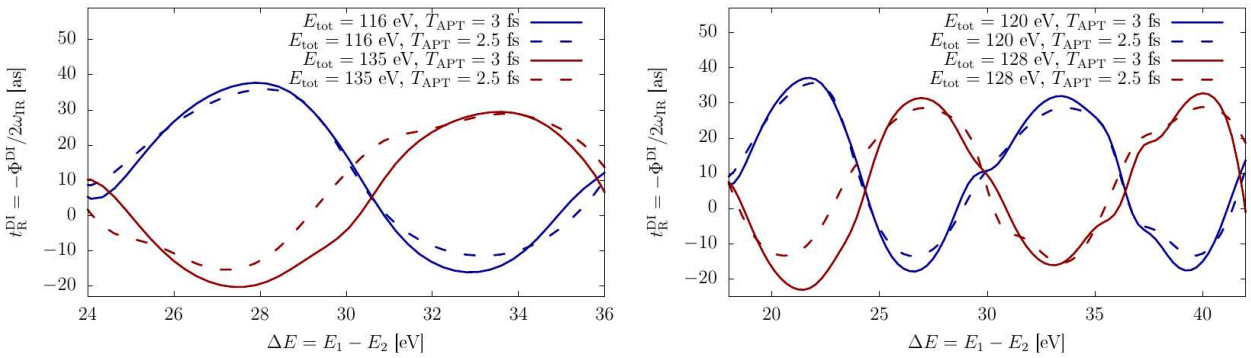

Figure 7.11.: RABBITT time delays $t_{\rm R}^{\rm DI}$ calculated at each point of the diagonal in Fig. 7.10 (marked by dashed lines) with total energy (a) $E_{\rm tot} = 116$ eV and $E_{\rm tot} = 135$ eV (orange lines), (b) $E_{\rm tot} = 122$ eV and $E_{\rm tot} = 128$ eV (green lines). Full lines show the time delays for an APT with a FWHM duration of $T_{\rm APT} = 3$ fs and dashed lines for $T_{\rm APT} = 2.5$ fs.

8. Summary and outlook

Double ionization (DI) of atomic helium has been among the most intensively studied topics in atomic physics over the course of the last few decades, both by experimental as well as theoretical researchers. The reason is that double ionization of helium allows to study details of the electron-electron interaction while still being simple enough to be treatable with numerical calculations or perturbative analytical models. Nevertheless, the insights gained from this simple process are valuable to understand more complicated processes involving the interaction of light with matter whenever correlations between the electrons play an important role.
Due to computational and experimental limitations most of the literature focuses either on double ionization by absorption of few (one to two) but high energetic photons [18–21, 35, 37, 43], or on the long wavelength regime where absorption of more than 25 photons is needed [13, 14, 16, 22, 46]. Interestingly, the processes in these two regimes can be explained by drastically different theoretical methods. While for one- or two-photon double ionization perturbative calculations have proven to be very powerful, in the long-wavelength (or strong field) regime classical calculations together with static field ionization rates have been used extensively.
Within this thesis we aimed at bridging this gap by analysing similarities and differences between these two regimes by studying double ionization of helium for various wavelengths of the ionizing pulse ranging from one-photon double ionization ($\omega \approx 100$ eV) up to strongly non-perturbative double ionization ($\omega \approx 3$ eV) using highly accurate *ab-initio* simulations. For this purpose, we have extended our previous numerical implementation [35, 37] by projecting onto Volkov-states during the propagation, which reduces the numerical complexity of the problem. We have shown that the angular distributions reveal remarkable similarities for a large range

of laser frequencies and that the dominant features do only depend on whether an even or an odd number of photons is absorbed. For even number of photons and equal-energy sharing the ionized electrons prefer ionization into opposite directions, while for odd number of photons a relative angle of 120° is preferred. Most of these features are caused by the quantum mechanical propensity rules resulting from parity conservation. Thus, they even hold qualitatively for the experimentally accessible strong-field regime ($\lambda = 394$ nm).
For one to five-photon DI we have additionally investigated DI by elliptically polarized laser pulses. In line with several experimental and analytical results [19–21], we have found a strong circular dichroism. The circular dichroism does not depend on the pulse duration of the ionizing pulse and is strongest for low electron energies. Further, there is no clear connection between the extent, or even the sign, of the circular dichroism for a particular relative angle between the ionized electrons and the number of photons absorbed.
Pioneering experiments have shown that for a wavelength of $\lambda = 800$ nm the DI probability is significantly enhanced for a certain intensity range, due to DI by the recolliding singly ionized electron [13]. Our results for $\lambda = 100$ nm do not reveal such an enhancement, since the energy of the returning electron is not high enough for the intensities accessible with the present numerical implementation and resources. We have not been able to achieve converged DI probabilities for higher wavelengths.
In the second part of this thesis we have focused on time-resolving one- and two-photon double ionization using the interferometric RABBITT technique [24, 26, 52] extending and following a recent experiment [27]. We found that for one-photon double ionization the doubly ionized wavepacket needs significantly more time to form, compared to the singly ionized wavepacket. Similarly to single ionization, the obtained time delay decreases rapidly for higher total energies. Interestingly, the time delay is almost independent of the energy difference between the two electrons, and depends only on the total energy.
For two-photon double ionization we have shown that the doubly differential electron distribution allows to clearly distinguish between the time delay of the first and the second electron, thus allowing us to unambiguously determine the time difference between the emission of the two electrons. Similar to results obtained from streaking calculations [53], the calculated time delay shows a dependence on the duration of the ionizing XUV pulse. The reason for this is that two-photon double ionization can happen sequentially for the investigated XUV energy.

Even though the presented results provide insights into the correlated double ionization dynamics, several questions are still open. Especially double ionization for $\lambda > 100$ nm is still very challenging for state of the art numerical implementations. For one-photon double ionization it would be interesting to disentangle the different contributions to the retrieved time delay and quantify their dependence on the total energy and energy difference of the two electrons. In the case of two-photon double ionization the results presented here are not sufficient to draw definite conclusions about the obtained time delays. More calculations are needed to test the dependence of the delay on the pulse duration and to understand the discrepancies compared to the time delays obtained from streaking simulations.

A. Details of the numerical implementation

In this appendix we shortly describe the numerical implementation of the spatial discretization and the time propagation. Four out of the six spatial degrees of freedom are already discretized expanding the wave function in coupled spherical harmonics Eq. (2.9). The remaining two radial coordinates are discretized using the finite-element discrete-variable-representation (FEDVR) [54, 55]. The radial coordinates are divided into elements where the local wave function is represented using Gauss-Lobatto polynomials [56]. FEDVR combines the sparse matrix representation of operators of grid-based methods with the accuracy of basis set expansion methods. In this work each FE spanned 4 a.u. with 11 normalized radial FEDVR basis functions, allowing a maximum electron energy of around 4 a.u..
For the time propagation the short iterative Lanczos method based on the Krylov subspace approximation with adaptive time step control was employed. The boundaries $r_{\max}$ of the chosen radial grid act as hard walls, thus upon reaching them the wave function would be reflected back resulting in non-physical interferences. For cases where this cannot be avoided, i.e. when it is numerically not feasible to have a large enough box, we employ a complex absorption potential centred at r_{cut}

$$a(r) = i\alpha\theta(r - r_{\text{cut}}) \ln\cos\left(\frac{r - r_{\text{cut}}}{r_{\max} - r_{\text{cut}}}\right) \tag{A.1}$$

The strength of the potential (α) and r_{cut} have to be chosen such that the wave function is damped to zero before it reaches the boundary $r_{\max}$.

B. Parameters for the different simulations

In this appendix we list all numerical parameters used for the simulations presented in the main part of this work.

B.1. Pulses and envelopes

We use linearly and elliptically polarized laser pulses defined by the vector potential

$$\mathbf{A}_{\text{lin}}(t) = A_0 f(t) \begin{pmatrix} 0 \\ 0 \\ \cos(\omega t) \end{pmatrix}, \tag{B.1}$$

for linear polarization and

$$\mathbf{A}_{\text{ell}}(t) = A_0 f(t) \frac{1}{\sqrt{1+\epsilon^2}} \begin{pmatrix} \sin(\omega t) \\ \epsilon \cos(\omega t) \\ 0 \end{pmatrix}, \tag{B.2}$$

for elliptical polarization where $I = A_0^2$ is the peak intensity. The envelope function $f(t)$ is either given by a squared sine

$$f_{\sin^2}(t) = \sin^2\left(\frac{\pi t}{2T}\right), \tag{B.3}$$

or a Gaussian

$$f_{\text{gauss}}(t) = \exp\left(\frac{-2\ln(2)(t-2T)^2}{T^2}\right), \tag{B.4}$$

where T is the full width half maximum (FWHM) duration.

B.2. Parameters for Ch. 4

We use a laser pulse with wave length $\lambda = 12.5$ nm (amounting to an energy of 99 eV), with a FWHM duration T of 2 fs, an intensity of $I = 10^{14}$ W/cm^2 and a squared sine envelope. We use a radial box spanning 192 a.u. $\times$ 192 a.u. An absorbing boundary starting at 182.4 a.u. and a cut-off for analytical propagation starting at 144 a.u. is used. For the close-coupling expansion we employ maximal total angular momenta up to $L_{\max} = 3$ and individual angular momenta up to $\ell_{1,\max} = \ell_{2,\max} = 10$, corresponding to 57 partial waves for linear polarization and 156 for circular polarization.

B.3. Parameters for Ch. 5

The respective pulse parameters are given in Tab. B.1. For each pulse a Gaussian envelope is used with a peak intensity of $I = 10^{14}$ Watt/cm^2. We use a radial box spanning 240 a.u. $\times$ 240 a.u. An absorbing boundary starting at 228 a.u. and a cut-off for analytical propagation starting at 180 a.u. is used.

Table B.1.: Pulse and close-coupling parameters used for the results shown in Ch. 5.

λ [nm]	ω [eV]	$L_{\max}$	$\ell_{1,\max} = \ell_{2,\max}$	FWHM duration [as]	$n_{\text{part}}^{\text{lin}}$	$n_{\text{part}}^{\text{circ}}$
25.3	49 eV	4	12	210	99	340
42.7	29 eV	4	12	357	99	340
56.4	22 eV	5	14	470	150	602
68.9	18 eV	6	14	574	192	740

B.4. Parameters for Sec. 6.1

We employ pulses with a wave length $\lambda = 98.5$ nm (corresponding to an energy of 12.6 eV). The respective pulse parameters are given in Tab. B.2. For each pulse a $\sin^2$ envelope is used. We use a radial box spanning 240 a.u. $\times$ 240 a.u. An absorbing boundary starting at 228 a.u. and a cut-off for analytical propagation starting at 180 a.u. is used.

Table B.2.: Pulse and close-coupling parameters used for the results shown in Sec. 6.1.

Figure	Intensity [W/cm^2]	$L_{\max}$	$\ell_{1,\max} = \ell_{2,\max}$	FWHM duration [fs]	$n_{\text{part}}^{\text{lin}}$
6.1	10^{15}	13	16	1.7	588
6.3	-	8	8	4	125
6.4	10^{15}	13	16	1.7	588
$6.5(a),(c)$	10^{15}	13	16	1.7	588
$6.5(b),(d)$	10^{15}	13	16	0.8	588

B.5. Parameters for Sec. 6.2

We employ pulses with a $\sin^2$ envelope and a FWHM duration of 5 optical cycles. The respective pulse parameters can be seen in Tab. B.3. We use a radial box spanning 240 a.u. $\times$ 240 a.u. An absorbing boundary starting at 228 a.u. and a cut-off for analytical propagation starting at 180 a.u. is used.

Table B.3.: Pulse and close-coupling parameters used for the results shown in Sec. 6.2.

Figure	Intensity [W/cm^2]	$L_{\max}$	$\ell_{1,\max}$	$\ell_{2,\max}$	FWHM duration [fs]	$n_{\text{part}}^{\text{lin}}$
6.6	10^{13}	10	18	18	3.3	504
$6.7(a),(b)$	10^{13}	10	18	18	3.3	504
$6.7(c),(d)$	3.5×10^{14}	20	10	20	6.6	821

B.6. Parameters for Chap. 7

We employ an fundamental IR pulse with a wave length of $\lambda_{\mathrm{IR}} = 400$ nm and a peak intensity of $I_{\mathrm{IR}} = 10^{11}$ and an APT consisting of the harmonics H_{2q-1} with q = 16-22 for Sec. 7.2 and q = 16-18 for Sec. 7.3 with a peak intensity of $I_{\mathrm{APT}} = 10^{12}$ W/cm^2. Each pulse has a FWHM duration $T = 3$ fs. We calculate 21 time delays τ between the central time of the IR and APT ranging from $\tau = -667$ as to $\tau = 667$ as to mimic an experimental RABBITT trace. We use a radial box spanning 880 a.u. $\times$ 616 a.u. An absorbing boundary starting at 792 a.u. for the larger box side and at 556 a.u. for the smaller box side is used. For the close-coupling expansion we employ maximal total angular momenta up to $L_{\max} = 3$ and individual angular momenta up to $\ell_{1,\max} = \ell_{2,\max} = 4$, corresponding to 21 partial waves.

C. Challenges in achieving converged results for long-wavelength double ionization

In this appendix we discuss the challenges inherent to the numerical simulation using a linear polarized laser pulse with a wavelength of $\lambda = 394$ nm. Due to the unfavourable scaling of the time-dependent close-coupling method with λ the results for this wavelength are only partially converged. In the calculation we use a pulse with a $\sin^2$ envelope, a peak intensity $I = 3.5 \times 10^{14}$ W/cm^2 and a total pulse duration of $T = 13.2$ fs (10 o. c.). We use a radial box spanning 240 a.u. $\times$ 240 a.u.. An absorbing boundary starting at 228 a.u. and a cut-off for analytical propagation starting at 180 a.u. is used.

The resulting photoelectron spectrum clearly shows multiple bands with constant E_{tot} where each band can be directly linked to the number of absorbed photons. These bands should appear at total energies according to Eq. (6.1) [dashed lines in Fig. 6.1(b)]. In the calculation the bands have the correct distance between each other (ω) but appear at the wrong energies [Fig. C.1]. As to why they do not correspond with Eq. (6.1) remains an open question. One possibility is that the visible peaks are Freeman resonances [57], thus overlaying the ATI peaks. Other possibilities are that with the used numerical parameters our results are not fully converged, or that this might be an effect of the short duration of the ionizing pulse.

The angular distribution [Fig. C.2] is, unlike the JAD [Fig. 6.7(c, d)], very susceptible to numerical convergence. Nonetheless, some characteristics which are similar to our results for 2-5 photon DI can be identified. For $n_{\text{ph}} = 29$ and equal-energy sharing the main lobes of the "butterfly" shape are visible, though at angles closer to 180°. In all cases there is a non-negligible chance for side-by-side emission, similar to the case for $\lambda = 197$ nm. For $n_{\text{ph}} = 30$ and equal-energy sharing the probability for side-by-side emission is only slightly smaller than the probability for back-to-back emission. It is not entirely clear whether the shown results are physically correct and how much they are affected by convergence problems.

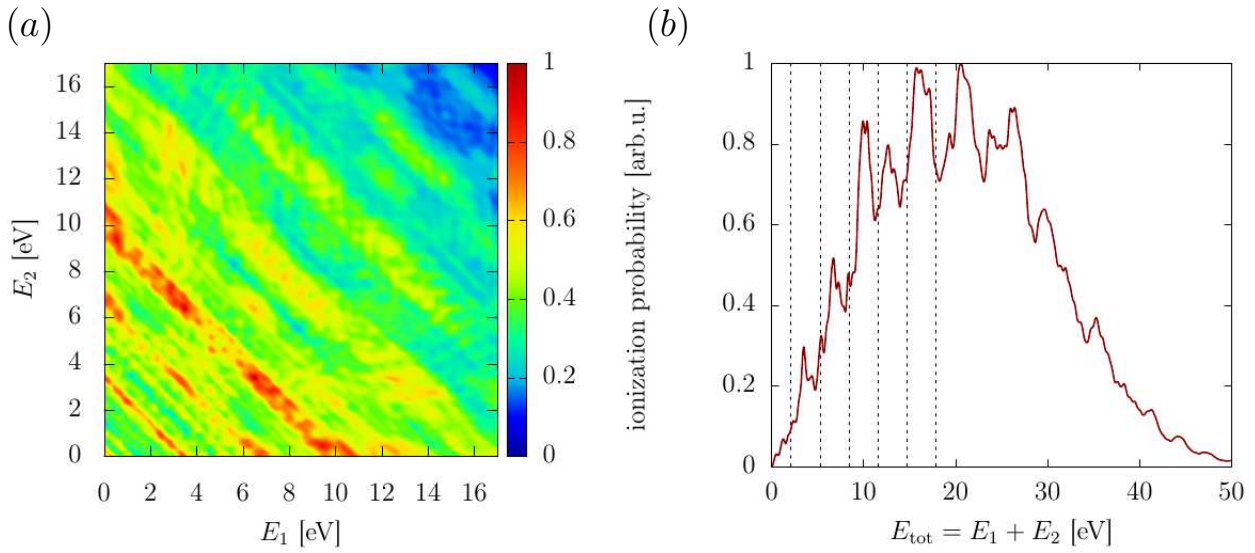

Figure C.1.: (a) Doubly differential photoelectron spectrum $P(E_1, E_2)$ for a laser pulse with a wave length $\lambda = 394$ nm and a total duration $T = 13.2$ fs. (b) Spectrum shown in (a) integrated with regards to $\Delta E = E_1 - E_2$. The dashed lines indicate the total energies according to Eq. (6.1).

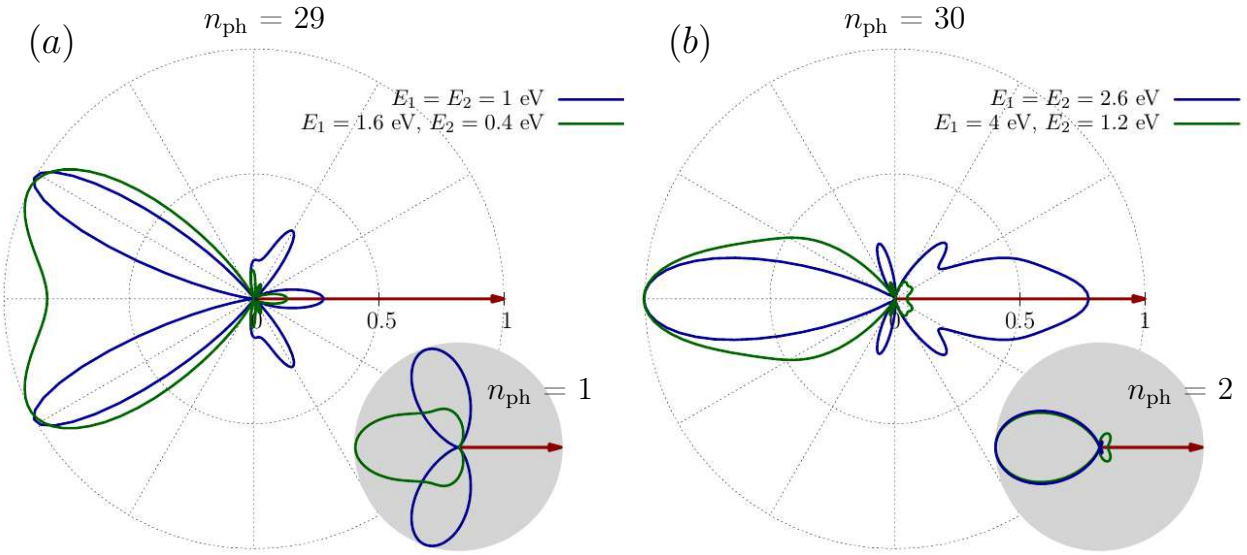

Figure C.2.: Angular distributions ($\theta_1 = 0, \varphi_1 = \varphi_2 = 0$) in the $\hat{x}$-$\hat{y}$ plane for a linear polarized laser pulse with a wave length of $\lambda = 394$ nm and duration of $T_{\mathrm{FWHM}} = 13.2$ fs. This wavelength corresponds to a photon energy of 3.15 eV. (a) Total energy corresponding to $n_{\mathrm{ph}} = 29$. The grey inset shows the angular distribution for $n_{\mathrm{ph}} = 1$ from Fig. 4.3(b, d) for comparison, with $E_1 = E_2 = 10$ eV (blue line) and $E_1 = 19$ eV, $E_2 = 1$ eV (green line). (b) Total energy corresponding to $n_{\mathrm{ph}} = 30$. The grey inset shows the angular distribution for $n_{\mathrm{ph}} = 2$ from Fig. 5.3 for comparison, with $E_1 = E_2 = 11.5$ eV (blue line) and $E_1 = 22$ eV, $E_2 = 1$ eV (green line). Direction of the first electron is marked by the red arrow, parallel to the laser polarization ($\theta_1 = 0$ and $\varphi_1 = 0$).

Acknowledgements

Lastly, I would like to take this opportunity to give my thanks to the people without whom this diploma thesis would not have been possible. First of all, I would like to thank Joachim Burgdörfer for his invaluable insights and discussions throughout this work. Further, I want to express my gratitude to Stefan Donsa for taking the time to always answer my not so bright questions and generally guiding me through all of this. I would like to thank all my other colleagues from the ITP for making it a pleasure to be around at the institute as well as after work, even those from the 3rd floor. I thank Johannes Feist for his contribution to the helium code which I mainly used throughout this thesis. I would like to thank the Scientific Computing Administration of the Johannes Kepler University Linz for letting me heavily use the MACH2 supercomputer during this thesis. Finally, I would like to thank my family for always supporting me during my studies and this diploma thesis.

Bibliography

[1] M. Lewenstein, P. Balcou, M. Y. Ivanov, A. L'Huillier, and P. B. Corkum. *Theory of high-harmonic generation by low-frequency laser fields.* Phys. Rev. A **49**, 2117 (1994).

[2] K. J. Schafer and K. C. Kulander. *High Harmonic Generation from Ultrafast Pump Lasers.* Phys. Rev. Lett. **78**, 638 (1997).

[3] M. Hentschel, R. Kienberger, C. Spielmann, G. A. Reider, N. Milosevic, T. Brabec, P. Corkum, U. Heinzmann, M. Drescher, and F. Krausz. *Attosecond metrology.* Nature **414**, 509 (2001).

[4] P. Agostini and L. F. DiMauro. *The physics of attosecond light pulses.* Reports on Progress in Physics **67**, 813 (2004).

[5] F. Krausz and M. Ivanov. *Attosecond physics.* Rev. Mod. Phys. **81**, 163 (2009).

[6] M. Y. Ivanov, R. Kienberger, A. Scrinzi, and D. M. Villeneuve. *Attosecond physics.* Journal of Physics B: Atomic, Molecular and Optical Physics **39**, R1 (2005).

[7] F. Krausz and P. B. Corkum. *Attosecond science.* Nature Physics **3**, 381 (2007).

[8] P. B. Corkum and Z. Chang. *The Attosecond Revolution.* Opt. Photon. News **19**, 24 (2008).

[9] J. S. Briggs and V. Schmidt. *Differential cross sections for photo-double-ionization of the helium atom.* Journal of Physics B: Atomic, Molecular and Optical Physics **33**, R1 (1999).

[10] D. Proulx and R. Shakeshaft. *Double ionization of helium by a single photon with energy 89–140 eV.* Phys. Rev. A **48**, R875 (1993).

[11] J. Feist, S. Nagele, R. Pazourek, E. Persson, B. I. Schneider, L. A. Collins, and J. Burgdörfer. *Probing Electron Correlation via Attosecond xuv Pulses in the Two-Photon Double Ionization of Helium.* Phys. Rev. Lett. **103**, 063002 (2009).

[12] M. S. Pindzola, Y. Li, and J. Colgan. *Multiphoton double ionization of helium using femtosecond laser pulses.* Journal of Physics B: Atomic, Molecular and Optical Physics **49**, 215603 (2016).

[13] B. Walker, B. Sheehy, L. F. DiMauro, P. Agostini, K. J. Schafer, and K. C. Kulander. *Precision Measurement of Strong Field Double Ionization of Helium.* Phys. Rev. Lett. **73**, 1227 (1994).

[14] M. Lein, E. K. U. Gross, and V. Engel. *Intense-Field Double Ionization of Helium: Identifying the Mechanism.* Phys. Rev. Lett. **85**, 4707 (2000).

[15] J. S. Parker, B. J. S. Doherty, K. T. Taylor, K. D. Schultz, C. I. Blaga, and L. F. DiMauro. *High-Energy Cutoff in the Spectrum of Strong-Field Nonsequential Double Ionization.* Phys. Rev. Lett. **96**, 133001 (2006).

[16] K. Henrichs, S. Eckart, A. Hartung, D. Trabert, K. Fehre, J. Rist, H. Sann, M. Pitzer, M. Richter, H. Kang, M. S. Schöffler, M. Kunitski, T. Jahnke, and R. Dörner. *Multiphoton double ionization of helium at 394 nm: A fully differential experiment.* Phys. Rev. A **98**, 043405 (2018).

[17] F. Byron and C. Joachain. *Multiple ionization processes in helium.* Physics Letters A **24**, 616 (1967).

[18] A. Knapp, M. Walter, T. Weber, A. L. Landers, S. Schössler, T. Jahnke, M. Schöffler, J. Nickles, S. Kammer, O. Jagutzki, L. P. H. Schmidt, T. Osipov, J. Rösch, M. H. Prior, H. Schmidt-Böcking, C. L. Cocke, J. Feagin, and R. Dörner. *Energy sharing and asymmetry parameters for photo double ionization of helium 100 eV above threshold in single-particle and Jacobi coordinates.* Journal of Physics B: Atomic, Molecular and Optical Physics **35**, L521 (2002).

[19] M. Achler, V. Mergel, L. Spielberger, R. Dörner, Y. Azuma, and H. Schmidt-Böcking. *Photo double ionization of He by circular and linear polarized single-photon absorption.* Journal of Physics B: Atomic, Molecular and Optical Physics **34**, 965 (2001).

[20] J. Berakdar and H. Klar. *Circular dichroism in double photoionization.* Phys. Rev. Lett. **69**, 1175 (1992).

[21] A. Y. Istomin, E. A. Pronin, N. L. Manakov, S. I. Marmo, and A. F. Starace. *Elliptic and Circular Dichroism Effects in Two-Photon Double Ionization of Atoms.* Phys. Rev. Lett. **97**, 123002 (2006).

[22] K. Kondo, A. Sagisaka, T. Tamida, Y. Nabekawa, and S. Watanabe. *Wavelength dependence of nonsequential double ionization in He.* Phys. Rev. A **48**, R2531 (1993).

[23] H. Kang, S. Chen, Y. Wang, W. Chu, J. Yao, J. Chen, X. Liu, Y. Cheng, and Z. Xu. *Wavelength-dependent nonsequential double ionization of magnesium by intense femtosecond laser pulses.* Phys. Rev. A **100**, 033403 (2019).

[24] V. Véniard, R. Taïeb, and A. Maquet. *Phase dependence of (N+1)-color (N>1) ir-uv photoionization of atoms with higher harmonics.* Phys. Rev. A **54**, 721 (1996).

[25] H. Muller. *Reconstruction of attosecond harmonic beating by interference of two-photon transitions.* Applied Physics B **74**, s17 (2002).

[26] K. Klünder, J. M. Dahlström, M. Gisselbrecht, T. Fordell, M. Swoboda, D. Guénot, P. Johnsson, J. Caillat, J. Mauritsson, A. Maquet, R. Taïeb, and A. L'Huillier. *Probing Single-Photon Ionization on the Attosecond Time Scale.* Phys. Rev. Lett. **106**, 143002 (2011).

[27] E. P. Månsson, D. Guénot, C. L. Arnold, D. Kroon, S. Kasper, J. M. Dahlström, E. Lindroth, A. S. Kheifets, A. L'Huillier, S. L. Sorensen, and M. Gisselbrecht. *Double ionization probed on the attosecond timescale.* Nature Physics **10**, 207 (2014).

[28] M. S. Pindzola, F. Robicheaux, S. D. Loch, J. C. Berengut, T. Topcu, J. Colgan, M. Foster, D. C. Griffin, C. P. Ballance, D. R. Schultz, T. Minami, N. R. Badnell, M. C. Witthoeft, D. R. Plante, D. M. Mitnik, J. A. Ludlow, and U. Kleiman. *The time-dependent close-coupling method for atomic and molecular collision processes.* Journal of Physics B: Atomic, Molecular and Optical Physics **40**, R39 (2007).

[29] J. Feist. *Two-photon double ionization of helium.* Ph.d thesis, Vienna Univ. of Technology (2009).

[30] S. Donsa. *Ionization phases and electron angular distributions of multi-electron atoms probed by attosecond pulses.* Ph.D. thesis, Vienna Univ. of Technology (2019).

[31] V. Schmidt. *Electron Spectrometry of Atoms using Synchrotron Radiation.* Cambridge Monographs on Atomic, Molecular and Chemical Physics. Cambridge University Press (1997).

[32] H. Friedrich. *Theoretical Atomic Physics.* Springer, Berlin (2005).

[33] D. M. Wolkow. *Über eine Klasse von Lösungen der Diracschen Gleichung.* Zeitschrift für Physik **94**, 250 (1935).

[34] H. R. Reiss. *Effect of an intense electromagnetic field on a weakly bound system.* Phys. Rev. A **22**, 1786 (1980).

[35] J. Feist, S. Nagele, R. Pazourek, E. Persson, B. I. Schneider, L. A. Collins, and J. Burgdörfer. *Nonsequential two-photon double ionization of helium.* Phys. Rev. A **77**, 043420 (2008).

[36] A. Liu and U. Thumm. *Laser-assisted XUV few-photon double ionization of helium: Joint angular distributions.* Phys. Rev. A **89**, 063423 (2014).

[37] S. Donsa, I. Březinová, H. Ni, J. Feist, and J. Burgdörfer. *Polarization tagging of two-photon double ionization by elliptically polarized XUV pulses.* Phys. Rev. A **99**, 023413 (2019).

[38] Z.-j. Teng and R. Shakeshaft. *Double ionization of helium by a single high-energy photon.* Phys. Rev. A **47**, R3487 (1993).

[39] D. N. Fittinghoff, P. R. Bolton, B. Chang, and K. C. Kulander. *Observation of nonsequential double ionization of helium with optical tunneling.* Phys. Rev. Lett. **69**, 2642 (1992).

[40] P. B. Corkum. *Plasma perspective on strong field multiphoton ionization.* Phys. Rev. Lett. **71**, 1994 (1993).

[41] L. Avaldi and A. Huetz. *Photodouble ionization and the dynamics of electron pairs in the continuum.* Journal of Physics B: Atomic, Molecular and Optical Physics **38**, S861 (2005).

[42] R. Pazourek, J. Feist, S. Nagele, E. Persson, B. I. Schneider, L. A. Collins, and J. Burgdörfer. *Universal features in sequential and nonsequential two-photon double ionization of helium.* Phys. Rev. A **83**, 053418 (2011).

[43] A. Palacios, T. N. Rescigno, and C. W. McCurdy. *Time-dependent treatment of two-photon resonant single and double ionization of helium by ultrashort laser pulses.* Phys. Rev. A **79**, 033402 (2009).

[44] J. Parker and C. W. Clark. *Study of a plane-wave final-state theory of above-threshold ionization and harmonic generation.* J. Opt. Soc. Am. B **13**, 371 (1996).

[45] D. N. Fittinghoff, P. R. Bolton, B. Chang, and K. C. Kulander. *Polarization dependence of tunneling ionization of helium and neon by 120-fs pulses at 614 nm.* Phys. Rev. A **49**, 2174 (1994).

[46] A. Zielinski, V. P. Majety, and A. Scrinzi. *Double photoelectron momentum spectra of helium at infrared wavelength.* Phys. Rev. A **93**, 023406 (2016).

[47] R. Pazourek, S. Nagele, and J. Burgdörfer. *Attosecond chronoscopy of photoemission.* Rev. Mod. Phys. **87**, 765 (2015).

[48] L. Eisenbud. *The Formal Properties of Nuclear Collisions.* Ph.D. thesis, Princeton University (1948).

[49] E. P. Wigner. *Lower Limit for the Energy Derivative of the Scattering Phase Shift.* Phys. Rev. **98**, 145 (1955).

[50] F. T. Smith. *Lifetime Matrix in Collision Theory.* Phys. Rev. **118**, 349 (1960).

[51] A. Galàn, L. Argenti, and F. Martìn. *Modulation of Attosecond Beating in Resonant Two-Photon Ionization.* Physical Review Letters **113** (2014).

[52] J. M. Dahlström, A. L'Huillier, and A. Maquet. *Introduction to attosecond delays in photoionization.* Journal of Physics B: Atomic, Molecular and Optical Physics **45**, 183001 (2012).

[53] R. Pazourek, S. Nagele, and J. Burgdörfer. *Probing time-ordering in two-photon double ionization of helium on the attosecond time scale.* Journal of Physics B: Atomic, Molecular and Optical Physics **48**, 061002 (2015).

[54] T. N. Rescigno and C. W. McCurdy. *Numerical grid methods for quantum-mechanical scattering problems.* Phys. Rev. A **62**, 032706 (2000).

[55] B. I. Schneider and L. A. Collins. *The discrete variable method for the solution of the time-dependent Schrödinger equation.* Journal of Non-Crystalline Solids **351**, 1551 (2005). Papers from the Michael Weinberg Symposium.

[56] C. W. McCurdy, M. Baertschy, and T. N. Rescigno. *Solving the three-body Coulomb breakup problem using exterior complex scaling.* Journal of Physics B: Atomic, Molecular and Optical Physics **37**, R137 (2004).

[57] R. R. Freeman and P. H. Bucksbaum. *Investigations of above-threshold ionization using subpicosecond laser pulses.* Journal of Physics B: Atomic, Molecular and Optical Physics **24**, 325 (1991).